Journal of Materials Chemistry A

ROYAL SOCIETY OF CHEMISTRY

REVIEW

View Article Online
View Journal | View Issue

Cite this: *J. Mater. Chem. A*, 2021, **9**, 782

Recent progress of high-entropy materials for energy storage and conversion

Azadeh Amiri and Reza Shahbazian-Yassar *

The emergence of high-entropy materials (HEMs) with their excellent mechanical properties, stability at high temperatures, and high chemical stability is poised to yield new advancement in the performance of energy storage and conversion technologies. This review covers the recent developments in catalysis, water splitting, fuel cells, batteries, supercapacitors, and hydrogen storage enabled by HEMs covering metallic, oxide, and non-oxide alloys. Here, first, the primary rules for the proper selection of the elements and the formation of a favorable single solid solution phase in HEMs are defined. Furthermore, recent developments in different fields of energy conversion and storage achieved by HEMs are discussed. Higher electrocatalytic and catalytic activities with longer cycling stability and durability compared to conventional noble metal-based catalysts are reported for high-entropy materials. In electrochemical energy storage systems, high-entropy oxides and alloys have shown superior performance as anode and cathode materials with long cycling stability and high capacity retention. Also, when used as metal hydrides for hydrogen storage, remarkably high hydrogen storage capacity and structural stability are observed for HEMs. In the end, future directions and new energy-related technologies that can be enabled by the application of HEMs are outlined.

Received 29th September 2020
Accepted 24th November 2020

DOI: 10.1039/d0ta09578h

rsc.li/materials-a

1. Introduction

Traditionally, the alloying strategy has been mostly limited to adding small fractions of elements as dopants into a base material to obtain a new composite material with improved properties. In this approach, finite types of possible alloys can be developed, and extensive research in the past have explored such alloys. A new method of alloying emerged in 2004, proposed by two research groups[1,2] independently, introducing single-phase solid solution alloys of five or more principal elements with near-equimolar compositions. Yeh *et al.*[2] introduced the concept of high-entropy alloys (HEAs) based on the fact that the configurational entropy of mixing (ΔS_{mix} from eqn (1)) increases with addition of more equimolar principal elements to the alloy system.

Department of Mechanical and Industrial Engineering, University of Illinois, Chicago, IL 60607, USA. E-mail: rsyassar@uic.edu

Azadeh Amiri is currently pursuing her PhD degree in Mechanical Engineering under the supervision of Prof. Reza Shahbazian-Yassar in the Department of Mechanical & Industrial Engineering, University of Illinois at Chicago. She received her Master of Science in Mechanical Engineering from Southern Illinois University at Carbondale (2017) and her bachelors in Chemical Engineering from University of Tehran (2014). Her current research interests are in high-entropy material nanoparticles, in situ electron microscopy studies of high-entropy alloy formation and their functional properties.

Dr Reza Shahbazian-Yassar is currently a Professor at the Department of Mechanical & Industrial Engineering and Department of Civil & Materials Engineering, University of Illinois at Chicago. He obtained his PhD degree in Materials Science from Washington State University (2005). His current research interests include advanced nanomaterials for electrochemical energy storage devices, and in situ electron microscopy of nanomaterials.

$$\Delta S_{mix} = -R\sum_{i=1}^{n} c_i \ln c_i = -R\sum_{n}\frac{1}{n}\ln\frac{1}{n} = R\ln n \quad (1)$$

n is the number of elements, c_i is the concentration of component i and R is the gas constant.

Based on this hypothesis, the thermodynamic contribution of high ΔS_{mix} in a system with a minimum of five equimolar elements to the Gibbs free energy (ΔG_{mix}) at high temperature is sufficient to compensate for the enthalpy formation (ΔH_{mix}) of intermetallic compounds and form a single-phase solution of multiple elements ($\Delta G_{mix} \leq 0$ from eqn (2)). Later, the definition of HEA expanded to alloys composed of five or more elements with compositions between 5% and 35% (composition-based definition)[3] and multi-elemental alloys with $\Delta S_{mix} > 1.5R$ (entropy-based definition).[4]

$$\Delta G_{mix} = \Delta H_{mix} - T\Delta S_{mix} \quad (2)$$

The presence of multiple elements with different characteristics gives HEAs four core effects: (1) high-entropy, (2) lattice distortion, (3) sluggish diffusion, and (4) cocktail effect (Fig. 1). The high-entropy effect is the main concept of HEMs. Multiple near-equimolar components increase the configurational entropy (eqn (1)) and stability of the single-phase structure at higher temperature.[5] The crystal lattice of an HEM is composed of atoms with different sizes randomly occupying lattice sites. These slightly unbalanced sites of the lattice and random positions of atoms lead to severe lattice distortion. The lattice distortion is the reason for lower intensity in X-ray diffraction peaks,[6–8] lower thermal and electrical conductivity,[7,8] as well as the higher hardness of these materials.[7,8] In addition, the lattice distortion of HEAs can delay atomic movement and replacements, and results in another effect called sluggish diffusion.[2,8] The sluggish diffusion effect may lead to the formation of nano-precipitates or amorphous phases in HEMs.[2] Finally, the cocktail effect of HEMs occurs when there are multiple elements with various properties in a mixture.[5] The ultimate property of such alloy is not equal to the sum of the properties of its components and is unpredictable.[5,7] The synergetic mixture of elements results in an HEM with excellent features as functional materials in energy storage and conversion systems.

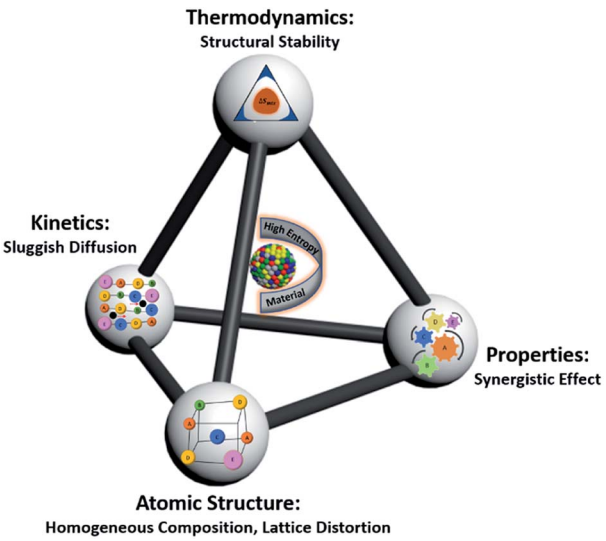

Fig. 1 The schematic showcases the four core effects of HEMs.

The concept of high-entropy stabilized multi-element alloys and their astonishing properties was later extended to oxides and other systems. Rost *et al.*[9] explored the idea of entropy-driven stabilization in a mixture of a five-metal oxide to form a single solid solution with a rock-salt crystal structure. Similar to multi-elemental alloys, here, the configurational disorder can increase with the addition of different metal cations to a single cation sublattice when the anion sublattice is only occupied by oxygen. Therefore, the configurational entropy of multi-elemental oxides can be obtained from eqn (3):

$$\Delta S_{mix} = -R\left[\left(\sum_{i=1}^{n} c_i \ln c_i\right)_{\text{cation-site}} + \left(\sum_{i=1}^{n} c_i \ln c_i\right)_{\text{anion-site}}\right] \quad (3)$$

Having oxygen as the single anion in the ionic structure, the second term for anion-sites is zero and the entropy increases by adding to the total number of cations. Later, several other multi-elemental oxides with fluorite,[10–12] perovskite,[13,14] and spinel[15,16] crystal structures materialized and broadened the variety of high-entropy oxides included in this approach. The concept of entropy-stabilized metallic, oxide and non-oxide ceramic materials can be generalized to high-entropy materials (HEMs), considering the development of new types of high-entropy ceramics such as carbides,[17–20] diborides,[21,22] nitrides[23] and silicides,[24] sulfides[25] as well as phosphides[26] and fluorides.[27] Zeolites[28] and metal–organic frameworks (MOFs)[29,30] with five near-equimolar active metallic elements are the other forms of organic–inorganic HEMs.

The high-entropy concept is not limited to inorganic materials and is not defined by only the number of elements and compositional disorder. High-entropy configuration for organic materials such as polymers and carbon materials can be considered as an effective way of designing interesting new materials. In this regard, the entropy is depicted as the degree of disorder of the system. Feng and Zhuang[31] introduced the concept of meso-entropy carbon materials. Considering the value of entropy of each form of carbon allotropes, the meso-entropy of materials can be manipulated between the high and low entropy forms. The level of disorder and entropy value can be manipulated by changes in the structure of carbon materials like the number of members in carbon rings. High entropy can also be considered for organic semicrystalline copolymer materials as high-entropy polymers. Having different types of polymers with various ratios in repeating units increases the lattice-packing entropy and can affect the phase transition of crystalline polymers.[32]

Some of the fundamental aspects, structural effects, and designing strategies of HEAs have been discussed in recent years.[5,33–38] Research on HEOs and other HEMs are more recent and less established compared to that on metallic alloys. Due

to some appealing and advantageous features like the synergistic effect, high-temperature stability, and corrosion resistance, HEMs are excellent candidates in various energy-related applications.[39,40] In this respect, the focus of this work is to review the emerging applications and performances of all the HEMs in catalysis, and energy conversion and storage applications reported in the literature. Afterward, considering the confirmed or possible capabilities of HEMs, other prospective applications of these materials in various energy-related systems are discussed. But first, the general criteria for the proper selection of elements in HEMs for the formation of a favorable single solid solution phase are addressed and classified.

2. Parameters affecting HEA formation

A few years after introducing HEAs, comparison of different experimental results showed that not all the HEAs exhibit a single crystalline solid-solution phase.[41] There are HEAs in an amorphous phase like high-entropy bulk metallic glasses and multi-phase alloys with intermetallic compounds as well as solid solutions with ordered structures.[41,42] This indicates that the entropy-driven effect from eqn (1) is not the only factor in determining the thermodynamically stable phases in multi-component alloys. The entropy of mixing from eqn (1) is defined for ideal solutions.[41] However, for non-ideal regular solutions, there is always a deviation from the ideal case, and configurational entropy is not precisely equal to the value calculated.[41] In this respect, several research studies[41–49] attempted to investigate the effect of other parameters to define more reliable thermodynamic criteria for phase selection of multi-component HEMs. Most of the studies are statistical analysis of a large database of synthesized HEAs with their reported phase or phases and with the focus on factors distinguishing the conditions required for solid solution phase formation over intermetallic compounds. It should be mentioned that the high-entropy and other factors that favor the formation of a solid solution over other intermetallic phases result in enhancing the mechanical properties of HEAs due to the solution hardening effect, which increases the overall strength and ductility of the materials.[39] A summary of these new parameters and their effects on the prediction of phase formation is described below.

2.1 Enthalpy of mixing (ΔH_{mix})

Zhang *et al.*[41] investigated the effect of mixing enthalpy (ΔH_{mix}) on existing phases in HEAs reported in the literature. ΔH_{mix} for each multi-component system can be calculated based on Miedema's model[50] from the following equation:

$$\Delta H_{mix} = \sum_{i=1, i\neq j}^{n} 4\Delta H_{mix}^{AB} c_i c_j \quad (4)$$

where n is the number of components, c_i and c_j are the concentrations of components i and j, respectively; and ΔH_{mix}^{AB} is the mixing enthalpy of those two components (i & j) in their AB-type binary mixture. Later Guo and Liu,[42] with a similar statistical analysis in a larger database, studied the role of mixing enthalpy as one of the determining parameters in the formation of different phases in multi-component alloys. Their analysis concluded that a solid solution (data mixed with intermetallic) forms only when the mixing enthalpy is moderately positive or not very negative ($-22 \leq \Delta H_{mix} \leq 7$ kJ mol^{-1}) while an amorphous phase forms at more negative mixing enthalpies ($-49 \leq \Delta H_{mix} \leq -5.5$ kJ mol^{-1}) (Fig. 2a). From the proposed idea of HEA formation and based on eqn (2), when the entropy contribution to the Gibbs free energy at high temperature is larger than that of enthalpy, a solid solution likely forms. As mentioned before, only for an ideal solution, the calculated mixing entropy from eqn (1) is an exact value, and there are deviations and excess amounts for regular solutions. Besides, for an ideal solution, the enthalpy of mixing is zero ($\Delta H_{ideal\text{-}mix} = 0$) but it has a negative or positive value ($|\Delta H_{real\text{-}mix}| > 0$) for non-ideal solutions. The designated range of ΔH_{mix} for the formation of a solid solution phase suggests that when the absolute value of mixing enthalpy is small, the regular solution is closer to an ideal case. Therefore, a low magnitude of ΔH_{mix} is more favorable for the formation of single-phase solid solutions. On the other hand, elements are less willing to randomly distribute in the solution due to higher binding energies between them at more negative ΔH_{mix} and their miscibility gaps at more positive ΔH_{mix}.

2.2 Atomic size difference (δ)

The difference in the atomic size of the elements in a mixture turns out to be an important and critical factor affecting the phase selection of multi-component alloys. When the atomic sizes of the components are quite similar, they all have an equal

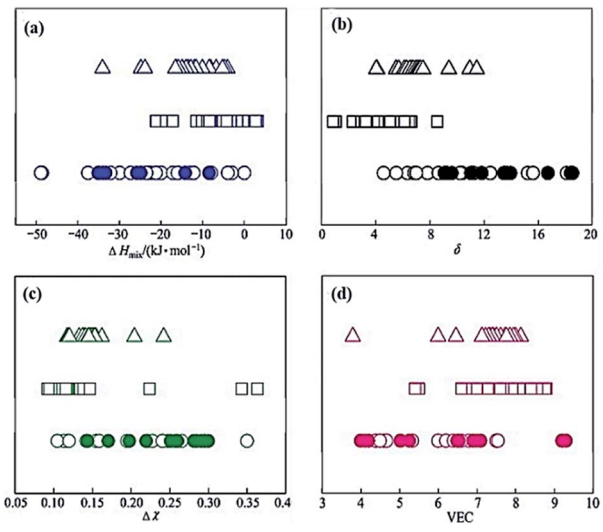

Fig. 2 Effect of (a) ΔH_{mix}, (b) δ, (c) $\Delta\chi$, and (d) VEC on phase stability in HEAs. The symbols □, △, ○ and ● represent the solid solution phase, intermetallic phase, equimolar amorphous phase, and non-equimolar amorphous phase, respectively. Reproduced with permission (ref. 40). Copyright 2011, Elsevier.

probability of locating in any of the crystal lattice sites, and their random distribution leads to a disordered structure of the solid solution. For the non-ideal real mixture of multiple components, there is an atomic size mismatch effect. The effect of this parameter on the phase stability of multi-component alloys was also first studied by Zhang *et al.*[41] by calculating the δ parameter for HEAs from the following equation:

$$\delta = 100\sqrt{\sum_{i=1}^{n} c_i\left(1-\frac{r_i}{\bar{r}}\right)^2}, \quad \bar{r} = \sum_{i=1}^{n} c_i r_i \tag{5}$$

where n is the number of components, c_i is the concentration of component i, r_i is the atomic radius of component i and $\bar{r}$ is the average atomic size of the n components in the alloy. The role of δ as a separate parameter was evaluated in several studies to find its critical value for phase selection. The analysis by Guo and Liu[42] concluded that a solid solution (data mixed with intermetallic) forms only when the atomic-size difference of elements is small ($\delta \leq 8.5$) while an amorphous phase forms when there is a larger difference in the atomic size of the components ($\delta \geq 9$) (Fig. 2b). Yang and Zhang[43] narrowed down the specified range of δ for the formation of solid solutions exclusively. Their evaluations led to a rule of $\delta \leq 6.6$ for solid solution phase selection over intermetallic compounds (Fig. 3a). Differences in atomic sizes are important factors affecting the lattice distortion of HEAs. Lattice distortion can reduce the thermal and electrical conductivity due to the scattering of electrons and phonons.[39] Also, the peak intensities of X-ray diffraction are largely decreased as a result of scattering by distorted lattice planes.[51]

2.3 Electronegativity difference ($\Delta\chi$)

The effect of the difference in electronegativity of elements in HEAs is another parameter studied for phase selection criteria. Guo and Liu[42] considered the Pauling electronegativity of elements in a mixture to calculate their electronegativity difference from the following equation:

$$\Delta\chi = \sqrt{\sum_{i=1}^{n} c_i(\chi_i - \bar{\chi})^2}, \quad \bar{\chi} = \sum_{i=1}^{n} c_i\chi_i \tag{6}$$

where n is the number of components, c_i is the concentration of component i, χ_i is the Pauling electronegativity of component i and $\bar{\chi}$ is the average electronegativity of the n components in the alloy. However, in their study, $\Delta\chi$ exhibited no significant determinative effect on the formation of solid solutions, intermetallic, and amorphous phases (Fig. 2c). Later Poletti and Battezzati[49] used a similar factor but considering Allen electronegativity (χ_{Allen})[52] of components and reported that $3 < \Delta\chi_{Allen} < 6$ is the condition under which only a solid solution phase forms (Fig. 3b).

2.4 Valance electron concentration (VEC)

Valance electron concentration (VEC) is the total number of electrons in the outer shell of an atom. VEC for a multi-component system is defined based on the following weighted-average equation:

$$\mathrm{VEC} = \sum_{i=1}^{n} c_i \mathrm{VEC}_i \tag{7}$$

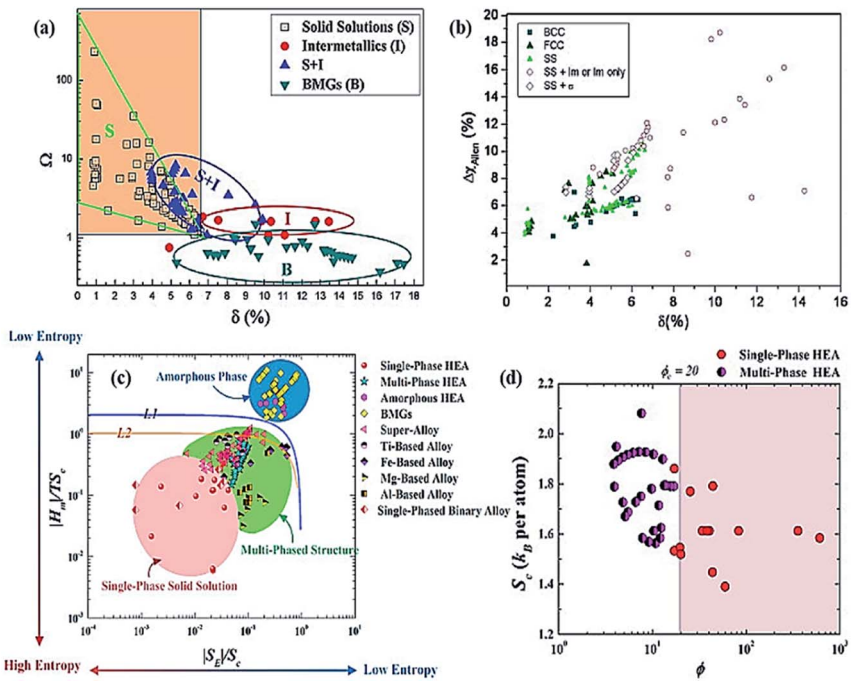

Fig. 3 Effect of (a) Ω and δ parameters (reproduced with permission (ref. 36). Copyright 2012, Elsevier), (b) χ_{Allen} and δ parameters (reproduced with permission (ref. 42). Copyright 2014, Elsevier), (c) $|S_E|/S_C$ and $|H_m|/(TS_C)$ terms (reproduced with permission (ref. 41). Copyright 2015, Elsevier), and (d) single $\varnothing$ parameter (reproduced with permission (ref. 40). Copyright 2015, Elsevier) on phase stability in HEAs.

where n is the number of components, c_i is the concentration of component i and VEC_i is the valance electron concentration of component i. VEC did not show any controlling effect on the phase stability of HEAs (Fig. 2d).[40] However, VEC was found to play an essential role in governing the crystal structure types of solid solution HEAs. Most of the reported solid solution HEAs have FCC and BCC structures, but a limited number of HCP-type HEAs based on heavy lanthanide metals are reported.[53–55] A study on the effect of VEC on the crystallography of HEAs by Guo *et al.*[46] suggested that VEC $\geq$ 8 and VEC < 6.87 favor FCC and BCC structures, respectively, while VEC between these values showed mixed FCC + BCC structures.[56] However, no HEAs reported with VEC < 5 were included in this study. Later HEAs with HCP solid solution structures composed of heavy lanthanide group elements with VEC_i of 3 were reported.[46] Therefore, VEC has a critical role in determining the crystal structure of HEAs and physical properties related to FCC or BCC structures.[57] HEAs with an FCC structure have good ductility due to strain hardening but lower strength[58] while solid solutions with a BCC structure have higher strength because of solution hardening but are more brittle because of lower ductility compared to FCC alloys.[59]

2.5 Ω parameter

Another parameter for phase formation prediction in multi-component alloys is Ω parameter. Defined by Yang and Zhang;[43] Ω is the ratio of the entropic contribution to Gibbs free energy at high temperature to enthalpic input and is calculated from the following equation:

$$\Omega = \frac{T_m \Delta S_{mix}}{|\Delta H_{mix}|}, \quad T_m = \sum_{i=1}^{n} c_i T_{mi} \tag{8}$$

where n is the number of components, $c_i$is the concentration of component i, T_{mi} is the melting point of component i and T_m is the weighted average melting point for a mixture of n components. Considering the atomic size difference effect with δ parameter and the ratio of entropy to enthalpy effect with Ω parameter, the required conditions for phase stability of a solid solution are $\Omega \geq 1.1$ and $\delta \leq 6$ (Fig. 3a).

2.6 Excess entropy (S_E)

The configurational entropy of mixing (S_C) for an ideal mixture of n components is only dependent on the concentration of elements ($S_C = \Delta S_{mix}$) and reaches its maximum when components are in equal atomic concentrations (eqn (1)). However, a non-ideal or real solution is composed of atoms with different sizes and packing fractions, which make its total configurational mixing entropy deviate from the ideal case. The excess entropy (S_E)[48] can represent the difference between the configurational mixing entropy for the ideal solution and regular mixture (eqn (9)). Unlike S_C of an ideal solution, S_E and, subsequently, the total mixing entropy (S_T) of a real solution depend not only on the concentration of elements (c_i) but also on their atomic radii (r_i) and packing densities (ξ) (according to the hard-sphere model[60]).

$$S_T(c_i, r_i, \xi) = S_C(c_i) + S_E(c_i, r_i, \xi) \tag{9}$$

Ye *et al.*[48] substituted the mixing entropy (S_{mix}) in eqn (2) with S_T and expressed the following condition required for the formation of a single solid solution phase in a multi-component mixture:

$$\frac{|S_E|}{S_C} \ll 1 - \frac{|H_m|}{TS_C} \tag{10}$$

Based on this theory, they investigated the effect of S_E on the phase selection of mixtures by calculating and plotting two terms, $|S_E|/S_C$ and $|H_m|/TS_C$ for a large number of HEAs in the literature. The result implied that lower ratios of these two terms are more favorable for the entropy-dominant formation of single-phase solid solution while at higher ratios, multiphase solid solutions and intermetallic phases tend to be formed (Fig. 3c). Higher excess entropy and enthalpy of mixing can be seen in multi-component systems with an amorphous phase, and their formation is mostly enthalpically favorable (Fig. 3c).

2.7 $\varnothing$ parameter

The discussed impacts of excess entropy and mixing enthalpy on phase formation criteria for HEAs were later combined by Ye *et al.*[47] in a single parameter $\varnothing$ defined as follows:

$$\varnothing = \frac{S_C - \left(\frac{|\Delta H_{mix}|}{T_m}\right)}{|S_E|} \tag{11}$$

Applying this parameter to the literature database indicated that there is a critical value of $\varnothing_c = 20$, which separates single-phase and multi-phase regions (Fig. 3d). Therefore, a single parameter rule of $\varnothing > \varnothing_c$ was proposed to design the single-phase HEAs.

2.8 Λ geometric parameter

Singh *et al.*[45] introduced a new purely geometric parameter, Λ (eqn (12)) and compared it with previous ruling parameters. They concluded that for ($\Lambda > 0.96$), ($0.24 < \Lambda < 0.96$) and ($\Lambda <$ 0.24), single-phase, two-phase, and multi-phase HEAs are expected to be formed, respectively.

$$\Lambda = \frac{\Delta S_{mix}}{\delta^2} \tag{12}$$

2.9 Effect of kinetics on phase formation

Most of the studies on the phase stability of HEAs and all the mentioned phase controlling parameters are from a thermodynamic point of view and focus on the detected phases in HEA samples at their thermodynamic equilibrium state (parameters in Fig. 4). However, for practical applications, it is vital to assess the structure and existing phases in samples after all cooling, solidification, and annealing steps. In this regard, kinetic effects play a considerable role in the phase stability of HEAs, especially in the formation of intermetallic phases in a system with an as-cast single solid solution phase.[61] He *et al.*[62] examined the impact of rapid and slow cooling rates on both solidification and solid-state phase transformation after annealing

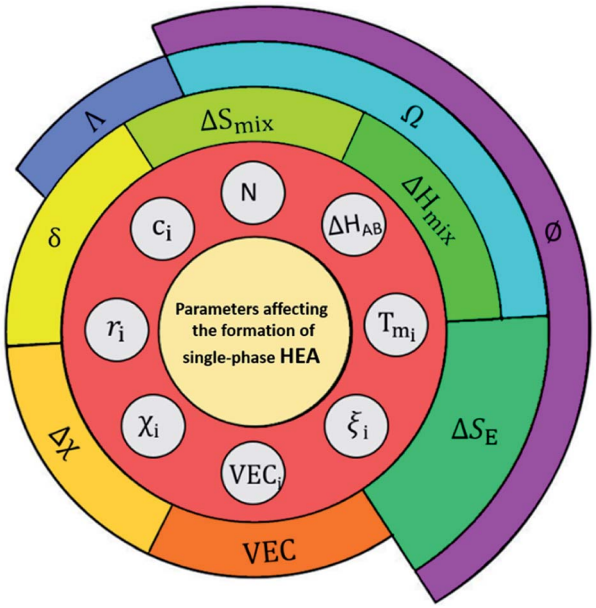

Fig. 4 Parameters affecting the formation of single-phase HEAs.

of $CoCrFeNiTi_{0.4}$ HEA as an example. It was observed that the formation of different intermetallic phases decreases at higher cooling rates and faster kinetics. This simply suggests that phase selection in HEAs can be tailored by controlling the kinetic factors during synthesis. Luan *et al.*[63] presented a perturbation model related to the number of elements and temperature to evaluate the stabilities of single-phase HEAs compared to the formation of a possible intermetallic. This model shows that with an increase in the number of elements, the number of possible intermetallics consisting of different combinations of those elements increases and leads to destabilization of the single-phase solid solution and formation of a multiphase structure. In other words, the increase in the number of elements is entropically favorable for the formation of a single-phase solid solution, but it also contributes to the unfavorable enthalpic contribution to the total Gibbs free energy of mixing. This fact points out the essential impact of high temperature on the phase stability of HEAs since it decreases the Gibbs free energy and boosts the stability of single-phase solid solutions. Therefore, based on the thermodynamic factors, most of the single-phase HEAs formed at high temperatures are not stable at room temperature and are expected to be in a multiphase structure. However, the kinetic factors during synthesis such as the fast cooling and sluggish dynamic effect of multicomponent systems considerably control the formation and stability of single-phase HEAs at room temperature.

3. Parameters affecting HEO formation

Generally, thermodynamic rules for phase stability of HEAs correspondingly apply to HEOs with adjustments for an ionic crystal structure. However, due to the limited number of successfully synthesized oxide and non-oxide HEMs in research studies, no statistical analysis of the database has been done yet to confirm their practical effects. Here, we address the general principles of choosing appropriate constituents for the formation of single-phase HEOs based on studies reported so far (Fig. 5).

3.1 Enthalpy of mixing (ΔH_{mix})

The effect of mixing enthalpy for HEOs is quite similar to that of HEAs, which is preferred to be near zero. The large positive ΔH_{mix} of metal oxides with different structures might not be compensated by the high-entropy effect or requires a much higher temperature for phase transition and mixing to happen.[9,64] On the other hand, the large negative ΔH_{mix} values of highly soluble metal oxides are not favorable for formation of an entropy-driven single-phase mixed oxide. Metal oxides with different crystal structures (*e.g.*, rock-salt, wurtzite) or cation coordination are suitable candidates in this regard. Rost *et al.*[9] used five equimolar metal oxides with rock-salt (MgO, CoO and NiO), tenorite (CuO) and wurtzite (ZnO) crystal structures and synthesized an HEO with a single-phase rock-salt crystal structure. In this case, even with the ideal mixing enthalpy of zero, tenorite and wurtzite had a positive enthalpy for structural transition to the final rock-salt structure. Therefore, the formation of the single-phase mixed oxides with the rock-salt structure is entropically favorable and the oxides are called entropy-stabilized oxides. Among all possible prototype oxides of metal cations, at least one should have a different crystal structure to prove the entropy-stabilization of the product single-phase HEO.

3.2 Ionic radius

In the same way as the difference in atomic size radius (δ) for HEAs, the ionic radius of metal cations affects lattice distortion

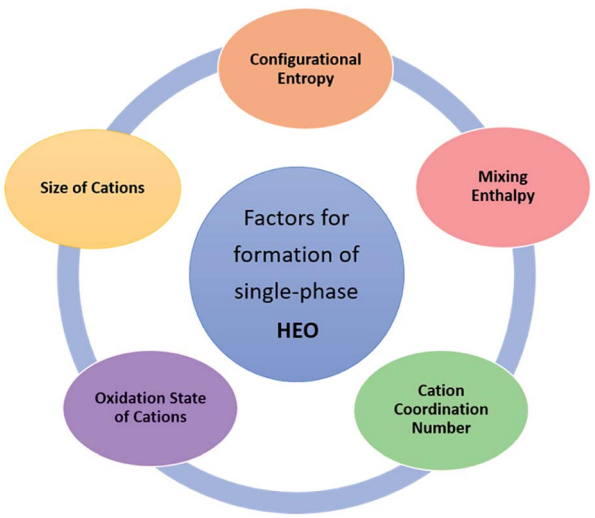

Fig. 5 Parameters affecting the formation of single-phase HEOs.

and formation of single-phase HEOs. In order to obtain single-phase HEOs with a cubic rock-salt or fluorite structure, choosing metal cations with similar cationic radius (r_c) is considered.[9,12] In ABO_3 type perovskite HEOs with a primitive cubic structure in which either or both A and B cation sites can be composed of multiple oxides, the ionic radius differences are calculated separately for each of the multi-cationic site as δ_{rA} and δ_{rB}. However, the formation of a single-phase high-entropy perovskite oxide did not follow the atomic size difference range of $\delta < 6.5\%$ and occurred even at larger δ_{rB} of 11–13%.[14] Therefore, other structural factors such as Goldschmidt's tolerance factor (t) for the stability of perovskite cubic structures from the following equation were applied to multi-component systems:

$$t = \frac{\bar{r}_A + r_O}{\sqrt{2}(\bar{r}_B + r_O)} \quad (13)$$

where $\bar{r}_A$ and $\bar{r}_B$ are the weighted average ionic radius of cations in A and B sites, respectively, and r_O is the radius of the oxygen anion. A cubic phase is likely stable if $0.9 \leq t \leq 1.0$, while a hexagonal or tetragonal phase may form if $t > 1.0$ and an orthorhombic or rhombohedral phase may form if $t < 0.9$. The experiments suggested that the Goldschmidt tolerance factor close to unity ($t \approx 1.00$) is perhaps a necessary but not sufficient criterion to form a single high-entropy perovskite phase.[13,14]

3.3 Oxidation state

In a single-phase multi-cation HEO, isovalent metal cations occupy the same cation sublattice sites, and anions preserve the electroneutrality of the lattice.[9,40] Therefore, the affinity of an element towards a particular oxidation state plays a crucial role in the formation of single-phase HEOs and the type of crystal structure. In a cubic rock-salt multi-cation oxide, metals have an equal oxidation state of +2 (M^{2+}) and oxide form of MO (like transition metals), but in the fluorite structure, they have a similar oxidation state of +4 (M^{4+}) and oxide form of MO_2 (like rare-earth metals). In an ABO_3 perovskite HEO, the oxidation state of A and B sites could be similar (+III) or different (+II and +IV); however, all cations in the same sublattice have the same oxidation state. The critical role of some cations in the formation and stability of single-phase HEOs has been observed and attributed to a more stable form of those cations in a specific oxidation state.[10]

3.4 Cation coordination number

In an ionic crystal structure, each ion is surrounded by other ions (cations and anions). The number of ions that immediately surround a particular ion is the coordination number (CN) and it depends on the relative size of ions. All cations occupying the same sublattice have the same coordination number. In a perovskite oxide with two cation sublattices, the A sites are occupied by larger cations with CN of 12 and B sites by smaller cations with CN of 6.

4. Synthesis methods and characterization techniques for crystalline HEMs

There are different physical and chemical synthesis routes to regulate the affecting thermodynamic or kinetic factors and successfully fabricate HEMs with single solid solution phase and homogeneous distribution of elements. The role of the synthesis approach and conditions are more crucial in the formation of high-entropy nanomaterials to control the size, phase structure and composition distribution.

HEAs with a single-phase crystal structure have been successfully synthesized by various physical and chemical routes. Mechanical alloying like arc melting[65–67] and high energy ball milling[68,69] are simpler processes to synthesize HEAs in a larger amount and relatively bigger particle size. Dealloying of a mechanically alloyed multicomponent alloy precursor is a common method to fabricate nano-porous HEAs.[70–72] Wet-chemistry processes such as solvothermal synthesis,[73] ultrasonication-assisted wet chemistry,[74] and sol–gel auto-combustion[75] are effectively used for the formation of nano-size HEAs. Other novel synthesis methods such as carbothermal shock,[76–78] fast-moving bed pyrolysis[79] and sputtering deposition[80,81] are reported to produce fine size HEA NPs but in low yield. Different synthesis methods reported in the literature for the formation of bulk and nano-size HEAs are analysed and compared in more detail in other studies.[39,82–84]

The fabrication of HEO powders is easier by conventional solid-state mixing of metal salts but requires high-temperature synthesis, which is their main disadvantage.[9,85] Lower energy demanding wet-chemistry methods such as co-precipitation,[86,87] solvothermal method,[88] hydrothermal method,[87] spray pyrolysis,[86,89,90] mechanochemistry,[91,92] sonochemistry[93] and solution combustion[94] are reported for the successful preparation of HEO NPs with different components and crystal structures.[95]

The properties of the synthesized HEMs, including the crystal structure, morphologies, elemental composition, distribution, and chemical states, are assessed through different material characterization techniques. The microstructure, morphology, and size of HEMs are mainly characterized by scanning electron microscopy (SEM), transmission electron microscopy (TEM), and high-angle annular dark-field scanning transmission electron microscopy (HAADF-STEM).[96–98] The crystallography and phase structure of materials are analysed by identifying the crystallographic peaks in the X-ray diffraction (XRD) test and electron diffraction patterns in the selected area diffraction (SAD) test. Furthermore, atomic scale HAADF-STEM and associated fast Fourier transform (FFT) analysis are advanced characterization tools to identify lattice planes, atomic lattice defects, and dislocations.[79,81] The chemical composition of HEMs is characterized by energy-dispersive X-ray spectroscopy (EDX) on a selected area by electron microscopy and X-ray photoelectron spectroscopy (XPS) for the elemental composition peaks near the surface.[26–28] Elemental mapping illustration by EDX is one of the most important tools for confirming the uniform distribution of constituent elements

in all multicomponent HEMs, especially for NPs in catalysis applications.[74,76,99–101] Inductively coupled plasma-optical emission spectrometry (ICP-OES) and inductively coupled plasma-mass spectroscopy (ICP-MS) are other tools for composition analysis of bulk samples.[76,101] XPS and X-ray absorption spectroscopy (XAS) are techniques used to determine the chemical states of the constituent elements on the surface of HEMs.[26–28]

5. High-entropy materials in catalysis and electrocatalysis applications

5.1 Electrocatalysis in fuel cells

Fuel cells are one of the most promising energy conversion devices with high efficiency and low pollution that generate an electric current through an electrochemical redox reaction. Anodic oxidation of hydrogen-rich fuels and cathodic reduction of oxygen demand highly active and corrosion-resistant electrocatalysts to improve the efficiency of fuel cells.[102] HEAs have been studied as potential electrocatalysts for the cathodic reduction of oxygen in different electrolyte media and for anodic oxidation of fuels in direct methanol fuel cells (DMFCs), direct formic acid fuel cells (DFAFCs) and direct ethanol fuel cell (DEFCs).

5.1.1 Methanol oxidation reaction (MOR). Improving the low power density of DMFCs related to the slow rate of the methanol oxidation reaction (MOR) at the anode surface is in great demand. One approach is developing highly active and cost-effective electrocatalysts. It is also essential for the catalyst materials to be corrosion resistant in the acidic electrolyte inside the cell.[102] Pt is a highly active noble metal catalyst for the MOR, but it has limitations due to its high cost and low abundance on the earth. Another issue with the Pt catalyst is the poisoning due to CO adsorption on its surface happening after methanol dehydrogenation, which can rapidly deactivate it.[103] Therefore, much effort has been made to solve this problem by alloying Pt with other elements. Several binary[104–110] (PtRu, PtFe, PtCo), ternary[104,105,111] (PtRuCo, PtRuOs) and quaternary[104,105,112,113] (PtRuIrOs, PtRuNiZr) Pt-based alloys with more and fewer improvements in catalysis performance have been reported in the literature.[114] Among all of them, binary PtRu alloys showed the highest activity due to their completely rapid oxidation mechanism.[108–110]

Taking the advantages of high-entropy multi-element alloys into consideration, Tsai *et al.*[103] developed a Pt-based HEA catalyst for the MOR. They fabricated Pt-based multi-element $Pt_{50}Fe_{11}Co_{10}Ni_{11}Cu_{10}Ag_8$ nanoparticles (NPs) with a single FCC solid solution structure by the radio frequency sputter deposition method. It was found that this multi-element alloy with less amount of Pt content exhibited higher MOR activity compared to the Pt catalyst alone. However, the performance of this alloy was still lower than that of $Pt_{43}Ru_{57}$. In another study, Tsai *et al.*[115] investigated the effect of Pt composition in the $Pt_x(FeCoNiCuAg)_{(100-x)}$ multi-element NPs on its MOR activity. Among four different compositions (x = 22, 29, 52, 56), $Pt_{52}Fe_{11}Co_{10}Ni_{11}Cu_{10}Ag_8$ showed the highest mass activity. It was again observed that the multi-element alloy has higher activity than those with Pt alone and lower activity than the binary PtRu alloy (Fig. 6a). Chen *et al.*[116] likewise compared the electrocatalytic activity of Pt-based HEAs fabricated by them with that of the commercial PtC catalyst. The nano-porous PtRuCuOsIr (np-PtRuCuOsIr) was synthesized by chemical dealloying of the mechanically alloyed AlCuPtRuOsIr precursor. From the electrochemical test results, a specific activity of 3 (mA cm^{-2}) for np-PtRuCuOsIr HEA was observed, which was six times higher than the value of 0.5 (mA cm^{-2}) obtained for the PtC catalyst. In a better comparison, mass activities (normalized by Pt loading) of 857.5 and 229.5 (mA mg^{-1}) for np-PtRuCuOsIr and PtC, respectively, indicate that the HEM nano-catalyst has about 3.7 times higher intrinsic activity towards the MOR (Fig. 6b). This result reflects the fact that HEAs containing Pt not only enhance the performance of DMFCs but also reduce the catalyst cost due to the lower amount of Pt element required. Another improved performance of HEAs for methanol electrooxidation is related to their higher CO tolerance compared to the commercial PtC catalyst, which makes them a more ideal electrocatalyst for DMFC application.

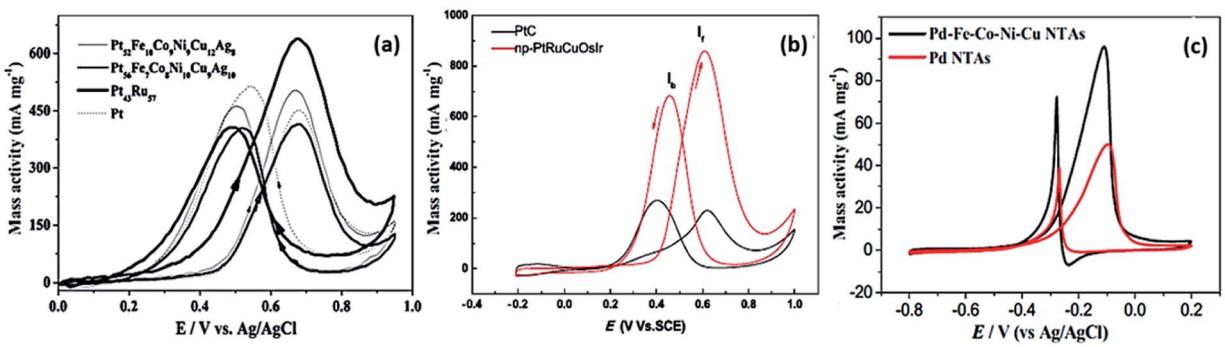

Fig. 6 Comparison of catalytic activities toward the MOR. Cyclic voltammetry curves in the mass activities of (a) $Pt_{56}Fe_7Co_8Ni_{10}Cu_9Ag_{10}$ NPs, $Pt_{52}Fe_{10}Co_9Ni_9Cu_{12}Ag_8$ NPs, Pt NPs, and $Pt_{43}Ru_{57}$ NPs (the 100th cycle) in 0.5 M H_2SO_4 + 1.0 M CH_3OH (reproduced with permission (ref. 115). Copyright 2009, Elsevier); (b) np-PtRuCuOsIr and PtC catalysts in 0.5 M H_2SO_4 + 0.5 M CH_3OH (reproduced with permission (ref. 116). Copyright 2015, Elsevier); and (c) PdNiCoCuFe NTAs and Pd in 1.0 M NaOH + 0.5 M CH_3OH (reproduced with permission (ref. 122). Copyright 2014, Elsevier) for methanol electrooxidation.

Among all active metals, palladium (Pd) is the closest metal to Pt, which is an attractive low-cost and more abundant option that can be replaced in Pt-based catalysts.[117,118] Similar to Pt-based alloys, alloying Pd with other active, cheap and stable transition metals can boost its activity.[119–121] Wang *et al.*[122] synthesized quinary PdNiCoCuFe alloy nanotube arrays (NTAs) by a template-assisted electrodeposition method and compared it with Pd NTAs for their performance in methanol oxidation. It is reported that the PdNiCoCuFe alloy NTAs exhibited considerably higher electrocatalytic activity relative to Pd NTAs (Fig. 6c). This enhancement in activity is attributed to the synergistic effect of multi-component systems and the electronic effects associated with alloys.

5.1.2 Ethanol oxidation reaction (EOR). A DEFC has theoretically high energy density due to the electrooxidation of ethanol at the anode which is a 12-electron/12-proton reaction with multiple dehydrogenation and oxidation steps.[123] However, designing a suitable catalyst with high selectivity for the 12-electron process to achieve the complete EOR is very challenging and of great interest. Most of the single Pd and Pt metals and their binary alloy catalysts have shown activity only toward the 4-electron transfer process.[124–126]

Wu *et al.*[127] evaluated the EOR performance of an HEA NP catalyst composed of six platinum group metals (RuRhPdOsIrPt) compared to the synthesized and commercial monometallic catalysts. The senary HEA with an FCC solid solution structure showed 2.5–30.1 times higher specific current density (normalized by the electrochemically active surface area (ECSA)) compared to all monometallic catalysts (Fig. 7a). More interestingly, the HEA catalyst at 0.6 V has 1.5 times higher mass activity than Au@PrIr/C which is the highest active catalyst reported for the EOR with a 12-electron process[128] (Fig. 7b). Comparing the CV curves of different mono- and multi-element catalysts revealed that not all these metallic elements have high EOR activity, but they can improve the adsorption/desorption of intermediate species and C–C breakage on the surface of the HEM catalyst. The HEM catalyst also demonstrated high stability during cycling in 1 M KOH electrolyte with ethanol and good activity retention over 50 cycles (Fig. 7c). The HEA with six elements has a more ideal surface configuration with various adsorption/desorption sites for intermediate species of the multistep EOR which can boost the selectivity of the 12-electron process and the overall efficiency of the EOR. This indicates that by more control on the effect of each element and compositional tuning, multi-element HEMs are potential catalysts for many other complex reactions.

5.1.3 Formic acid oxidation reaction (FAOR). The electrooxidation of formic acid to H_2 and CO_2 is the anodic reaction of DFAFCs, which can be achieved *via* direct or indirect competing pathways.[129] Different alloying and shape engineering strategies are applied to improve the efficiency of highly active Pt and Pd catalysts for industrial applications.[130–133] Katiyar *et al.*[134] studied the electrocatalyst performance of CuAgAuPdPt HEA NPs compared to the Pt NP catalyst for the FAOR. The ratio of the forward to reverse current of oxidation peaks (i_f/i_r) measured for the HEA was 1.47 and 3.5 times higher than that of Pt NPs (0.4). Also, analysis of the gas produced from the reaction catalysed by HEA NPs and Pt NPs showed that

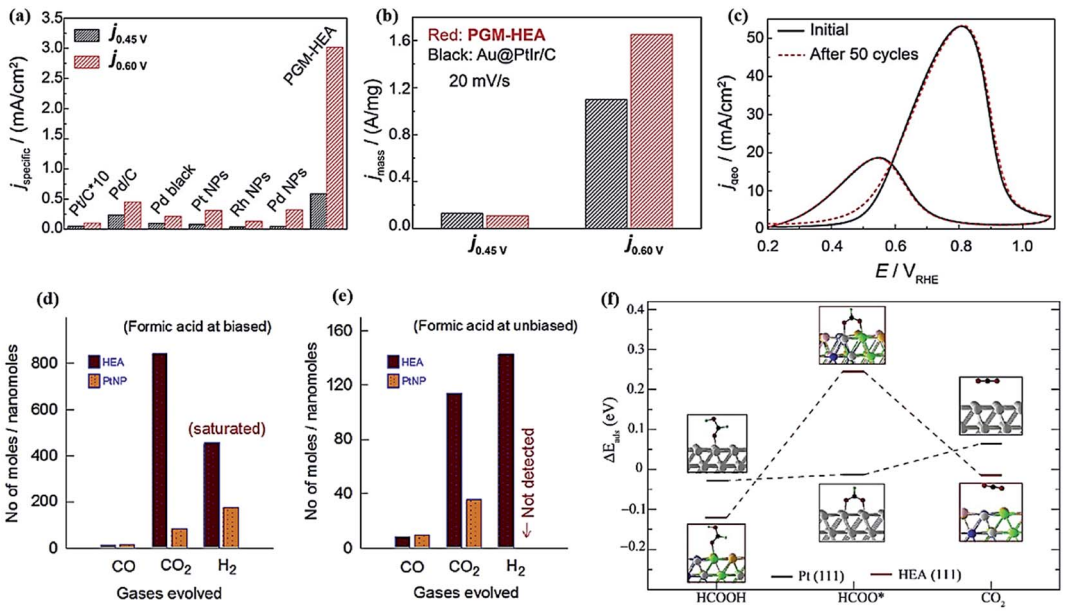

Fig. 7 Comparison of the (a) specific activities of RuRhPdOsIrPt HEA NPs (shown with the PGM-HEA label) with a monometallic catalyst, and (b) mass activity of HEA NPs (shown with the PGM-HEA label) with the Au@PtIr/C catalyst for the EOR at 0.45 and 0.6 V. (c) Performance stability of RuRhPdOsIrPt NPs in the EOR after 50 cycles. Reproduced with permission (ref. 127). Copyright 2020, American Chemical Society. Comparison of moles of gases produced on CuAgAuPdPt and Pt NP catalysts during the FAOR under (d) 0.7 biased and (e) unbiased (without energy input) conditions. (f) DFT calculated adsorption energies of the reactant (HCOOH), intermediate (HCOO*) and product (CO_2) of the FAOR on the (111) surface of pristine Pt and CuAgAuPdPt (shown with the HEA label) showing the mechanism of the catalysis reaction. Reproduced with permission (ref. 134). Copyright 2020, Elsevier.

a lower amount of CO is produced on the HEM catalyst (Fig. 7d and e). These results imply that the FAOR on the HEA is mainly dominated by the direct oxidation pathway. To explain the experimental results, the mechanism of the FAOR is also studied by DFT calculation of the adsorption energies of the reactant (HCOOH), intermediate (HCOO*) and product (CO_2) of the reaction on HEA and Pt (111) surfaces (Fig. 7f). It was revealed that the synergistic effect of different metallic elements in the HEM leads to a change in the d-band canter and adsorption energies of species on its surface compared to the pristine elements. The reaction profile shows that FAOR is exothermic on the HEA and endothermic on the Pt surface, which could be the reason for the higher activity of the HEM catalyst.

5.1.4 Oxygen reduction reaction (ORR). The oxygen reduction reaction (ORR) is the crucial cathodic reaction in fuel cells and demands a highly active electrocatalyst to overcome its overpotential and slow kinetics of either the 4-electron or 2-electron pathway.[135] Among all metal elements, Pt is known as the state-of-art electrocatalyst for the ORR due to its excellent catalytic activity and long-term stability in acidic and alkaline media of fuel cells.[136] However, the major limitations associated with its high cost and scarcity for feasible applications in commercialized fuel cells have led to research efforts to develop alternative low Pt loading or Pt-free electrocatalysts.[137] The volcano-like plots of catalytic activities and binding energies of metals are usually used to design new electrocatalyst alloys by predicting the activity based on the constituents and their compositions. However, such a prediction for a multi-component system is more complicated than the average calculated binding energies and activity of single metals.[136,137]

Löffler *et al.*[138] experimentally investigated the electrocatalytic activity of the well-known CrMnFeCoNi HEA (Cantor alloy) as a non-noble metal alloy toward the ORR. The quinary HEA NPs were synthesized by combinatorial co-sputtering into an ionic liquid and their electrocatalytic activity in alkaline media was compared to Pt as well as binary and quaternary alloys of the same elements. The interesting result revealed higher activity (lower overpotential) of the HEA NP catalyst composed of five equimolar inexpensive transition metal elements compared to that of the Pt catalyst. In contrast, the activities of all other quaternary and binary alloys were considerably lower than that of the Pt catalyst (Fig. 8a). These findings suggest that the HEA, with a homogeneous distribution of five different metals in a single-phase solid solution, provides a higher number of active sites for electrocatalysis.

Chen *et al.*[116] evaluated the catalytic activity of the np-PtRuCuOsIr HEA toward the ORR at the cathode in addition to the MOR at the anode, which was mentioned before (Section 4.1.1). The results from the ORR electrocatalytic activity measurement test in 0.1 M $HClO_4$ solution reveal a specific activity of 0.77 mA cm^{-2} and mass-specific activity of 0.249 A mg_{Pt}^{-1} for np-PtRuCuOsIr which are about 3.8 and 1.8 times higher than those of the commercial PtC, respectively (Fig. 8b). The durability of the np-PtRuCuOsIr was also tested in an acidic electrolyte (0.1 M $HClO_4$). After 10k and 15k cycles, specific activity retention was measured to be 90.3% and 73.1% of the initial value, respectively, and the corresponding mass activity retention was 70.2% and 50.0% (Fig. 8c).

Qiu *et al.*[139] proposed a combined method of arc-melting followed by fast cooling and dealloying from an Al-rich precursor for the preparation of equimolar senary np-

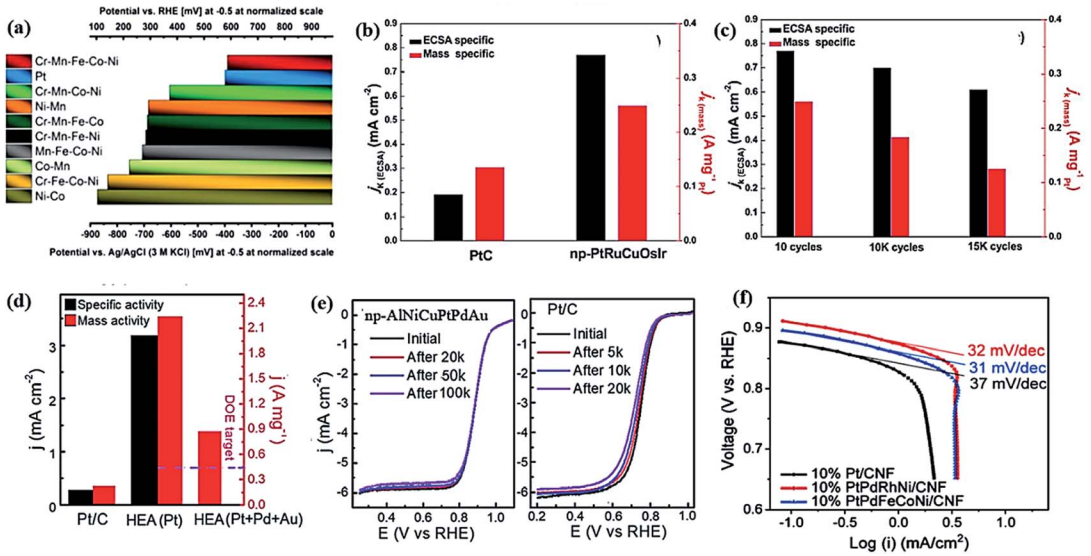

Fig. 8 Comparison of the catalytic activities of HEAs toward the ORR. (a) Overpotential at −0.5 V at the normalized scale for all sputtered NPs (Pt, binary, quaternary, and quinary Cr–Mn–Fe–Co–Ni). Reproduced with permission (ref. 138). Copyright 2018, Wiley-VCH. The ECSA-specific and mass-specific kinetic current densities at 0.90 V (*vs.* RHE) for (b) the np-PtRuCuOsIr and PtC catalysts; and (c) the np-PtRuCuOsIr after 10, 10k and 15k cycles. Reproduced with permission (ref. 116). Copyright 2015, Elsevier. (d) ECSA-specific and Pt mass-specific activities of Pt/C and HEA, and Pt + Pd + Au mass activities of the HEA at 0.9 V and (e) durability of np-AlNiCuPtPdAu and Pt/C after different cycles in O_2-saturated 0.1 M $HClO_4$. Reproduced with permission (ref. 139). Copyright 2019, Royal Society of Chemistry. (f) Tafel plots of ORR activities of PtPdRhNi, PtPdFeCoNi, and Pt catalyst in 1 M KOH. Reproduced with permission (ref. 140). Copyright 2020, National Academy of Science.

AlNiCuPtPdAu HEAs. The characterization tests demonstrated that the as-prepared np-AlNiCuPtPdAu is composed of uniformly distributed six different elements in the FCC solid solution structures of nano-ligaments. Also, the surface of nano-ligaments is coated with a very thin spinal oxide layer due to the natural surface oxidation of less noble metals in air. The fabricated np-HEA was examined for different electrocatalytic performances, including the electrocatalytic ORR. It was found that the specific activity and Pt mass activity of np-AlNiCuPtPdAu in an acidic electrolyte solution (O_2-saturated 0.1 M $HClO_4$) are 11.4 and 10 times higher than those of commercial Pt/C, respectively. Likewise, the activity of np-AlNiCuPtPdAu normalized by its total mass of precise metals (Pt, Pd, and Au) was found to be four times higher than that of Pt/C (Fig. 8d). Additionally, the HEA catalyst showed durability and long-term performance stability in an acidic environment after 100 000 CV cycles, while 35% loss of mass activity after 20 000 cycles was observed in Pt/C results (Fig. 8e).

Yao *et al.*[140] synthesized a series of ultrafine and homogeneously dispersed HEA NPs on a carbon support through a fast thermal shock method to explore their vast compositional design by controlling the formulation of precursor solutions. Two quaternary (PtPdPhNi) and quinary (PtPdFeCoNi) uniformly dispersed multi-metallic nanoclusters on carbon nanofiber (CNF) supports as optimized examples were screened for their activities for the ORR in 1 M KOH electrolyte compared to the control sample (Pt/CNF) by droplet cell analysis. Both HEA loaded samples exhibited lower overpotentials and better catalytic performances than the single metal Pt loaded catalyst. The Tafel plots of the three tested catalysts exhibit smaller slopes for HEAs/CNF than for Pt/CNF with a similar mechanism in the ORR (Fig. 8f). Batchelor *et al.*[141] presented a theoretical approach to predict the electrocatalytic activity of HEAs based on DFT calculated OH and O adsorption energies on random available binding sites on the surface of IrPdPtRhRu. Furthermore, the model works for the optimization of HEAs by adjusting the elemental compositions to increase the binding sites with the highest activities. According to this study, the large number of surface configurations provides the near-continuum adsorption energies on the surface of the HEA and makes it an inherently potential electrocatalyst for the ORR.

5.2 Electrocatalysts for hydrogen generation from water splitting

Hydrogen production by the water splitting method from different electric sources like solar photovoltaic (PV) and wind power is a simple and environment-friendly energy generation approach.[142,143] In this method, hydrogen and oxygen are generated by electrochemically splitting water molecules ($e^- + H_2O \rightarrow 1/2O_2 + H_2$) through the hydrogen evolution reaction (HER) on cathodes and oxygen evolution reaction (OER) on anodes.[144] However, water splitting efficiency is mainly limited by the electrolysis overpotentials and kinetics of the HER/OER and requires highly active electrocatalysts to enhance it.[145] Pt/Ru/Ir-based catalysts are known as the best theoretically active catalysts for these reactions, yet the high-cost and scarcity of the noble-metals are critical constraints to their practical large-scale applications.[146–148] Therefore, various transition-metal-based alloys as low-cost and nature abundant catalysts with comparable catalytic performances to that of noble-metal-based catalysts were developed and studied.[149–153] However, weak corrosion resistance and chemical stability of the materials in acidic and alkaline electrolytes are reported as the critical drawbacks for their applications.[154,155]

5.2.1 Hydrogen evolution reaction (HER). Inspired by the emergence of the new multi-element alloys with unique structural properties, phase stability, and corrosion resistance, Zhang *et al.*[156] investigated the catalytic performance of an HEA ($Ni_{20}Fe_{20}Mo_{10}Co_{35}Cr_{15}$) for the HER. In this work, the HEA samples were fabricated by an arc melting method with two different annealing temperatures of 800 °C and 1150 °C. The sample annealed at 1150 °C is a single FCC phase solid solution while the other one annealed at 800 °C shows the FCC phase plus μ phase precipitates. The results of the electrocatalytic activity of single-phase (FCC) and dual-phase (FCC + μ) samples for the HER in acidic electrolytes were compared together and to that of the commercial Pt catalyst. The single-phase HEA with lower onset potentials and smaller Tafel slope showed better performance than the dual-phase sample (Fig. 9a). Moreover, the electrochemical stability test of the HEA electrode in an acidic electrolyte (0.5 M H_2SO_4) demonstrated that the single FCC phase HEA works without activity degradation for 8 hours and is more durable than the dual-phase HEA (Fig. 9b). The superior electrocatalytic performances of the single-phase HEAs are mainly attributed to their disordered atom distribution, which provides a simple solid solution phase with higher coordination numbers. In addition to the effect of disordered surface atoms, the synergistic effect of under-coordinated atoms boosts the hydrogen adsorption on the electrode and facilitates the charge transfer required for the HER.

Liu *et al.*[157] synthesized ternary PtAuPd, quaternary PtAuPdRh, and quinary PtAuPdRhRu alloy NPs by co-reduction of metal ions with ethylene glycol under ambient conditions and tested their electrocatalytic HER performances in 1 M KOH solution. A lower Tafel slope of 62 mV dec^{-1} was obtained for HEA NPs compared to ternary (177 mV dec^{-1}) and quaternary (91 mV dec^{-1}) synthesized alloys as well as the commercial Pt catalyst (77 mV dec^{-1}) (Fig. 9c). Another HER electrocatalytic performance was reported by Qiu *et al.*[139] for their senary AlNiCuPtPdAu nano-porous HEA with an ultrafine structure and high specific area. The np-AlNiCuPtPdAu exhibited higher mass-specific activity normalized by the mass of Pt and mass of all the three metals (Pt, Pd and Au) compared to the commercial Pt/C catalyst (Fig. 9d). The np-HEA was also very stable in acidic electrolytes for 2000 CV cycles (Fig. 9e). Gao *et al.*[158] evaluated FeCoPdIrPt@GO NPs synthesized by a fast-moving bed pyrolysis method as a working electrode for the HER in 1 M KOH. This HEA electrode also demonstrated superior electrocatalyst performance to the commercial Pt/C electrode with a lower overpotential of 42 mV compared to 64 mV at the current density of 10 mA cm^{-2} and 26 times higher mass activity of 9.1 mA μg_{Pt}^{-1} compared to 0.35 mA μg_{Pt}^{-1} for Pt/C at an overpotential of 100 mV (Fig. 9f). Wu *et al.*[159] investigated the effect

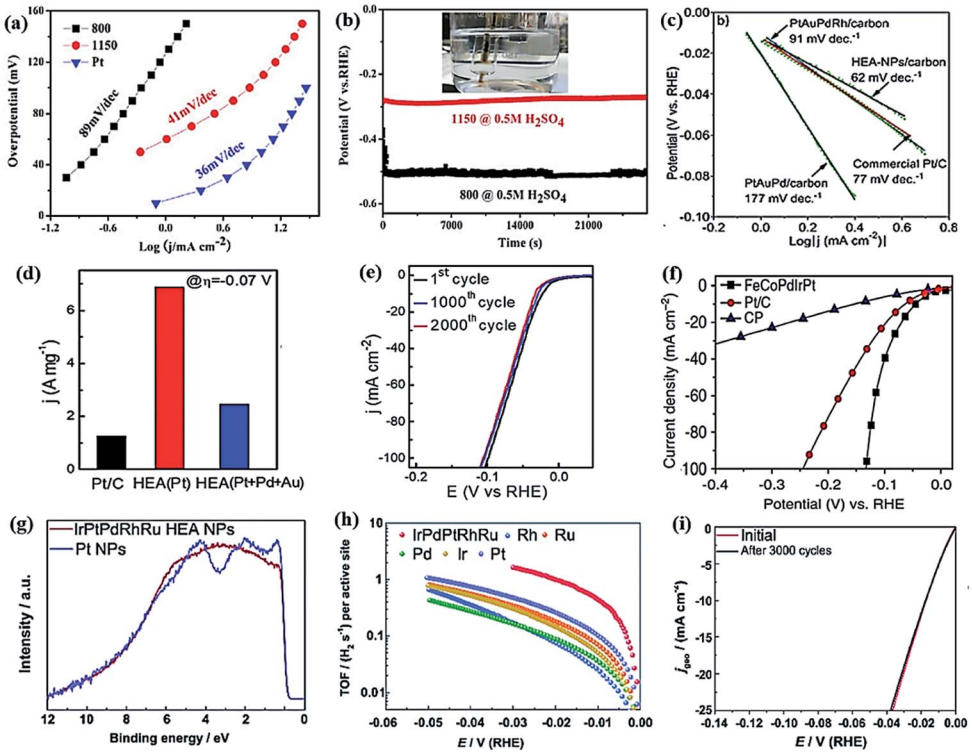

Fig. 9 Comparison of catalytic activity toward the HER. (a) Tafel plots and (b) electrochemical stability of single-phase (@1150) and dual-phase (@800) $Ni_{20}Fe_{20}Mo_{10}Co_{35}Cr_{15}$ catalysts in 0.5 M H_2SO_4 at room temperature. Reproduced with permission (ref. 156). Copyright 2018, Elsevier. (c) Tafel plots of PtAuPdRhRu HEM-NPs/carbon, PtAuPdRh/carbon, PtAuPd/carbon, and commercial Pt/C (Pt loading = 20 wt%) catalysts in 1 M KOH. Reproduced with permission (ref. 157). Copyright 2019, Wiley-VCH. (d) Pt and Pt + Pd + Au mass-specific activities at 0.07 V and (e) cycling stability of np-AlNiCuPtPdAu. Reproduced with permission (ref. 139). Copyright 2019, Royal Society of Chemistry. (f) Linear sweep voltammetry curve of FeCoPdIrPt@GO NPs and Pt/C (ref. 158). Comparison of (g) the valance band spectrum of IrPdPtRhRu and Pt NPs; and (h) TOF of IrPdPtRhRu NPs and monometallic NPs in 0.05 M H_2SO_4; (i) polarization curve of IrPdPtRhRu NPs at the initial cycle and after 3000 cycles. Reproduced with permission (ref. 159). Copyright 2020, Royal Society of Chemistry.

of the electronic structure of HEA NPs on the HER activity by measuring their valance band spectrum. IrPdPtPhRu NPs were synthesized through the co-reduction of the metal ions in an aqueous precursor solution sprayed into preheated triethylene glycol as the reducing agent. The valance band spectra of the HEM and Pt NPs were experimentally measured by hard X-ray photoelectron spectroscopy (HAXPES). It was observed that unlike Pt NPs, the valance band spectra of IrPdPtRhRu HEA NPs are broad and without any sharp peaks, which is because of their disordered atomic arrangements (Fig. 9g). The turnover frequency (TOF) test results revealed the higher intrinsic activity of IrPdPtRhRu NPs compared to the monometallic NPs (Fig. 9h) and cycling CV measurement proved their excellent performance stability in an acidic electrolyte (Fig. 9i).

5.2.2 Oxygen evolution reaction (OER). Similar to the idea of using the HEA catalyst for the HER, Dai *et al.*[114] reported the outstanding electrocatalytic performance of MnFeCoNi for the OER compared to highly active RuO_2 catalysts. The CV-activation of the HEA electrode fabricated by mechanical alloying results in the growth of nanosheets of MO_x (M = Mn, Fe, Co and Ni) compounds and forms a core–shell structure with much-enhanced surface area and active sites. The obtained electrode showed comparable activity performance to that of RuO_2 with a low overpotential of 302 mV at the current density of 10 mA cm^{-2} and the Tafel slope is only 83.7 mV dec^{-1} (Fig. 10a). Besides, the MnFeCoNi HEA working electrode exhibits stable activity in 1 M KOH electrolyte for 20 h (Fig. 10b).

Qiu *et al.*[160] prepared different nanoporous HEAs of non-noble metals by chemical dealloying of Al-rich precursor alloys with compositions of np-AlNiCoFeX (X = Mo, Nb, Cr). They selected highly OER active NiFe and NiCoFe alloys as the starting materials and then added other elements to further increase the compositional complexity to enhance the OER performance. From the Tafel plot, an increase in the number of elements improves the activity of the catalyst and OER kinetics (Fig. 10c). Furthermore, they tested the catalyst activity of quinary HEAs dissimilar in the fifth component to find the enhancing effect of different elements. This result showed that the addition of Mo, Cr and Nb has the highest to third highest catalytic enhancing effect, respectively. This is attributed to their preference for higher oxidation states, which can modify the strength of oxygen adsorption on the oxide surface (Fig. 10d). Moreover, it is demonstrated that incorporating a larger number of suitable metal species into the active binary and ternary alloys is an effective way to improve the OER catalysis as well as activity retention and durability of the catalyst over long-time cycling (Fig. 10e).

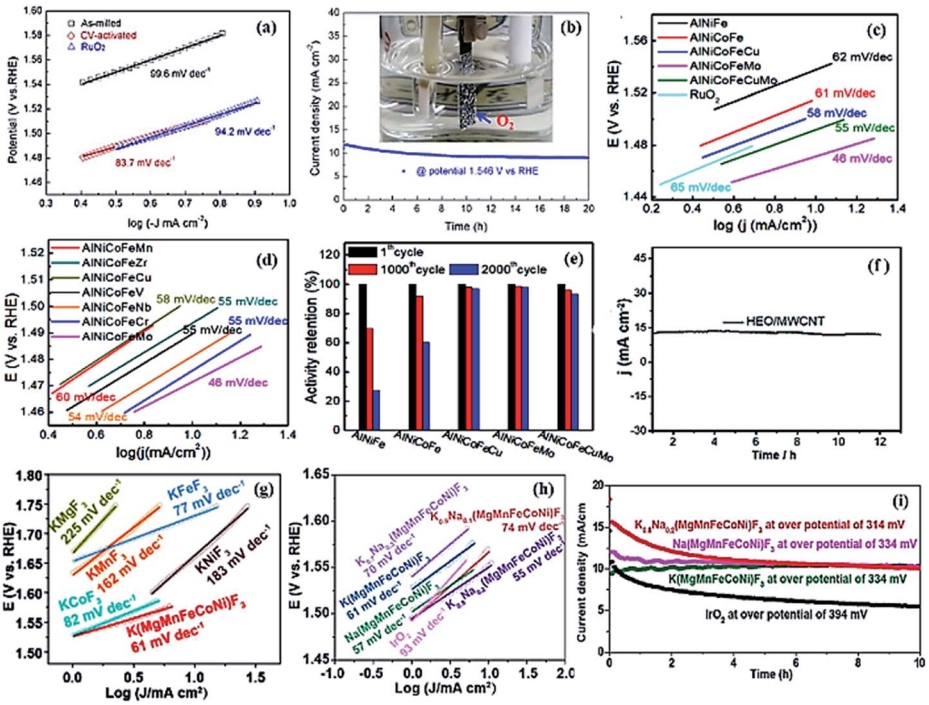

Fig. 10 Comparison of catalytic activity toward the OER. (a) Tafel plots for RuO_2, as-milled and CV-activated MnFeCoNi catalyst; and (b) electrochemical stability test of CV-activated MnFeCoNi HEM working electrode in 1 M KOH solution. Reproduced with permission (ref. 114). Copyright 2018, Elsevier. Comparison of (c) Tafel plots of different metallic np-HEMs, np-AlNiCoFe, np-AlNiFe, and RuO_2; (d) Tafel plot of metallic np-HEMs different in their fifth element; and (e) activity retention at 1.55 V after 1000 and 2000 cycles of different metallic np-HEMs, np-AlNiCoFe, np-AlNiFe, and RuO_2. Reproduced with permission (ref. 160). Copyright 2019, American Chemical Society. (f) Electrochemical activity retention of the HEO on a multiwalled carbon nanotube support (HEO/MWCNTs) at 1.58 V *vs.* RHE in 1.0 M KOH. Reproduced with permission (ref. 16). Copyright 2019, Royal Society of Chemistry. Comparison of Tafel plots for (g) perovskite fluorite HEM ($K(MgMnFeCoNi)F_3$) and other ABF_3 perovskite fluorites with a single metal at the B site; (h) perovskite fluorite HEMs with different compositions at the A site ($K_{1-x}Na_x$(-MgMnFeCoNi)F_3) and commercial IrO_2 catalyst in 1 M KOH solution. Reproduced with permission (ref. 27). Copyright 2020, American Chemical Society.

Wang *et al.*[16] reported the electrocatalytic activity of an HEO toward the OER. They prepared the high-entropy $(CoCuFeMnNi)_3O_4$ with a single-phase spinel structure ($Fd\bar{3}m$) and a very small particle size of 5 nm *via* a solvothermal synthesis followed by low-temperature pyrolysis at 400 °C. The synthesized nanoparticles loaded on multi-walled carbon nanotubes (MWCNTs) revealed excellent catalytic performance for the water oxidation reaction and reached a current density of 10 mA cm^{-2} at 1.58 V in 1 M KOH (Fig. 10f). More interestingly, the HEO supported on MWCNTs showed excellent stability in the alkaline test environment for 12 h without any decay in catalytic activity, which makes it a promising catalyst candidate for the OER in hydrogen generation from water splitting (Fig. 10f).

A new type of HEM was developed by Wang *et al.*[27] and studied as a catalyst for the OER. ABF_3 perovskite fluoride HEMs (HEPFs) were synthesized by combining the hydrothermal method with mechanochemistry. The catalytic activity of the synthesized $K(MgMnFeCoNi)F_3$ in 1 M KOH solution was first compared with all KMF_3 perovskite fluorides with a single metal at the B site. From the electrochemical test in 1 M KOH solution, it was found that $K(MgMnFeCoNi)F_3$ has higher catalytic activity and kinetics for the OER (potential of 369 mV at 10 $mAcm^{-2}$ and Tafel slope of 61 mV dec^{-1}) compared to all related KMF_3 perovskite fluorides with a single metal at the B site (Fig. 10g). The superior performance of fluorite HEMs is a result of their highly and randomly distributed active sites and low charge transfer resistance. Further activity improvement was observed by introducing sodium and modifying the composition of the A sites of ABF_3 type HEMs. Comparing the OER performances, $K_{0.8}Na_{0.2}(MgMnFeCoNi)F_3$ with a lower overpotential of 314 mV at a current density of 10 mA cm^{-2} and Tafel slope of 55 mV dec^{-1} exhibited the best performance among the different $K_{1-x}Na_x(MgMnFeCoNi)F_3$ HEMs as well as the commercial IrO_2 (Fig. 10h). Also, the stability of the catalysts at a constant potential for 10 h revealed that the fluorite HEM performs much better than commercial IrO_2 and $K_{0.8}Na_{0.2}(MgMnFeCoNi)F_3$ is able to maintain the current density above 10 mA cm^{-2} with lower overpotential than $K(MgMnFeCoNi)F_3$ and $Na(MgMnFeCoNi)F_3$ (Fig. 10i).

Zhao *et al.*[26] developed a phosphide type HEM and synthesized multi-elemental phosphide (HEMPs) nanosheets with Co, Cr, Fe, Mn and Ni metals in a single phosphide phase by the eutectic solvent method. The new HEMPs were evaluated as electrocatalysts for water splitting at both cathodic HER and anodic OER in alkaline media (1 M KOH solution). Commercial

Pt/C and commercial IrO_2 were used as control samples for the HER and OER, respectively. Electrochemical analysis revealed that HEMPs with lower overpotential (Fig. 11a) and Tafel slopes have higher electrocatalytic activity than single-metal phosphides for the HER and OER (Fig. 11b and c). For the OER, the phosphide HEM nanosheets with an overpotential of 320 mV and a Tafel slope of 60.8 mV dec^{-1} showed even better performance than commercial IrO_2 with the overpotential and Tafel slope of 440 mV and 75.8 mV dec^{-1}, respectively (Fig. 11a and b). In a more practical test, the excellent electrocatalytic activity of HEMP nanosheets for the overall water splitting process was tested in a two-electrode configuration in which phosphide HEM deposited on nickel foam was used as both cathode and anode. The electrocatalytic water splitting of the cell with phosphide HEM electrodes was compared with the other one with commercial Pt/C as the cathode and commercial IrO_2 as the anode. The cell with phosphide HEM electrodes with a lower potential of 1.78 V at the current density of 100 mA cm^{-2} exhibited superior performance to the cell with the commercial electrode coupled with a potential of 1.87 V at the same current density (Fig. 11d). Additionally, the phosphide HEM catalyst showed excellent stability and current retention for 24 h and only a slight current degradation of 1.2% was observed while it was run at the current density of 10 mA cm^{-2} (Fig. 11e).

Metal–organic frameworks (MOFs) composed of metal ions and organic group linkers with high surface area and active sites are attractive materials for catalytic and electrocatalytic reactions like the OER.[161,162] Zhao *et al.*[30] reported the synthesis of a high-entropy MOF (MnFeCoNiCu-MOF) from a solution of five equimolar metal ions and 1,4-benzenedicarboxylic acid (1,4-BDC) at room temperature (HE-MOF-RT) (Fig. 12a). Another multi-metallic MOF material was also prepared by the solvothermal method by heating the solution (HE-MOF-ST). The characterization of the synthesized material showed that the room temperature method gives a homogeneous and random distribution of metal ions of near equimolar composition and a high-entropy material is successfully formed. However, the one prepared by the solvothermal method gives unequal distribution of metal ions and aggregation of Fe ions, which indicates that the material is a polymetallic composite MOF and HE-MOF. The OER activity of HE-MOF was examined in alkaline solution (1 M KOH) and compared to that of the polymetallic MOF from the solvothermal method as well as the conventional RuO_2 catalyst. The obtained result revealed that the HE-MOF has a lower overpotential of 245 mV at a current density of 10 mA cm^{-2} and smaller Tafel slope of 54 mV dec^{-1} which are much smaller than those of HE-MOF-ST (293 mV and 81 mV dec^{-1}) and commercial RuO_2 (346 mV and 71 mV dec^{-1}) in alkaline systems (Fig. 12b). Moreover, the HE-MOF synthesized at room temperature with homogeneous distribution of elements showed higher activity retention compared to the one prepared by the solvothermal method and aggregated elemental distribution (Fig. 12c).

Huang *et al.*[29] employed a MOF templated method to synthesize sub-5 nm HEA particles on carbon cloth. The quinary metal MOF/CC precursor was pyrolyzed at 450 °C to form HEA NPs which are decorated on the porous structure by thin graphite linkers (Fig. 12d). The HEA NPs with an FCC crystal structure decorated on the porous structure of carbon linkers were tested as the electrocatalyst for the OER in 1.0 M KOH and compared to ternary and quaternary NP catalysts prepared by the same method. The result revealed that HEA NPs with a Tafel slope of 43 mV dec^{-1} showed enhanced activity compared to ternary and quaternary NP catalysts (Fig. 12e). The improved

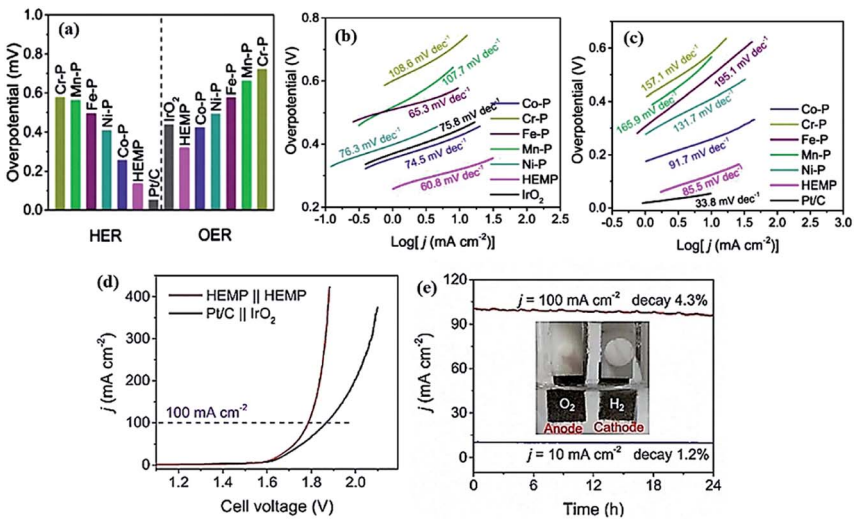

Fig. 11 Comparison of the electrocatalytic activity toward water splitting in 1 M KOH solution. (a) Overpotential of the phosphide HEM (labelled HEMP) electrocatalyst and individual metal phosphides at a current density of 10 mA cm^{-2} for the HER (left) and OER (right). Tafel plots of different electrode samples for the (b) OER and (c) HER. (d) Polarization curve of coupled phosphide HEM electrodes and coupled Pt/C–IrO_2 electrodes; (e) chronoamperometric curves of coupled phosphide HEM cathode and anode at the current density of 10 and 100 mA cm^{-2} with the inset showing the picture of the device working as the two-electrode configuration cell. Reproduced with permission (ref. 26). Copyright 2020, Wiley-VCH.

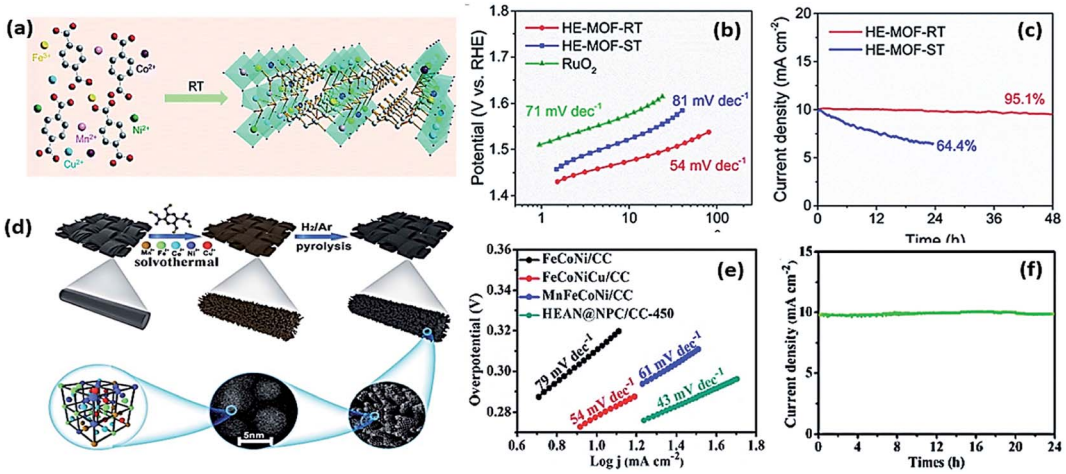

Fig. 12 (a) Schematic of high entropy MOF synthesized by the room temperature solution method; (b)Tafel plots of HE-MOF-RT, HE-MOF-ST and RuO_2 electrocatalysts for the OER test in O_2-saturated 1 M KOH electrolyte; and (c) chronoamperometric curves of HE-MOF-RT and HE-MOF-ST at a current density of 10 mA cm^{-2}. Reproduced with permission (ref. 30). Copyright 2019, Royal Society of Chemistry. (d) Schematic of MOF-template synthesis of HEA NPs on carbon cloth; (e) Tafel plots of FeCoNi/CC, FeCoNiCu/CC, MnFeCoNi/CC and HEAN@NPC/CC-450 electrocatalysts for the OER test in O_2-saturated 1 M KOH electrolyte; and (f) current density retention of HEAN@NPC/CC-450 over time. Reproduced with permission (ref. 29). Copyright 2020, Royal Society of Chemistry.

OER activity and low overpotential of the HEA NP catalyst are attributed to the atomic defect in the structure observed by HRTEM and high surface tension associated with that. Besides the higher catalytic activity, the HEA NPs showed long term stability and good activity retention for over 24 h (Fig. 12f).

5.3 Catalysts for CO oxidation

The catalytic oxidation of CO concentrated on the surface of the catalyst is the primary key to air purification from this toxic gas.[163] Precious metals like Pt, Ru and Au are the highest active materials for this surface reaction, but their high price is an inevitable limitation for practical applications.[164,165] Oxides of transition metals like Co, Mn and Cu are also known to be suitable catalysts for CO oxidation because of their high oxygen content which can inhibit the rate-limiting step for the reaction and allow the active site of metals to work under cycling conditions.[163,166] Developing highly active, long-term functional, high-temperature stable and cost-effective catalysts or support materials with the capability of good dispersion of noble metal atoms on their active sites is one attractive field of research in the catalysis area.[167–173]

The newly developed HEOs are highly stable at high temperature due to the temperature dependence of entropic contribution to Gibbs free energy.[9] This unique property, along with the disordered multicomponent cation sites in their structure, was the inspiration to consider them as a new type of catalyst system.[174,175] Chen *et al.*[174] showed the possibility of designing an HEO-supported noble metal catalyst system for CO oxidation. The homogeneous entropy-stabilized mixed metal oxide solid solution of (NiMgCuZnCo)O can not only act as an active catalyst itself but is also an excellent support to randomly disperse and stabilize Pt atoms. The 0.3 wt% Pt/(NiMgCuZnCo)O showed high activity for CO oxidation (100% conversion at 155 °C) due to highly dispersed active sites and extreme thermal stability (900 °C) owing to the entropy-stabilized behavior inside the metal oxide (Fig. 13a). Okejiri *et al.*[176] similarly reported a Ru atom dispersed perovskite HEO nanoparticle catalyst for CO oxidation. $BaSrBi(ZrHfTiFe)O_3$ (HEPO-7), $Ru/BaSrBi(ZrHfTiFe)O_3$ (Ru/HEPO-7) and $BaRuO_3$ obtained by a sonochemical-based synthesis method were tested for CO oxidation performance at ambient pressure. It was observed that Ru/HEPO-7 with only 0.2 wt% Ru displays much higher activity than $BaRuO_3$ with 53 wt% Ru and can reach 100% CO conversion at 118 °C (Fig. 13b). HEPO-7 without Ru did not exhibit good catalytic activity which shows that Ru metal is the main active site of the catalyst and its high dispersion in the high-entropy phase resulted in the superior catalytic activity of Ru/HEPO-7. Xu *et al.*[177] synthesized an entropy-stabilized single-atom Pd catalyst on a $(CeZrHfTiLa)O_x$ fluorite HEO support *via* mechanical milling with fumed silica followed by calcination at 900 °C and etching silica with NaOH. The CO conversion activity of fluorite HEO doped with 1 wt% Pd (Pd_1@HEFO) was tested and compared with the activity of 1 wt% Pd doped CeO_2 (Pd@CeO_2) synthesized by the same method. It was observed that Pd_1@HEFO has an onset temperature of 80 °C and 100% CO conversion temperature of 170 °C which are considerably lower than 223 °C and 253 °C for Pd@CeO_2, respectively (Fig. 13c). The CO oxidation measurements in the cycling experiments and long-term stability test at 170 °C also demonstrated the excellent activity retention and high-temperature stability of the Pd doped HEO catalyst (Fig. 13d). Different characterization test results showed that Pd atoms are homogeneously incorporated on both the surface and in the bulk phase of fluorite HEO with the existence of Pd–O–M (M = Ce, Zr or La) and no agglomeration. The enhanced reducibility of lattice oxygen on the surface and higher oxygen vacancies of the HEO carrier after incorporation of Pd atoms in

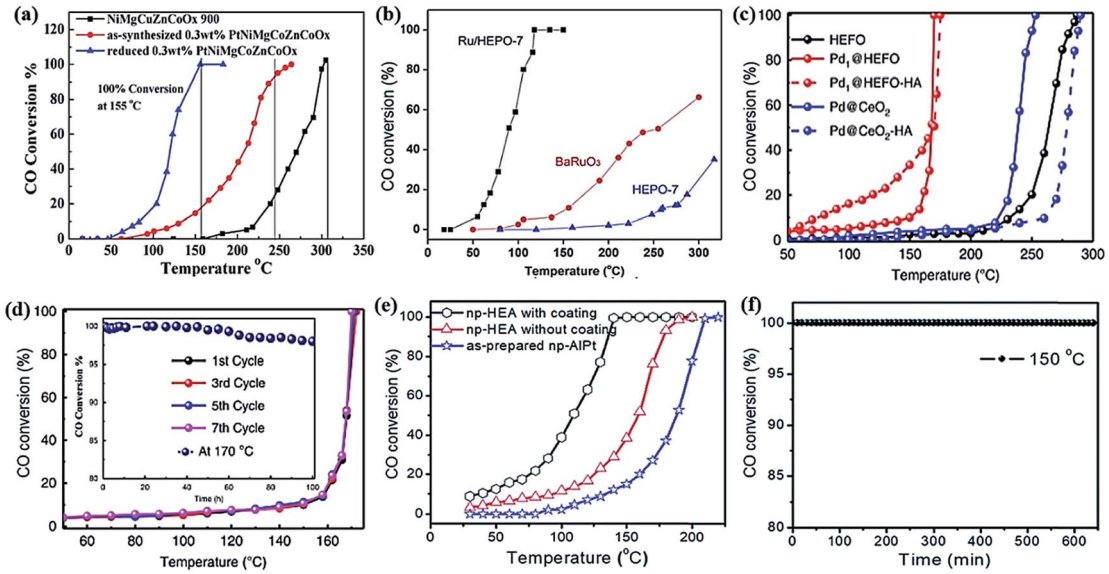

Fig. 13 Comparison of the catalytic activities toward CO oxidation. CO conversion as a function of the reaction temperature over (a) rock-salt HEO ($NiMgCuZnCoO_x$) and 0.3 wt% Pt doped HEO ($PtNiMgCuZnCoO_x$) (reproduced with permission (ref. 174). Copyright 2018, Royal Society of Chemistry); (b) perovskite HEO ($BaSrBi(ZrHfTiFe)O_3$ shown with the HEPO-7 label), 0.2 wt,% Ru doped HEO (Ru/HEPO-7) and $BaRuO_3$ (reproduced with permission (ref. 176). Copyright 2019, Wiley-VCH); (c) fluorite HEO ($CeZrHfTiLaO_x$ shown with the HEFO label), 1 wt% Pd doped HEO (Pd_1@HEFO) and 1 wt% Pd doped CeO_2 (Pd@CeO_2) (ref. 177); (d) 1 wt% Pd doped HEO for seven cycles (inset shows the CO conversion performance stability of the catalyst at 170 °C for 100 h) (ref. 177); and (e) np-AlNiCuPtPdAu with and without oxide coating and np-AlPt. Reproduced with permission (ref. 139). Copyright 2019, Royal Society of Chemistry. (f) CO oxidation durability of np-AlNiCuPtPdAu with oxide coating at 150 °C. Reproduced with permission (ref. 139). Copyright 2019, Royal Society of Chemistry.

the lattice are reported to be the main reasons for its superior catalytic activity.

Qiu *et al.*[139] examined the catalytic activity of the equimolar senary AlNiCuPtPdAu np-HEM with an ultrafine structure and high specific area toward CO oxidation. The as-synthesized np-AlNiCuPtPdAu was coated with a very thin spinal oxide layer due to the natural surface oxidation of the less noble metals in air. Therefore, the catalytic activity of the metallic np-AlNiCuPtPdAu with oxide coating and after removing the thin oxide layer was tested and compared with that of the np-AlPt binary alloy with high Pt content under the same conditions. The np-AlNiCuPtPdAu samples with the removed oxide layer showed better catalytic performance compared to np-AlPt (Fig. 13e) and excellent coarsening resistance at high temperature due to the slow diffusivity aspect of multi-element solid solutions. A comparison of results for all samples demonstrated that np-HEA with a thin oxide coating has higher activity than the other two tested samples and reaches 100% conversion rate at a lower temperature (Fig. 13c). Additionally, the catalyst stays active for a long time, with no efficiency decay at the operation temperature of 150 °C (Fig. 13f). This is known to be a favorable result in the field of catalysis wherein the oxide coating layer shows an enhancement effect on the catalytic activity of a metallic core catalyst in addition to providing better thermal stability at high temperatures. The high efficiency of np-HEAs with oxide coating is attributed to the oxygen source on their surface resulting from O_2 dissociation as well as the role of the oxide layer in stabilizing ultrafine nano-ligaments in order to prevent them from losing active sites during the reaction time. Interestingly, the oxide-coated alloy is highly active without any high-temperature activation step needed, unlike other np-Au or Pt-based alloys coated with Al_2O_3 or TiO_2 layers.

5.4 Catalysts for ammonia decomposition

Catalytic decomposition of ammonia is a promising route for hydrogen storage applications.[178,179] The main limitation of the large-scale application is related to the cost of the ruthenium (Ru) as the conventional metal catalyst.[180–182] Researchers' efforts to find a low-cost and earth-abundant replacement catalyst for this process led to the finding of the bimetallic Co–Mo alloy as the best option.[183,184] However, the existence of a large miscibility gap in the phase diagram of this binary alloy limits the range of its functional composition.[185–188]

Recently, Xie *et al.*[76] investigated the idea of using quinary CoMoFeNiCu HEA NPs for the decomposition of ammonia and compared it with Co–Mo and conventional Ru metal catalysts. The quinary HEA NPs with five different Co/Mo composition ratios were synthesized by a carbothermal shock technique and all formed single-phase solid solutions. This indicates that the addition of other metals and multi-element alloying can resolve the issue related to the miscibility gap of Co–Mo. Evaluation of the performance of HEA catalysts with various Co–Mo ratios toward catalytic NH_3 conversion at different temperatures demonstrates that all the HEAs display higher performances than bimetallic Co–Mo (Fig. 14a). Among five HEA catalysts, the second Mo rich sample (HEA-$Co_{25}Mo_{45}$) with a Co/Mo ratio of 25/45 showed the highest activity (Fig. 14a). Besides, comparing the reaction rate at 500 °C with different catalysts showed that

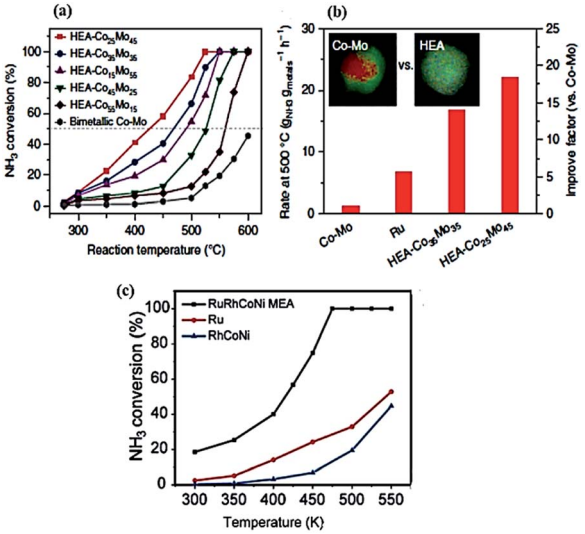

Fig. 14 Comparison of catalytic activities toward NH_3 decomposition. (a) NH_3 conversion of different HEA-Co_xMo_y nanoparticles and bimetallic Co–Mo (Co/Mo = 25/45) depending on the reaction temperature; (b) reaction rates of bimetallic Co–Mo, Ru, and HEA-Co_xMo_y catalysts (T = 500 °C). Reproduced with permission (ref. 76), Copyright 2019, Springer Nature; (c) NH_3 conversion of RuRhCoNi compared to Ru and RhCoNi. Reproduced with permission (ref. 101). Copyright 2020, American Association for the Advancement of Science.

the best HEA sample in this work is about 4 and 12 times more active than bimetallic Co–Mo and monometallic Ru catalysts, respectively (Fig. 14b). Yao *et al.*[101] recently compared the catalytic activity of $Ru_{0.44}Rh_{0.30}Co_{0.12}Ni_{0.14}$ NPs synthesized by the electrical Joule heating method and compared it with those of Ru and RhCoNi as control samples. Interestingly, superior performance was observed for the HEA catalyst and 100% NH_3 decomposition was achieved at 470 °C (Fig. 14c).

5.5 Catalysts for CO_2 conversion

CO_2 reduction to CO by H_2 through a heterogeneous catalytic reaction is one of the promising ways for atmospheric CO_2 utilization. Chen *et al.*[175] presented a new method of synthesizing an HEO-supported noble metal catalyst at ambient temperature (Fig. 15a). The advantages of this catalyst system are reducing the amount of precious metal used as well as decreasing the activation temperature of the catalyst. The mechanochemically synthesized (NiMgCuZnCo)O doped with 5 wt% Pt showed high CO_2 conversion, CO yield and selectivity as well as stable performance for 20 h (Fig. 15b). Pedersen *et al.*[189] recently conducted a DFT analysis to study the catalytic activity of HEAs for CO and CO_2 reduction by predicting the CO and H adsorption energies on the surface of two HEAs, CoCuGaNiZn and AgAuCuPdPt as examples. Use of this method showed how the distribution of adsorption energies is affected by tuning the composition with different affinities for H_2 formation and CO reduction, which provides a way to predict and optimize the compositional distribution of HEAs to improve their catalytic activity towards different reactions.

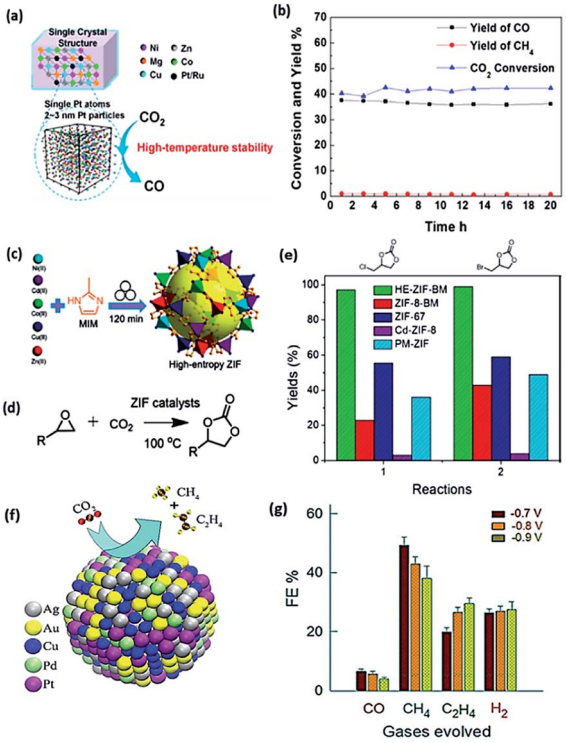

Fig. 15 (a) Schematic of the Pt/Ru-(NiMgCuZnCo)O entropy-stabilized metal oxide solid solution synthesized by mechanical ball milling; (b) CO_2 hydrogenation stability of 5 wt% Pt doped HEO at 500 °C for 20 h. Reproduced with permission (ref. 175). Copyright 2019, American Chemical Society. Schematic of (c) ZIF HEM synthesized by the mechanochemistry method; (d) catalytic cycloaddition of CO_2 with epoxides to produce cyclic carbonates; and (e) yields of two cyclic carbonates obtained from the cycloaddition of CO_2 with corresponding epoxides catalysed by HE-ZIF-BM, ZIF-8-BM, ZIF-67, Cd-ZIF-8, and PM-ZIF. Reproduced with permission (ref. 190). Copyright 2019, Wiley-VCH. (f) Schematic of CO_2 conversion to hydrocarbon fuels on the Cu-based HEA catalyst; (g) bar diagram for the faradaic efficiencies of carbonaceous species and hydrogen gaseous products of the reaction. Reproduced with permission (ref. 191). Copyright 2020, American Chemical Society.

Xu *et al.*[190] reported the synthesis of a zeolitic imidazolate framework HEM (HE-ZIF) at room-temperature by a mechanochemistry method. HE-ZIF is composed of five transition metal cations, Zn^{2+}, Co^{2+}, Cd^{2+}, Ni^{2+}, and Cu^{2+} dispersed in the ZIF structure (Fig. 15c). The catalytic performance of the HE-ZIF for CO_2 cycloaddition with epoxides to produce cyclic carbonates (Fig. 15d) was examined under 10 bar CO_2 pressure at 100 °C for 8 h and compared with other reported active single-metal ZIF-type catalysts. The reaction yields catalyzed by the HE-ZIF, 97.2% for 2-(chloromethyl)oxirane and 99.0% for 2-(bromomethyl)oxirane, were interestingly higher than that of other single-atom ZIF catalysts due to the synergistic effect of the five metal ions as a Lewis acid in epoxide activation (Fig. 15e).

Another important process related to CO_2 conversion is electroreduction of CO_2 into hydrocarbon fuels. While many noble metal catalysts like Ag, Au, Pd and Pt have shown high selectivity for CO in the catalytic reduction of CO_2, Cu-based catalysts have shown selectivity towards other hydrocarbons.

Nellaiappan *et al.*[191] have studied the electroreduction of CO_2 to gaseous hydrocarbons by a Cu-based HEA catalyst (Fig. 15f). AgAuCuPdPT HEA was synthesized by melting and cryo-milling with a single FCC crystal structure and homogeneous distribution of elements. The HEA is considered as a single atom catalyst when Cu is the active metal catalyst and other metals have a synergistic effect on Cu catalytic activity. The electroreduction of CO_2 is tested in CO_2-saturated K_2SO_4 electrolyte solution with HEA as the working electrode and Pt as the counter electrode. Evaluation of gashouse products by gas chromatography has shown 100% faradaic efficiency of the gashouse product and higher selectivity to hydrocarbon fuels such as CH_4 and C_2H_4 compared to CO and H_2 at a low applied potential of 0.9 V *vs.* Ag/AgCl (0.3 V *vs.* RHE) (Fig. 15g).

5.6 Catalysis for azo dye degradation

Azo dyes, organic compounds with an R–N=N–R functional group, are widely used in many industries such as textiles, cosmetics, and food. The release of stable dyestuff existing in the effluents of these industries causes pollution of the environment.[192] Therefore, much effort has been made to investigate an efficient approach for the degradation of azo dyes.[193–199] Degradation by zero-valent metals is one of the low-cost and simple methods generally used in industrial applications.[200–203] The main limitation of this method is the low corrosion resistant of zero-valent metals in water, which can rapidly reduce their efficiency.[204] Metallic glasses are other investigated materials with thermodynamically stable structures and good capability for azo degradation.[205–207] However, the synthesis of metallic glasses involves several conditions and processes, which makes it less cost-effective and favorable for commercial applications.[208] Herein, there is a need to find and develop new highly stable and low-cost materials with simple preparation methods for the degradation processes of different azo dyes.

In this regard and after the reported progress in high-entropy alloys and their outstanding features, Lv *et al.*[208] worked on the HEA for azo degradation. They synthesized three HEA samples AlCoCrTiZn (S_1), AlCoCrFeNi (S_2), and CoCrFeMnNi (S_3) by the mechanical alloying method and tested their performances in the degradation of Direct Blue 6 (DB_6, $C_{32}H_{20}N_6S_4O_{14}Na_4$). The degradation efficiency was evaluated by plotting the normalized intensity of the DB_6 concentration at 25 °C as a function of reaction time (Fig. 16a). Based on the comparison between the three HEA samples tested in this work, S_1 has a higher efficiency in the degradation of DB_6 than S_2 and S_3. Furthermore, the performances of the S_1 and metallic glass powders were compared simply in terms of the t_0 value, which is the time in which the concentration intensity decreases to the initial condition (Fig. 16b). The obtained result indicates that the AlCoCrTiZn powder with $t_0 = 0.83$ min has very low efficiency compared to the best reported metallic glasses (BM MgZn glassy powder) with $t_0 = 0.78$ min. It can also be seen that the efficiency of S_1 is about 20 times higher than the BM Fe-based glassy powder (BM G-Fe, $t_0 = 16$ min), which is reported to be 200 times faster than that of the commonly used commercial Fe powder. The outstanding performance of the HEA is attributed

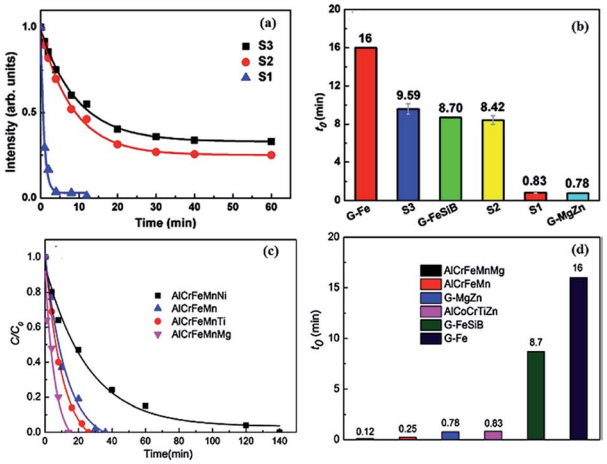

Fig. 16 Comparison of catalytic activity toward azo dye degradation. Comparison of DB_6 degradation efficiency at 25 °C of (a) S3, S2 and S1 by the normalized concentration as a function of degradation time; and (b) S1, S2, S3, MgZn and Fe-based glassy powders in terms of the t_0 value. Reproduced with permission (ref. 208). Copyright 2019, Springer Nature. Comparison of the discoloration efficiency of (c) AlCrFeMn and AlCrFeMnM (M = Mg, Ti, Ni) with respect to concentration change over time; and (d) AlCrFeMn, AlCrFeMnMg and BMG-MgZn, AlCoCrTiZn, G-FeSiB and BM G-Fe as a function of the t_0 value. Reproduced with permission (ref. 209). Copyright 2019, Elsevier.

to its unique atomic structure with high lattice distortion, specific chemical compositions, and large available surface area. Later, Wu *et al.*[209] investigated the effect of the composition and particle size of HEAs on their efficiency toward the decolorization of DB_6. To select suitable elements for HEAs with high efficacy, they chose Al, Cr, Fe, Mn, Ti, Zn and Co metal elements with high activity. Among them, elements with a BCC structure are more favorable as the BCC phase is more brittle, and finer powders can be synthesized by the ball milling method. In this regard, they selected AlCrFeMn as their main sample and AlCrFeMnM (M = Mg, Ti, Ni) samples to find the effect of adding a different fifth element. Comparison of the normalized concentration of the dye as a function of temperature for the four synthesized HEA samples showed that the addition of Ti and Mg to AlCrFeMn can improve the efficiency and AlCrFeMnMg shows the best performance among all samples (Fig. 16c). Moreover, the comparison of t_0 of the highly active samples with that of previous studies shows that their performances are considerably higher than those of metallic glass powders (Fig. 16d).

5.7 Catalysts for carbon nanotube growth

There are various methods for the growth of carbon nanotubes (CNTs) and catalytic pyrolysis is one simple and efficient route. Lal and Sundara[210] showed that HEO NPs themselves could efficiently play a catalytic role in the growth of CNTs to form HEO–CNT nanocomposites. The as-synthesized HEO (Ni, Fe, Co, Cr, and Al-based) NPs *via* a simple sol–gel auto-combustion technique were used as a catalyst for the CVD growth of multiwalled CNTs with acetylene gas as the carbon precursor. The

yield of as-grown CNTs in the form of the HEO–CNT nanocomposite and reduced HEO–CNTs (by passing H_2 to reduce surface oxygen) was exceptionally high compared to the previous reports.

6. High-entropy materials in electrochemical energy storage application

Following the pioneering work on the development of the first HEO,[9] Bérardan *et al.*[85,211,212] studied the electrochemical properties of this material. It was first reported that (CoCuMgNiZn)O substituted with aliovalent dopants (*e.g.*, Li^+, Na^+, K^+) shows colossal dielectric constants and the charge compensation mechanism of aliovalent dopant incorporation into a single-phase rock salt structure of HEO was discussed.[85,211] However, the most promising property of HEOs, which makes them a new potential material for lithium-based batteries, is their superior Li-ion conductivity at room temperature.[148] This group showed that 30% Li-doped (CoCuMgNiZn)O has an ion conductivity of 10^{-3} S cm^{-1}, which is five orders of magnitude higher than that of pristine HEO (10^{-8} S cm^{-1}) (Fig. 17a). This indicates that by incorporating sufficient ions into the HEO structure, they can show higher conductivity than LIPON at room temperature (Fig. 17b). These findings have inspired many recent studies on the performance of high-entropy materials in electrochemical energy storage devices.

6.1 HEO as an anode material in Li-ion batteries

Transition metal oxides (TMOs) as active anode materials have been widely studied for new lithium-ion batteries due to their larger theoretical capacities compared to conventional graphite anodes.[213–216] However, their solid structures change severely after cycling and result in rapid capacity decay and limit their applications for long-term stable and efficient batteries. The development of entropy stabilized metal oxides with their excellent Li-ion conductivity received attention recently for use as conversion anode materials in Li-ion batteries.[217–219] Sarkar *et al.*[217] tested (CoCuMgNiZn)O with a rock-salt crystal structure as a conversion-based electrode material in a half coin cell with lithium metal and showed that it can be cycled over 500 times without capacity fading (Fig. 18b). The increase in capacity over cycling is the typical electrochemical behavior of conversion-based electrodes and is related to the activation process of large particles of the material. Moreover, they showed the importance of the entropy-stabilization concept in the material performance and cell cycling by testing each 4-cation oxide (medium entropy oxide) in the same system (Fig. 18c). The rapid capacity degradation of cells with medium entropy oxides indicates that the high configurational entropy (1.61*R*) of the five-cation system is the main factor for the stable structure of the electrode material and its cycling stability. Preservation of the rock-salt structure over cycling and during lithiation/de-lithiation processes was observed experimentally and is described as the main reason for the cycling stability of the material. It is explained that while some of the cations in the lattice are involved in the conversion reaction and are reduced to metals, the other uninvolved non-reduced cations are responsible for holding the structure and trapping the reduced metals inside the lattice (Fig. 18d).

In other relevant studies, (CoCuMgNiZn)O NPs were investigated by Qiu *et al.*[219] as anode materials in coin cells and compared with the Co_3O_4 anode as the reference material. Interestingly, the HEO with a high reversible capacity of 920 mA h g^{-1} at 100 mA g^{-1} after 300 cycles performed better than Co_3O_4 with a lower specific capacity and only 79% capacity retention (Fig. 18e and f). The difference in the performance and mechanism was analyzed by studying the surface morphology and crystal structure of anode material nanoparticles. A significant change in morphology and large cracks were detected on the surface of Co_3O_4 after several cycles, which is attributed to the agglomeration of nanoparticles and change in the overall crystallinity of the material. In contrast, no significant structural change was detected on the surface of the HEO after repeated cycling (Fig. 18g). It is proposed that the presence of inactive MgO along with the lattice distortion and entropy-stabilization features of the HEO prevent the particle agglomeration and morphology change and lead to long cycling performance of the anode material.

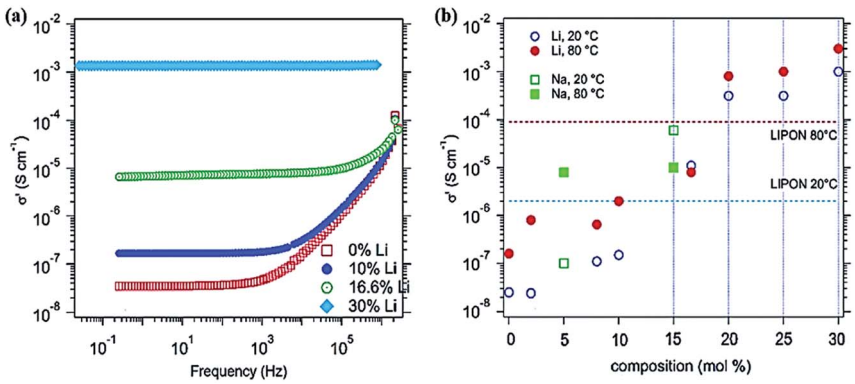

Fig. 17 Ionic conductivity of (a) Li doped (CoCuMgNiZn)O samples at room temperature (b) Li and Na doped (CoCuMgNiZn)O samples compared with LIPON. Reproduced with permission (ref. 148). Copyright 2016, Royal Society of Chemistry.

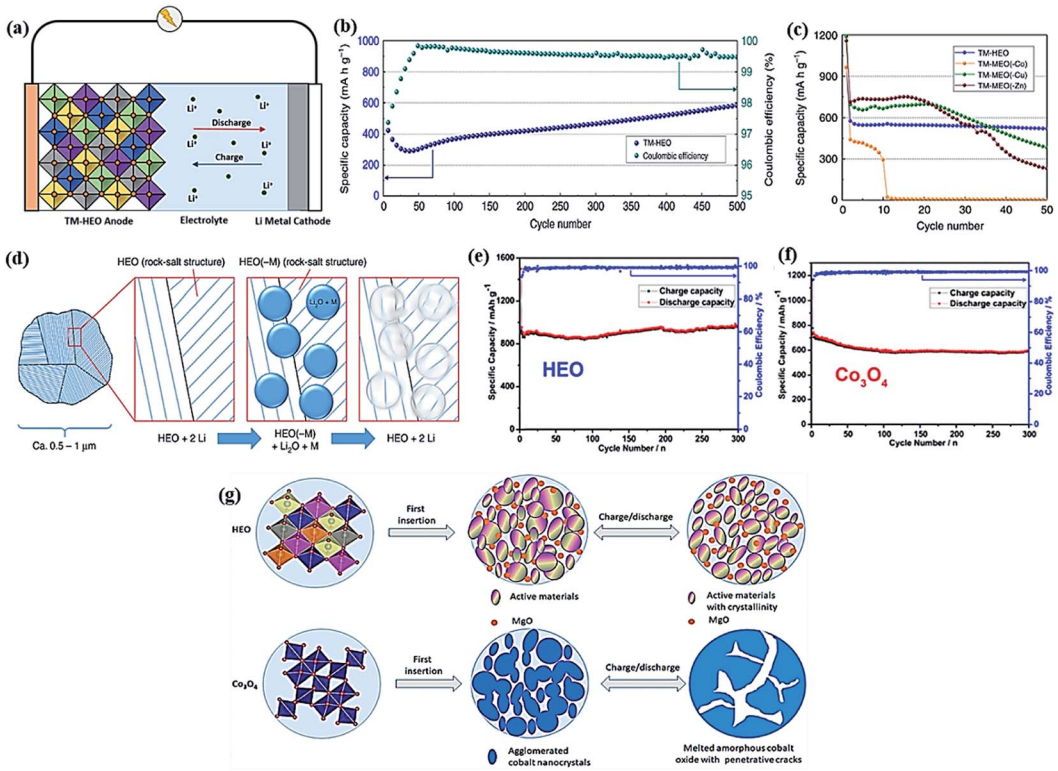

Fig. 18 (a) Schematic of a Li-ion half-cell with a TM-based HEO at the anode. Cycling performance of (b) the calcined HEO at 200 mA g^{-1} with the corresponding coulombic efficiency; and (c) HEO with five metallic elements (labelled TM-HEO) and other mixed metal oxides with four metallic elements (labelled TM-MEO). Reproduced with permission (ref. 217). Copyright 2018, Springer Nature. (d) Schematics of the (de)lithiation mechanism of active cations (Co, Cu, Zn and Ni) inside (CoCuMgNiZn)O with a poly/nanocrystalline structure during the conversion reaction. Reproduced with permission (ref. 217). Copyright 2018, Springer Nature. Cycling performance and the corresponding coulombic efficiency of the (e) HEO electrode and (f) Co_3O_4 electrode at 100 mA g^{-1} during 300 cycles. Reproduced with permission (ref. 219). Copyright 2019, Elsevier. (g) Schematic of the HEO and Co_3O_4 electrode changes over cycling. Reproduced with permission (ref. 219). Copyright 2019, Elsevier.

Testing the electrode material in half-cells with a Li counter electrode provides excess available Li, while in the full-cell configuration, the limited Li content of the cathode material is responsible for supplying Li for reactions.[220] Herein, Wang *et al.*[218] evaluated the performance of HEOs as an anode material in a full-cell with $LiNi_{1/3}Co_{1/3}Mn_{1/3}O_2$ as the cathode material (Fig. 19a). The cell started working with the initial capacity of 446 mA h g^{-1} and remained at 300 mA h g^{-1} after 50 cycles (Fig. 19b).

The outstanding performance of transition-metal-based HEOs with a rock salt structure compared to conventional transition metal oxides as anode materials has inspired researchers to study and develop other types of HEOs for battery electrodes. Chen *et al.*[221] studied the spinel HEO $(Mg_{0.2}Ti_{0.2}Zn_{0.2}Cu_{0.2}Fe_{0.2})_3O_4$ synthesized by a solid-state reaction as an anode material in a half cell LIB and observed superior Li storage and electrochemical performances. High reversible specific capacity of 504 mA h g^{-1} at a current density of 100 mA g^{-1} after 300 cycles as well as an exceptional 96.2% capacity retention (about 272 mA h g^{-1}) at a high current density of 2000 mA g^{-1} after 800 cycles was achieved (Fig. 19c). The remarkable electrochemical performance and stability of the electrode material are ascribed to the fast reaction kinetics, capacitive behavior and structural stability of the high-entropy spinel oxide.

Yan *et al.*[222] explored a different HEO with a perovskite structure as an anode material for lithium-ion batteries (Fig. 19d). The high-entropy perovskite titanate in the form of $[(Bi,Na)_{0.2}(La,Li)_{0.2}(Ce,K)_{0.2}Ca_{0.2}Sr_{0.2}]TiO_3$ was synthesized by the solid-state method and its performance as an anode for LIBs was explored in a coin cell. An initial discharge capacity of 125.9 mA h g^{-1} and a reversible capacity of 120.4 mA h g^{-1} at 100 mA g^{-1} with no degradation after 300 cycles were obtained (Fig. 19e). The excellent cycling performance of the anode material is again attributed to the entropy-stabilized structure.

6.2 HEO as a cathode material in Li/Na-ion batteries

Most of the reported studies on HEOs are based on multi-cation systems with only oxygen in the anion sites. Therefore, the total stabilizing configurational entropy of the material comes from the cations. Wang *et al.*[223] reported the development of a multi-anionic and multi-cationic system in which both cations and anions contribute to the total S_{config}, which results in a system with higher stabilizing entropy. In this new material, additional halide (F, Cl) and alkali metal ions (Li^+, Na^+) were added to the multi-cationic transition-metal-based HEO (CoCuMgNiZnO) to

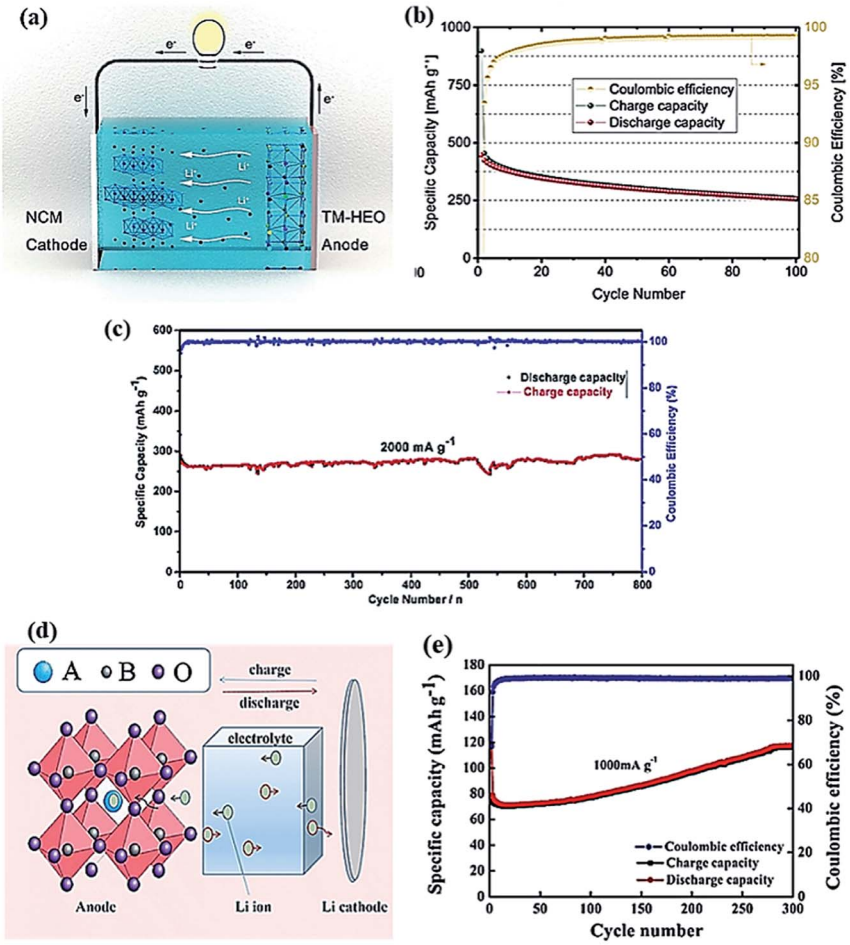

Fig. 19 (a) Schematic of the NCM111||TM-HEO full-cell with the intercalation-based cathode and conversion-based anode; cycling performance and the corresponding coulombic efficacy of (b) the NCM111||TM-HEO full-cell at 120 mA g^{-1} for 100 cycles. Reproduced with permission (ref. 218). Copyright 2019, Elsevier. (c) Cycling performance of the $(Mg_{0.2}Ti_{0.2}Zn_{0.2}Cu_{0.2}Fe_{0.2})_3O_4$ electrode at 2000 mA g^{-1} for 800 cycles. Reproduced with permission (ref. 221). Copyright 2020, Royal Society of Chemistry. (d) Cycling performance of the $[(Bi,Na)_{0.2}(La,Li)_{0.2}(Ce,K)_{0.2}Ca_{0.2}Sr_{0.2}]TiO_3$ electrode at 1000 mA g^{-1} for 300 cycles; and (e) the schematic of the Li-ion half-cell with the perovskite HEO anode. Reproduced with permission (ref. 222). Copyright 2020, Springer Science Business Media.

make a multi-anionic and multi-cationic rock-salt type ionic crystal in the form of Li(HEO)F and Na(HEO)Cl. The synthesized oxyfluoride Li(HEO)F was used as the active cathode material in a half cell Li-ion battery and showed specific capacity retention over 300 cycles. Besides, using these high-entropy materials as cathode materials enables us to achieve a higher and more stable specific capacity compared to conventional LiNiOF materials (Fig. 20a).

Zhao *et al.*[224] applied the concept of high-entropy to design layered oxide cathodes for Na-ion batteries. They used an HEO with nine components as a new O_3-type $NaNi_{0.12}Cu_{0.12}Mg_{0.12}Fe_{0.15}Co_{0.15}Mn_{0.1}Ti_{0.1}Sn_{0.1}Sb_{0.04}O_2$ as Na-ion layered cathode, and it demonstrated long cycling stability after 500 cycles with outstanding capacity retention (83% at 3.0C) (Fig. 20b). Moreover, monitoring the transition between O_3 and P_3 phases during the charge–discharge and Na^+ (de)intercalation process indicated that the phase transition is highly reversible. More notably, more than 60% of the total capacity was stored in the O_3-type region in contrast to other O_3-type Na-ion cathodes. The presence of multiple transition-metal components in the layered HEO that retained the structure during the Na^+ (de) intercalation is presented as the possible mechanism for such a reversible phase transition and long cycling life of the cathode material (Fig. 20c).

6.3 HEO as a chemical anchor of polysulfide in Li–S batteries

An important challenge in Li–S batteries is the capacity fading during cycling due to the shuttle effect of LIPS.[225,226] Many efforts have contributed to finding a suitable catalyst material for the cathode to anchor the LIPS and improve the cycling stability of Li–S batteries. Multicomponent metal oxides such as $ZnCo_2O_4$ and $Ba_{0.5}Sr_{0.5}Co_{0.8}Fe_{0.2}O_{3-\delta}$ are examples of materials proposed for this purpose as they can chemically immobilize the polysulfide in the cathode side.[227–230] Zheng *et al.*[231] reported on applying CoCuMgNiZnO as the cathode catalyst to anchor the LIPS. They observed that due to the synergic contribution of

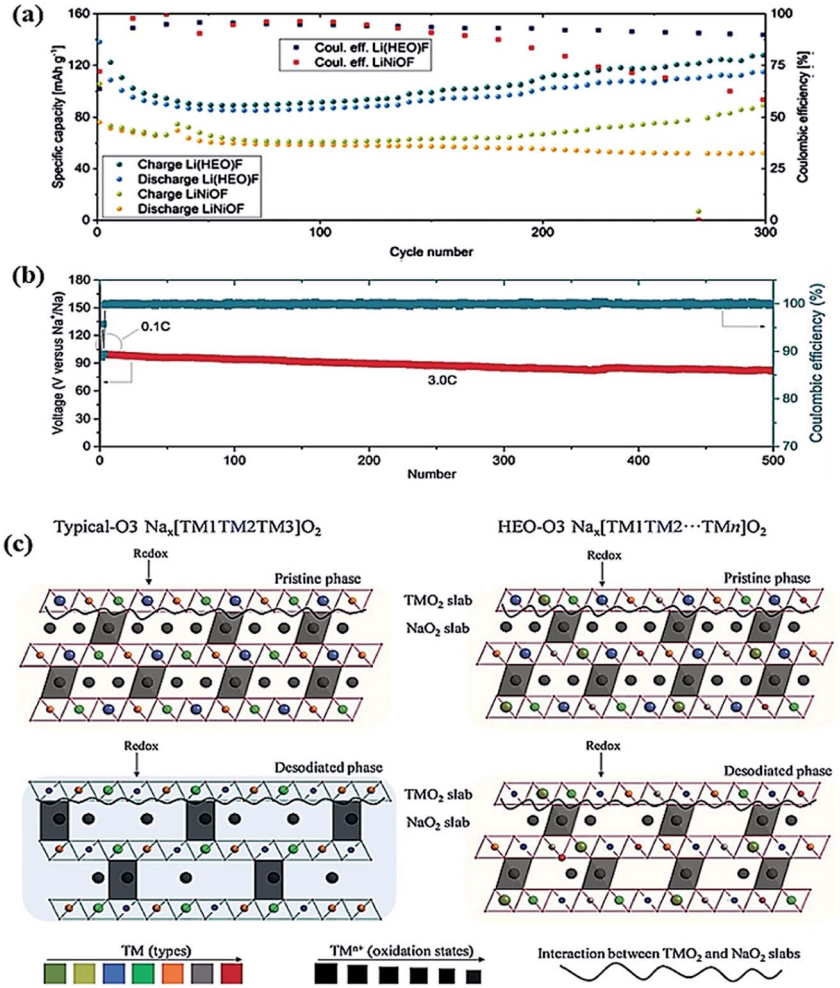

Fig. 20 (a) Capacity retention and coulombic efficiency of Li(HEO)F and LiNiOF at 0.1C. Reproduced with permission (ref. 223). Copyright 2019, Royal Society of Chemistry. (b) Capacity retention and coulombic efficiency of the O_3-type layered HEO at 3.0C; and (c) schematic of the possible mechanism of the Na^+ (de)intercalation process for a typical O_3-type layered cathode (left) with three different transition metal (TM1–3) elements compared to an HEO-O_3 layered cathode (right) with multiple transition metals (TM1–*n*). Reproduced with permission (ref. 224). Copyright 2020, Wiley-VCH.

Li–O and S–Ni binding interactions, HEO can highly restrain the LIPS by chemical absorption. Therefore, they tested the effect of HEO added to the KB carbon cathode in the Li–S cell. The obtained results demonstrated that the cells with the HEMO-1/KB/S cathode and KB/S at 0.1C start working with very similar initial capacities of 1191 mA h g^{-1} and 1131 mA h g^{-1}, respectively (Fig. 18a). However, the cell with the HEO catalyst maintained a high capacity over 200 cycles, while the routine KB/S cell showed very rapid capacity degradation (Fig. 21a). Furthermore, testing at a higher charge/discharge rate of 0.5C revealed the outstanding cycle stability of the HEO/KB/S cell over 600 cycles compared to the fast capacity fading of the KB/S cell after 100 cycles (Fig. 21b).

6.4 HEM as an active electrode material in electrochemical capacitors

Electrochemical capacitors (ECs) or supercapacitors are electrochemical energy storage devices with long cycling life, power density and energy density higher than batteries and dielectric capacitors, respectively. Electrical double-layer capacitors (EDLCs) and pseudo-capacitors are two types of ECs that work based on two different mechanisms. The energy storage in EDLCs happens because of electrostatic interaction in the double-layer between the electrode surface and electrolyte. The electrode material for EDLCs is carbon nanomaterials which provide high power density and long cycling but show limited energy density. On the other hand, faradaic charge transfer at the interface of the pseudocapacitive electrode and electrolyte is the working mechanism in pseudo-capacitors, which provide higher energy density but suffer from poor cycling life.[232] Therefore, much effort has been made to develop new electrode materials for ECs with improved energy density and cycling life.

Lal and Sundara[210] employed the idea of metal oxide embedded in CNTs using HEO NPs instead of single metal oxides. They synthesized an HEO based on Al, Co, Cr, Fe and Ni metal ions by the sol–gel auto-combustion method. The as-

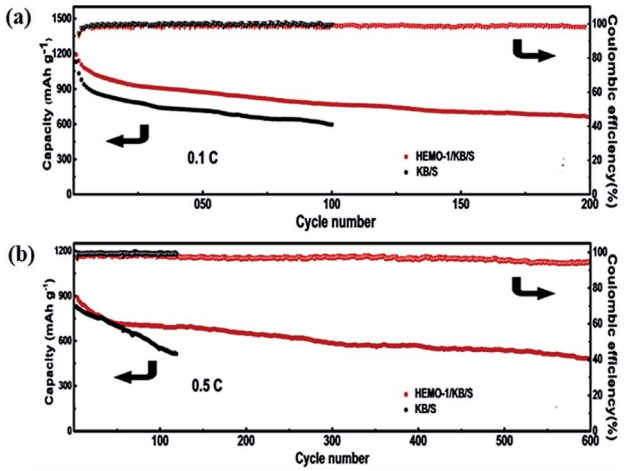

Fig. 21 Capacity retention and coulombic efficiency of HEMO-1 and KB at (a) 0.1C and (b) 0.5C. Reproduced with permission (ref. 231). Copyright 2019, Elsevier.

prepared nanoparticles were used as a catalyst for the CVD growth of CNTs to fabricate the HEO–CNT nanocomposite electrode (Fig. 22a). The electrochemical performance of the nanocomposite electrode was tested in a half cell and full cell with polyvinyl alcohol/H_2SO_4 hydrogel electrolyte. The CV plots of the full cell exhibited a quasi-rectangular shape due to the dual electrical double layer and pseudo-capacitive behavior of the nanocomposite electrode material (Fig. 22b). More importantly, excellent cycling stability of the assembled full cell EC working with the HEO–CNT nanocomposite electrode at the current density of 5 A g^{-1} was achieved over 15 000 cycles with 100% capacitance retention and coulombic efficiency (Fig. 22c).

Jin *et al.*[233] synthesized a nitride HEM (HEMN-1) composed of equimolar V, Cr, Nb, Mo, Zr metals in a cubic crystal structure *via* a soft urea method assisted by mechanochemical synthesis. The single-phase HEMN-1 was evaluated as an electrode for supercapacitors in 1 M KOH electrolyte solution. Cyclic voltammetry (CV) was obtained at different scan rates of 10, 20, 50, 100 and 200 mV s^{-1} (Fig. 22d) and specific capacitance values of

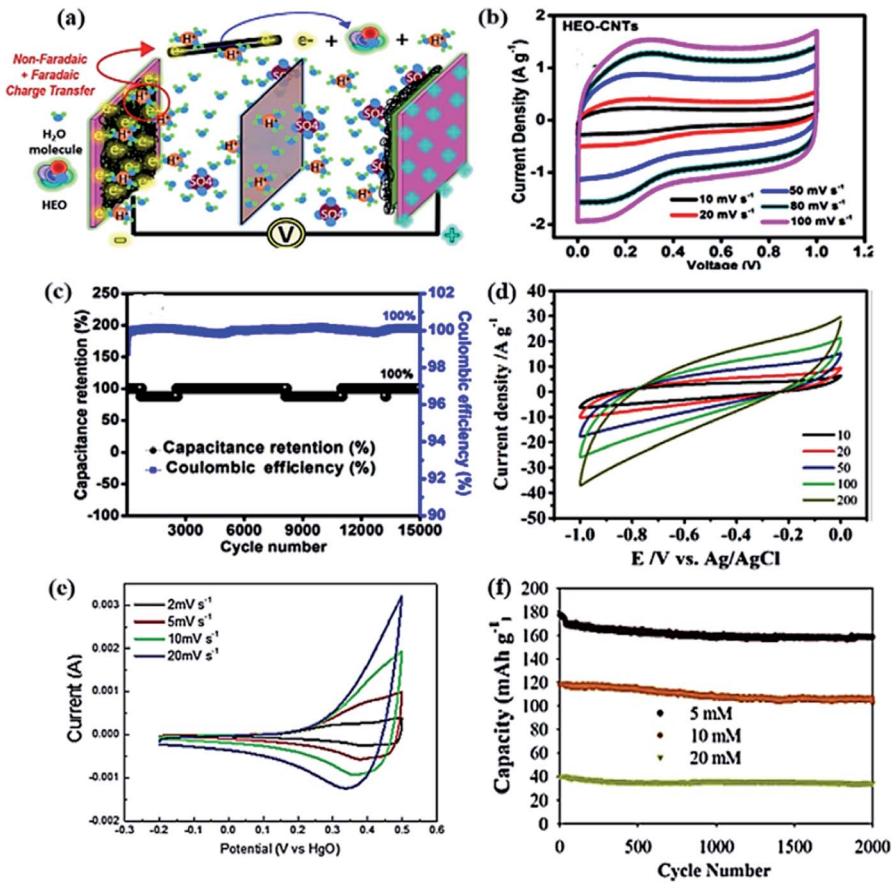

Fig. 22 (a) Schematic of an EC cell with an HEO–CNT nanocomposite electrode; (b) CV curves at different scan rates for the HEO–CNT nanocomposite electrode; and (c) capacitance retention and coulombic efficiency at a current density of 5 A g^{-1} for the HEO–CNT nanocomposite electrode in the fc-EC fabrication with the PVA/H_2SO_4 hydrogel electrolyte. Reproduced with permission (ref. 210). Copyright 2019, American Chemical Society. (d) CV curves at different scan rates for the HEMN-1 electrode in 1 M KOH electrolyte in a three-electrode cell. Reproduced with permission (ref. 233). Copyright 2018, Wiley-VCH. (e) CV curves at different scan rates for the Cr–Fe rich nano-porous HEA electrode in 1 M H_2SO_4 solution. Reproduced with permission (ref. 236). Copyright 2019, Elsevier. (f) Capacity retention of HEA-NPs/ACNF electrodes formed from precursor concentrations of 5, 10 and 20 mM in a cell with 6 M KOH electrolyte solution. Reproduced with permission (ref. 237). Copyright 2020, Elsevier.

230, 175, 113, 78, and 54 F g^{-1} were calculated accordingly. The measured capacitance of the HEMN-1 electrode is higher compared to that of single metal nitride electrodes reported in the literature (46.9 F g^{-1} for VN@C nanowire electrodes at 100 mV s^{-1}).[234,235]

Kong *et al.*[236] applied a single-phase nano-porous HEA as a binder-free electrode for supercapacitors. The single-phase Cr–Fe rich HEM was obtained from the two-phase equimolar AlCoCrFeNi precursor by selective degloving of the Al–Ni rich phase. Also, a thin nanometre layer of metal oxide/hydroxide was formed and detected on the surface of nano-ligaments. As a combined result of having highly conductive ligament metals in the core structure and pseudocapacitive oxide layer on the surface, the HEA electrode showed good performance with a high volumetric capacitance of 700 cm^{-3} (Fig. 22e) and long-term cycling stability of over 3000 cycles.

Xu *et al.*[237] recently reported the electrochemical performance of HEA NPs and carbon nanofiber (CNF) composite as a new supercapacitor electrode. In their study, by using a metal chloride precursor solution with different concentrations of 5, 10 and 20 mM, quinary FeNiCoMnMg HEA NPs are uniformly synthesized on aligned carbon nanofibers (ACNFs) through a carbothermal shock method. The electrochemical performances of the HEA NP/ACNF electrodes were examined in a cell with 6 M KOH electrolyte solution. The composite electrode prepared with a 5 mM precursor solution exhibited better performance with a high capacitance of 203 F g^{-1} and a specific energy density of 21.7 W h kg^{-1}. Moreover, the electrode showed 89.2% capacity retention up to 2000 cycles, which makes it a promising candidate for practical purposes (Fig. 22f).

7. High-entropy materials in hydrogen storage application

Hydrogen is known as a potential renewable source of energy and green alternative for fossil fuels due to its abundance and various production and storage technologies. One of the suitable and safe hydrogen storage methods is using metal hydrides as an on-board hydrogen tank.[238–240] The most important properties of metal hydrides for use in hydrogen storage applications are high hydrogen storage capacity (>2 wt% at room T), fast kinetics (high absorption–desorption reaction rate), ease of activation, reversible and stable hydrogen absorption–desorption over cycling as well as the low cost of the metals and alloys.[238–240] Hydrogen atoms dissolved in the metal matrix occupy the octahedral and tetrahedral interstitial sites of the crystal lattice.[241–243] This fact indicates that the maximum atomic ratio of absorbed hydrogens to metals or their alloys ($(H/M)_{max}$) is related to the number of interstitial sites in the metallic host lattice.[244]

Most of the metallic elements can absorb hydrogen and form a hydride. However, the thermodynamic conditions under which hydrogenation and dehydrogenation of metals occur differ widely for different elements. This can be explained by the Pressure–Composition–Temperature (PCT) diagram of each element and its related Van't Hoff equation $\ln P = (\Delta H/RT) - (\Delta S/R)$, where ΔH, $\Delta S$and T are the enthalpy, entropy and absolute temperature of the hydration reaction, respectively, and R is the gas constant.[245] For all hydrides, ΔH and ΔS are negative during hydrogen absorption and the reaction is exothermic while they are both positive for the endothermic hydrogen desorption reaction. The change in entropy during hydrogen absorption and desorption reactions is mainly the change in the entropy of hydrogen from the gas phase to the metal solution phase and *vice versa*.[238] Therefore, from the Van't Hoff equation, for each metal at a constant given temperature, the constant pressure of hydrogenation or dehydrogenation (Plateau P) depends on the value of hydride reaction enthalpy and strength of the metal–hydrogen bonds.[238,245]

For practical applications, it is desirable that desorption of hydrogen occurs under near-ambient conditions, *i.e.*, temperature and pressure range of 1–100 °C and 1–10 atm, respectively. Based on the Van't Hoff desorption lines for elemental hydrides (Fig. 23),[245] only V satisfies this thermodynamic condition for hydrogen desorption. The elemental hydrides on the down-left side of the diagram with very low pressure and high-temperature ranges of hydrogen desorption are called strong hydride forms. On the other hand, the elemental hydrides on the up-right with very high hydrogen desorption pressure are known as weak hydride forms. Therefore, the main reason for using metal alloy hydrides instead of a pure metal hydride is to combine the strong (A, *e.g.*, La, Ti and Zr) and weak (B, *e.g.*, Ni, Mn and Co) hydride forming elements and make an alloy with intermediate thermodynamic affinities for hydrogen.

Over the years, various types and combinations of intermetallic compounds and alloys composed of weak and robust hydride forming elements with different structures for hydrogen storage have been studied. The most common types of these alloys are AB_5 intermetallic compounds, AB_2 intermetallic compounds and solid solution alloys.[245] The effects of element selection and their composition in alloys, phases and crystal structures of alloys, as well as the synthesis methods of alloys and heat treatment on hydrogen capacity (PCT diagram),

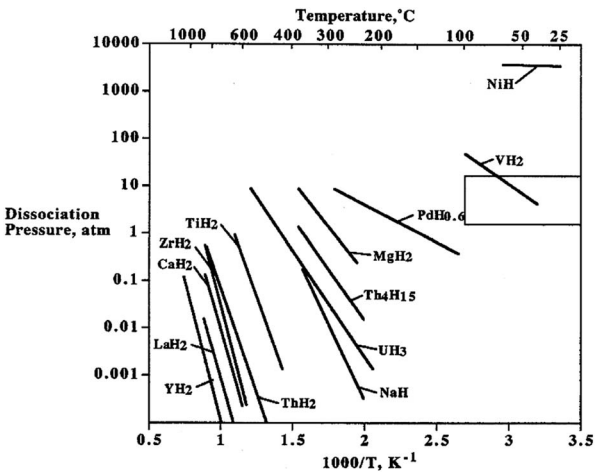

Fig. 23 Van't Hoff lines of hydrogen desorption for metal hydrides. Reproduced with permission (ref. 245). Copyright 1999, Elsevier.

equilibrium plateau pressure, and hydrogen absorption and desorption kinetics, are mostly investigated.[246–259] Intermetallic compounds have a low hydrogen storage capacity limited to about 1.4 wt%, which is not sufficient to meet the requirements for many hydrogen storage applications (capacity > 2 wt%). The other problem related to intermetallic phases is their low cycling stability. However, alloys with intermetallic phases, especially Laves phase structures, show fast kinetics for hydrogen absorption–desorption in addition to an easy activation step for the processes.[239,246,247,252–254]

BCC solid solutions are known to have very high hydrogen storage capacity (H/M > 2 wt%), but they suffer from poor kinetic properties and difficulty of activation. BCC metals and their alloys usually undergo a structural transition during the hydrogenation process and have an FCC structure in their hydride forms.[239] Among all BCC metals, only vanadium and rubidium hydrides can desorb the stored hydrogen at atmospheric pressure and room temperature.[255] Hence many V-based solid solutions are studied, focusing on the impact of different added elements and their compositions on the hydrogen storage properties of the system.[248–251,256–259]

The multiphase alloys with a mixture of BCC solid solution and intermetallic Laves phase are found to have the intermediate properties of high hydrogen storage and fast kinetics. The concept of the Laves phase-related BCC structure was introduced first by Akiba and Iba.[239] These multi-phase alloys showed high hydrogen storage in the BCC phase and fast kinetics due to intermetallic Laves phases.[257,259–261] Kao *et al.*[262] reported the hydrogen storage properties of $CoFeMnTi_xV_yZr_z$ HEA with a single C_{14} Laves phase structure. They also studied the effect of chemical composition and the affinity between alloy components and hydrogen on the maximum hydrogen capacity. It was found that the $CoFeMnTi_2VZr$ alloy exhibited maximum hydrogen capacity up to 1.8 wt% at room temperature. Kunce *et al.*[263–265] synthesized ZrTiVCrFeNi, TiZrNbMoV and LaNiFeVMn[264] alloys with laser engineered net shaping (LENS) method and studied the effect of fabrication parameters and elemental compositions on alloy phases and hydrogen absorption–desorption properties associated with them. Based on their results, ZrTiVCrFeNi, with a dominant C_{14} Laves phase, showed a maximum hydrogen capacity of 1.8 wt% and 1.56 wt% at 100 bar and 50 °C for as-synthesized and annealed samples, respectively.[265] TiZrNbMoV samples synthesized with different laser powers led to different phase compositions and hydrogen storage capacities. Chen *et al.*[266] showed that $Cr_uFe_vMn_wTi_xV_yZr_z$ HEAs have a stable C_{14} Laves structure during the absorption–desorption cycle, which is highly beneficial for having a long-life alloy for hydrogen storage application. They also investigated the effect of elemental composition on the maximum hydrogen capacity and kinetics of the hydrogenation reaction while the phase structure of the alloys remained unchanged. It was concluded that $(H/M)_{max}$ is mainly dependent on the hydride formation enthalpy of alloys which can be optimized by the compositions of hydrogen absorbing (Zr, Ti) and hydrogen desorbing (Fe, Mn, Cr) elements. Similarly, the rate of hydrogenation reaction increases with Fe, Mn and Cr concentrations while it decreases with Zr concentration.

Sahlberg *et al.*[267] reported the hydrogen storage properties of an equimolar single solid solution TiVZrNbHf (synthesized by arc-melting) with a BCC structure. They measured an $(H/M)_{max}$ of 2.5 equivalent to 2.7 wt% for a fully hydrogenated HEA hydride at 300 °C and 53 bar with a plateau pressure of 0.1 bar and a reversible H/M ratio range of 0.3–1.7 (~1.5 wt%). The measured H/M ratio of 2.5 in the hydrogenated HEA (HEA-$H_{2.5}$) is higher than the maximum (H/M) ratio of 2 in fully hydrogenated binary hydrides of components (MH_2). They proposed a new mechanism of hydrogenation and the associated phase transition for HEAs, which makes it different from normal BCC metals and other alloys. A normal BCC metal or alloy undergoes a phase transition during hydrogenation from the initial BCC structure (H/M = 0) to a distorted BCC (BCT) while getting partially hydrogenated (H/M < 1) and finally to FCC in their fully hydrogenated form (H/M = 2) when hydrogen atoms occupy the tetrahedral sites (BCC route in Fig. 24a). However, reaching an H/M ratio of 2.5 with the HEA indicates that in addition to all tetrahedral sites, hydrogen atoms could occupy about 50% of the octahedral sites. On the other hand, in the phase transition during hydride formation of light rare-earth (RE) metals (La, Ce) with H/M > 2, first the initial double hexagonal close-packed (dHCP) structure changes to FCC (H/M < 3) and upon more hydrogenation, a distorted tetragonal FCC (BTC) structure is formed (RE route in Fig. 23a). From the observed BTC structure of hydrogenated HEAs with H/M > 2, a unique hydrogenation mechanism, which is a combination of two BCC and RE routes, is introduced as the HEA route (Fig. 24a). It is suggested that the high lattice strain build-up due to atomic size difference in HEA is the main reason for providing more available interstitial sites for hydrogen occupancy and formation of the final BCT structure in hydride HEAs. The proposed mechanism was investigated more by neutron diffraction for determination of the positions of hydrogen atoms in the HEA hydride in their next study.[268] It was observed that at high temperature and pressure (500 °C and 50 bar) hydrogen fills both tetrahedral and octahedral sites of the tetragonal structure (Fig. 24b). The PCT diagram measurements showed that the hydrogen adsorption–desorption is reversible at 500 °C (Fig. 24c). The reactions are kinetically slow due to the low activation energy of the alloy since the reaction rate increases slightly (about 20%) after activation over cycling (Fig. 24c).

Different observations and phase transformations for the TiZrNbHfTa HEA with a BCC structure were reported by the same group when they substituted V with a larger element Ta to examine the effect of change in lattice size and distortion on the hydrogen sorption properties of HEAs.[269] They synthesized an alloy that undergoes the BCC route phase transition from BCC to BCT during hydrogenation and to FCC in the full hydride form. Moreover, two plateaus at low and high pressure were observed in pressure–composition isotherm curves, which is again like the hydrogenation behavior of ordinary BCC metals. The substitution of V by Ta leads to a decrease in the δ parameter from 6.8% to 4.6%, and consequently, a decrease in the associated lattice distortion. From the different observations for the mentioned HEAs, the authors suggested that higher δ could be responsible for single-phase transition from BCC to BCT and

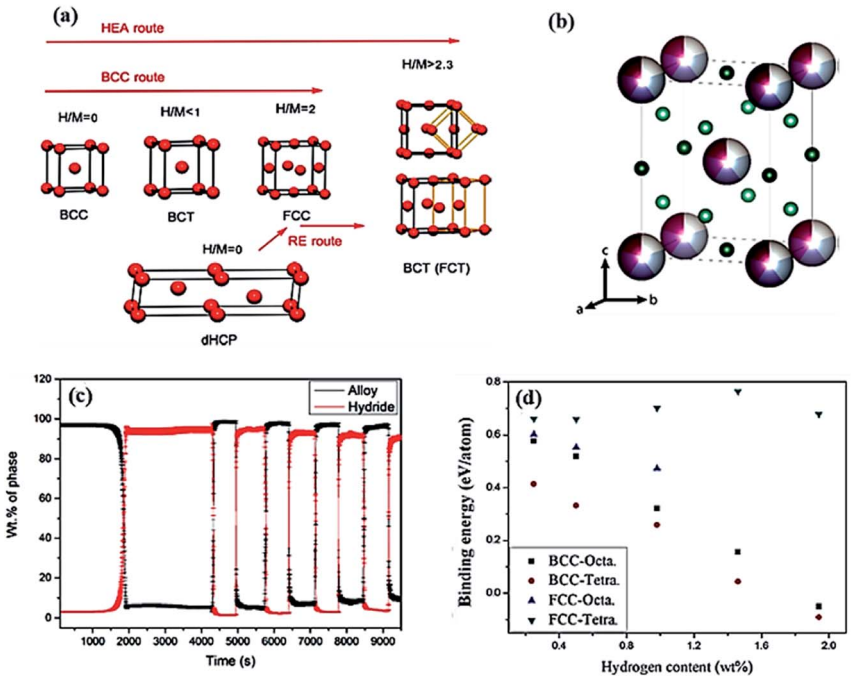

Fig. 24 (a) Different routes for hydrogen adsorption in metals. Reproduced with permission (ref. 267). Copyright 2016, Springer Nature. (b) Structural model for the metal deuteride; and (c) phase contents for the alloy and hydride phase at 500 °C. Reproduced with permission (ref. 268). Copyright 2018, American Chemical Society. (d) Variation of the binding energy for the BCC and FCC hydrogenated TiZrHfMoNb with the H content. Octa.: octahedral occupation for H; Tetra.: tetrahedral occupation for H (ref. 272).

hydrogenation occupation in tetrahedral sites. HEAs with smaller lattice distortion act similar to normal BCC type metals.

In the following studies, Nygard *et al.*[270] investigated the accuracy of the hypothesis wherein the high atomic H/M ratio capacity of HEAs is related to the value of its lattice strain. They measured the hydrogen absorption–desorption and BCC/FCC lattice parameters of the synthesized $TiVZr_zNbTa_{1-z}$ alloys and their hydrides. The lattice parameter (a) and local lattice strain (δ) increase with the composition of Zr as the largest atom in the alloy. The result showed that all alloys (with BCC structures), regardless of their different lattice strains, have FCC structures in their hydride form and H/M ratio $\sim$ 2. Therefore, no relationship between the hydrogen capacity of HEAs and higher lattice strain as well as Zr/M ratio was observed. However, increasing Zr composition in alloys stabilizes the hydrides. In another work,[271] they studied the effect of VEC of the alloys on their hydride crystal structures and their corresponding hydrogen capacities. They showed that the BCC alloys with VEC < 4.75 form hydrides with a single FCC structure and others with VEC > 4.75 form hydrides with multiple FCC/BCC phases and the ratio of their FCC phase decreases with VEC. However, the first result reported for TiVZrNbHf was not observed in their findings.

Shen *et al.*[272] reported a maximum hydrogen capacity of 1.18 wt% and a reversible BCC to FCC phase transformation during hydrogenation at room temperature and atmospheric pressure for the TiZrHfMoNb. The stabilities of the BCC and FCC structures of TiZrHfMoNb and its hydride form were calculated by the DFT method. It was confirmed that the BCC structure is preferable for pure alloys due to 0.25 eV per atom lower energy than the FCC structure. For the hydrogenated alloy, however, the FCC structure is always favorable because of the higher binding energies. Therefore, hydrogen occupies tetrahedral sites in the FCC phase and octahedral sites in the BCC phase (Fig. 24d). In the same group, Hu *et al.*[273] did a DFT study on the hydrogen storage properties of TiZrHfScMo HEAs with a BCC structure. The calculated result showed that the maximum hydrogen capacity of 2.14 wt% can be obtained and elements in the alloy play different roles based on their covalent bonding energies with hydrogen atoms during hydrogenation. Zepon *et al.*[274] synthesized non-equimolar $MgZrTiFe_{0.5}Co_{0.5}Ni_{0.5}$ HEM (A_2B chemical composition) and its $(MgZrTiFe_{0.5}Co_{0.5}Ni_{0.5})H_x$ hydride form with BCC and FCC structures, respectively. A maximum hydrogen capacity of 1.2 wt% equivalents to a low atomic ratio of H/M = 0.7 was observed during absorption at 350 °C, which indicates that there exist kinetic and thermodynamic limitations preventing further hydrogenation to form the dihydride of the alloy.

8. Prospective applications

HEMs have demonstrated many appealing features and capabilities which have significantly boosted their potential applications in catalysis, energy conversion and storage. While further studies are ongoing to explore their durability and performance under severe conditions, we briefly highlight other possible energy-related applications with the opportunity of employing HEMs (Fig. 25).

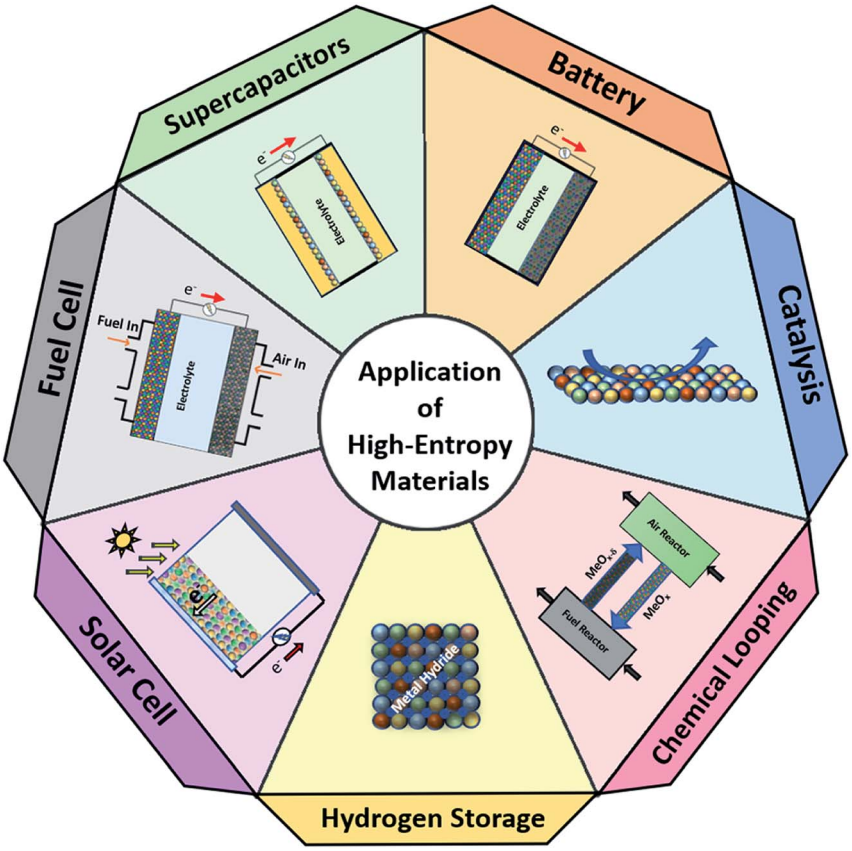

Fig. 25 Energy-related applications of high-entropy materials.

8.1 Catalysis

Until now, there are a limited number of studies on the catalytic performance of HEMs (Table 1). However, their exceptional activities and favorable performances are inspiring to investigate them in many other catalytic applications. It was observed in different studies that HEAs have higher catalytic activity and longer stability compared to the single-atom and binary/ternary alloys. The superior catalytic performance of HEAs is attributed to their entropy-stabilized structure, synergistic effect and continuum active area provided by their highly disordered distribution of atoms. Therefore, it can be expected that HEMs are potential alternative catalysts for many other catalytic reactions relying on precise noble metals as their state-of-art catalysts. The concept can be applied to many Pt group unary, binary, or ternary alloy catalysts by adding more elements to improve their catalytic performances due to the synergistic effect and optimization of catalyst surface adsorption energies. More importantly, by adding non-noble metals like active transition metals to the system, the cost of the catalyst and, accordingly, the cost of the process reduce significantly while the performance is expected to be enhanced. However, the most desirable perspective is to employ HEAs composed of non-noble metals as considerably cheaper and more abundant materials with comparable or even better activities and stabilities. Therefore, these materials can be one of the most attractive solutions for cost and sustainability problems related to green energy processes relying on precious metal catalysts.

HEMs, especially HEOs, are a suitable choice of material for any application that requires high temperature stable active catalysts due to the high-temperature dependency of entropic contribution in minimizing Gibbs free energy. In addition, HEOs are suitable supports for dispersion of single noble metal atoms on their highly active sites. This means they can play a double-effective role in improving the catalyst activity and reducing the cost of the materials by using less amount of precious metals. HEMs are also appealing choices for any application in harsh acidic and basic environments, due to their high corrosion resistance.[275,276]

There are many binary and ternary transition metal alloys known to be efficient catalysts for different applications. However, they usually suffer from a miscibility gap and limited compositional flexibility.[76] In this respect, adding two or three more suitable elements to these combinations and employing them in the form of HEA catalysts for the same reaction resolves not only the miscibility problem but also improves their activity and performance stability.

We also believe that other aspects of HEMs in catalysis applications need to be investigated in future research work. (1) The intrinsic properties of HEAs in published studies are mostly tested by comparing the five-elemental alloys with four and less than four elemental alloys. However, it is still necessary to

investigate the effect of the number of elements and compositions in HEMs with a higher number of elements to clearly examine the impact of configurational entropy on their properties and performances. (2) The inherent capability and high performance of HEMs are attributed to the known four effects of these materials (Fig. 1). However, further studies are needed to fully understand the mechanisms by which catalytic HEMs work.

8.2 Batteries

A few types of HEOs are evaluated as electrode materials for Li/Na ion batteries due to their high alkali ion conductivity and structural stability over cycling (Table 2). However, to broaden the observations and findings of their advanced performances, various oxide and non-oxide HEMs with other compositions and crystal structures need to be examined as electrode materials in different metal-ion batteries. HEAs can also be designed for high capacity electrodes in Li/Na-ion batteries, with the ability to control their electrochemical performance with vast compositional tuning. Moreover, the high electrocatalytic activity of HEAs toward the OER and ORR makes them a promising candidate for air electrodes in Li– and Na–air batteries.[277]

Besides the application as electrode materials, due to the superior ionic conductivity of HEOs doped with alkali metal cations[212] ($\sim 10^{-3}$ S cm^{-1}), they can be considered as solid-state electrolytes for alkali ion and alkali sulfur batteries. Similarly, sulfide HEMs as a solid electrolyte for Li/Na-ion batteries is worth studying and comparing with the well-known sulfide solid electrolytes (LISICON and NASICON).[278]

Although high-entropy polymers are still in the early stages of development, further studies can be conducted to explore new functional solid polymer electrolytes with enhanced ionic conductivity and cycling stability for Li/Na-ion batteries.[32,279] Addition of ionic conductive nanoparticles and nanosheets to the polymeric matrix is a known effective approach to increase the low ionic conductivity and mechanical stability of composite polymer electrolytes and eventually improve the performance of solid-electrolyte Li-ion batteries.[280,281] Many different types of metal oxides and ceramic nanoparticles or nano-flakes, as well as MOFs, have been used in the fabrication of polymer composite electrolytes and studied for their performance as solid electrolytes.[280–284] Due to the possible advantages of the high-entropy form of these materials (high-entropy oxides, nitrides, phosphides, and MOFs), many new high-

Table 1 List of all high-entropy materials used as catalysts in different catalysis processes

High-entropy material catalyst	Catalysis reaction	Synthesis method	Ref.
$Pt_{50}Fe_{11}Co_{10}Ni_{11}Cu_{10}Ag_8$ NPs	MOR	Radio frequency sputter deposition method	103
PdNiCoCuFe NTAs	MOR	Template assisted electrodeposition method	122
np-PtRuCuOsIr	MOR ORR	Chemical dealloying of the AlCuPtRuOsIr precursor	116
np-AlNiCuPtPdAu	ORR, HER, CO oxidation	Chemical dealloying of an Al-rich precursor	139
np-AlNiCoFeX (X = Cu, Cr, Mn, Mo, Nb, Zr, V)	OER	Chemical dealloying of an Al-rich precursor	160
CuAgAuPdPt NPs	FAOR, MOR	Arc melting + cryo-milling	88
RuRhPdOsIrPt NPs	EOR	Co-reduction of metal ions with triethylene glycol	127
PtAuPdRhRu NPs	HER	Co-reduction of metal ions with ethylene glycol	157
IrPdPtRhRu NPs	HER	Co-reduction of metal ions with triethylene glycol	114
CrMnFeCoNi NPs	ORR	Co-sputtering into an ionic liquid	138
$Ni_{20}Fe_{20}Mo_{10}Co_{35}Cr_{15}$	HER	Arc melting method	156
MnFeCoNi nanosheets	OER	Mechanical alloying	114
PtPdRhNi/CNF NPs PtPdFeCoNi/CNF NPs	ORR	Carbothermal shock method	140
FeCoPdIrPt@GO NPs	HER	Fast-moving bed pyrolysis method	158
CoMoFeNiCu ($HEACo_{25}Mo_{45}$)	Ammonia decomposition	Carbothermal shock method	76
$Ru_{0.44}Rh_{0.30}Co_{0.12}Ni_{0.14}$	Ammonia decomposition	Electrical Joule heating method	101
IrPdPtRhRu	ORR	DFT analysis	141
CoCuGaNiZn	CO_2 reduction	DFT analysis	189
AgAuCuPdPt	CO_2 reduction	Melting and cryo-milling	191
AlCoCrFeNi AlCoCrTiZn CoCrFeMnNi	Azo dye degradation	Ball milling	208
AlCrFeMnM (M = Mg, Ti, Ni)	Azo dye degradation	Ball milling	209
$(CoCuFeMnNi)_3O_4$ NPs/MWCNTs	OER	Solvothermal method	16
Pt doped (NiMgCuZnCo)O	CO oxidation, CO_2 reduction	Ball milling	174
Ru doped BaSrBi $(ZrHfTiFe)O_3$	CO oxidation	Sono-chemical method	175
Pd doped $(CeZrHfTiLa)O_x$	CO oxidation	Ball milling in a fumed silica template	177
Ni, Fe, Co, Cr, and Al-based oxide NPs	CNT growth	Sol–gel auto-combustion method	210
$K_{1-x}Na_x(MgMnFeCoNi)F_3$	OER	Hydrothermal method combined with mechanochemistry	27
CoCrFeMnNi–P	HER, OER	Eutectic solvent method	26
NiCdCoCuZn-ZIF	CO_2 conversion to carbonate	Mechanochemistry method	145
MnFeCoNiCu-MOF	OER	Room temperature wet chemistry	30

Table 2 List of all high-entropy oxides tested as battery electrodes

HEO battery electrode	Crystal structure	Active electrode	Performance	Ref.
$(Co_{0.2}Cu_{0.2}Mg_{0.2}Ni_{0.2}Zn_{0.2})O$	Rock-salt oxide nano to micro size	Anode half-cell test	Initial discharge specific capacity of 980 mA h g^{-1} Reversible capacity of 590 mA h g^{-1} at 0.2 A g^{-1} after 500 cycles	217
$(Co_{0.2}Cu_{0.2}Mg_{0.2}Ni_{0.2}Zn_{0.2})O$	Rock-salt oxide nanocrystalline	Anode half-cell test	Initial discharge specific capacity of 1585 mA h g^{-1} Reversible capacity of 920 mA h g^{-1} at 0.1 A g^{-1} after 300 cycles	219
$(Co_{0.2}Cu_{0.2}Mg_{0.2}Ni_{0.2}Zn_{0.2})O$	Rock-salt oxide nanocrystalline	Anode full cell with $LiNi_{1/3}Co_{1/3}Mn_{1/3}O_2$ cathode	Initial discharge specific capacity of 446 mA h g^{-1} Reversible capacity of 256 mA h g^{-1} at 0.12 A g^{-1} after 100 cycles	218
$(Mg_{0.2}Ti_{0.2}Zn_{0.2}Cu_{0.2}Fe_{0.2})_3O_4$	Spinel oxide nanocrystalline	Anode half-cell	Initial discharge specific capacity of 1261 mA h g^{-1} Reversible capacity of 504 mA h g^{-1} at 0.1A g^{-1} after 300 cycles	221
$[(Bi,Na)_{0.2}(La,Li)_{0.2}(Ce,K)_{0.2}Ca_{0.2}Sr_{0.2}]TiO_3$	Perovskite oxide micro size	Anode half-cell	Initial discharge specific capacity of 125.9 mA h g^{-1} Reversible capacity of 120 mA h g^{-1} at 1 A g^{-1} after 300 cycles	222
$Li_x(Co_{0.2}Cu_{0.2}Mg_{0.2}Ni_{0.2}Zn_{0.2})OF_x$	Rock-salt oxide nanocrystalline	Cathode half-cell	90% of capacity retention at 0.1C after 300	223
$NaNi_{0.12}Cu_{0.12}Mg_{0.12}Fe_{0.15}Co_{0.15}Mn_{0.1}Ti_{0.1}Sn_{0.1}Sb_{0.04}O_2$	O_3-Type layered oxide micro size	Cathode half-cell	83% of capacity retention at 3C after 500 cycles	224

entropy polymer-composite materials have the potential to be designed and studied in the future.

8.3 Electrochemical capacitors (ECs)

Pseudo-capacitors are one type of supercapacitors that work based on faradaic charge transfer mechanisms from redox reactions at the interface of the electrode (metal oxides)–electrolyte with high energy density but they suffer from poor cycling life.[232] HEOs composed of TM-metal oxides can be designed with optimal pseudo-capacitance properties to be used as electrode materials in capacitors. Other HEMs like carbide HEMs and sulfide HEMs could also be suitable electrode materials for EC devices since they have been previously used in their binary and ternary forms. The entropy-stabilization feature of these materials is expected to enhance the cycling stability of pseudo-capacitors, which is their main disadvantage. Moreover, the colossal dielectric constant of rock-salt HEO doped with aliovalent cations could make them a suitable candidate as a solid electrolyte material in capacitors.[85] More investigations on other HEOs with different compositions are needed for a better understanding of this behavior. On the other hand, embedding metal NPs in polymers is known to show significant enhancement of the dielectric constant.[285,286] In this regard, HEM NPs could be evaluated in a composite membrane as another novel solid electrolyte for capacitors.

8.4 Solar cells

The sun is obviously one of the cleanest and most abundant sources of renewable energy. However, solar cells are still too expensive compared to other energy sources considering material cost and efficiency. Low-cost, abundant, and highly effective materials for different types of solar cells and accordingly, research efforts in this area are still facing challenges in finding new efficient advanced materials. High-entropy materials can provide further advantages in several parts of solar cells by improving the efficiency and reducing the cost. Developing suitable HEAs with vast compositional tailoring enables the possibility of fine-tuning the optical properties and bandgap reduction of semiconductor materials for thin-film solar cells.

Wide bandgap metal oxides like TiO_2 and ZnO are imperative materials in dye-sensitized solar cells (DSSCs) and perovskite solar cells (PSCs). Modifying their bandgap energy and optical properties *via* partial doping with other metal oxides is one of the adequate directions to improve the performance of cells. Obtaining a single-phase crystal structure is difficult in the case of ternary oxides, which limits the compositional tuning and requires a very high synthesis temperature. These issues can be resolved by the concept of entropy-stabilization in single-phase HEOs and their vast compositional space for a large number of elements.

The high-entropy concept is expanding to various types of materials. In this regard, high-entropy halides could be another perspective material with superior properties compared to their binary and ternary forms. Designing and synthesizing single-phase crystalline high-entropy halide perovskites (ABX_3) as quantum dot materials for light-sensitized perovskite solar cells can have beneficial impacts on the performance of the cell.

8.5 Fuel cells

HEMs have shown highly promising activity as anode and cathode electrocatalyst materials for fuel cells. Still, many

compositional spaces need to be explored for further performance optimization. Fluorite HEOs, composed of equimolar cerium and other rare earth elements, show higher oxygen vacancies compared to binary oxides and doped cerium oxides with a limited amount of added elements.[11,12,287] Due to this high oxygen conductivity property and strong stability at high temperatures, they could be promising solid electrolyte materials for solid oxide fuels. These features, as well as the high chemical and mechanical stability comparable with YSZ, also make them an attractive choice of material for porous ceramic supports in molten carbonate fuel cells and ceramic-molten carbonate dual-phase membranes.[287]

8.6 Chemical looping systems

Oxygen stored in the lattice of metal oxides is used for methane combustion in chemical looping systems as an inherent CO_2 separation method or in chemical looping reforming for H_2 production.[288] In these systems, metal oxides as oxygen carriers circulate between two fuel and air reactors, where they are reduced by methane and re-oxidized by air, respectively.[288] The selection of suitable oxygen carriers with high oxygen capacity and decent mechanical stability is a critical factor for the efficiency of these systems.[289] CeO_2-based oxygen carriers have high oxygen capacity due to oxygen vacancies in the lattice. Doping with other metal oxides like Zr, Fe and Cu can modify the performance of oxygen carriers in oxygen uptake and realize the conversion and selectivity of the reaction as well.[290–293] However, the percentage of dopants is kept to a limited amount not to affect the fluorite structure of CeO_2. A fluorite HEO composed of near equimolar Ce and other metal cations in a single cubic crystalline structure with high oxygen vacancy and excellent mechanical stability is expected to be an ideal choice of material for these applications. They can open a new perspective in oxygen carrier modification, and future studies can be directed to compositional space for optimizing their essential properties.

8.7 Hydrogen storage

HEAs have shown remarkable hydrogen storage capacity and reversible phase transformation upon hydrogenation/dehydrogenation cycling. However, the details regarding the associated properties and factors affecting their hydrogen storage performance are not clear yet. Therefore, more comprehensive studies on potential HEMs are needed to clarify their specific advantages as hydrogen storage materials. Also, computational studies on a large number of HEAs with various numbers and combinations of elements and their vast compositional tuning can explore new materials with enhanced hydrogen storage capabilities.

9. Summary

The concept of high-entropy is now covering a wide range of organic and inorganic materials and can be effectively used to design and develop vast types of new materials with desired properties. Entropy, as the level of randomness, can be manipulated in terms of both compositional complexity and structural disorder to explore the mechanical and functional properties of materials for various applications.

HEMs, including metallic alloys as well as oxides, diborides, carbides, and sulfides, are emerging new materials with promising properties and high-performance durability due to their entropy-driven stabilization. High ΔS_{mix} associated with mixing five or more near-equimolar metal elements or ions favors the formation of a single-phase solid solution thermodynamically. Subsequent studies have shown that other thermodynamic and structural parameters as well as kinetic factors are also important in the formation of a single-phase crystalline solid solution. Beyond the well-known mechanical properties, HEMs have received attention for the outstanding functional properties attributed to their entropic phase stabilization, lattice distortion, sluggish diffusion, and cocktail effects.

As catalyst materials or as catalyst supports, HEMs show outstanding properties. HEMs have been investigated as cathode/anode electrocatalysts for reactions like the MOR, FAOR, EOR, ORR, HER and OER, as well as catalysts for ammonia decomposition, methane burning, CO oxidation, CO_2 reduction and azo dye degradation. Noble metal-based and TM-based HEMs demonstrated higher activity and stability than many commercial Pt group catalysts. The enhanced performance of HEMs is described by the synergistic effect of multiple elements, higher atomic coordination and active surfaces, optimized surface adsorption energies and entropy-stabilization of their structure. HEOs also revealed outstanding properties as catalyst themselves and stable supports for homogeneous dispersion of active metal single atoms. These studies manifest that HEMs are promising catalyst materials with high activity, excellent stability and low-cost for several applications.

In the energy storage field, HEMs are shown to be promising as hydrogen storage materials, battery electrodes, and capacitors. HEAs with a single-phase BCC structure are reported to be high capacity metallic alloys for hydrogen storage. Due to their interesting electrochemical properties such as colossal dielectric constant and high Li conductivity, HEOs are studied as electrode materials for Li-ion batteries and they show high capacity and long cycling life. Different types of HEM NPs demonstrated good performance in electrochemical capacitor systems. The outstanding physical and chemical properties of HEMs and their capability of being vastly tuned with respect to composition make them a promising choice of material for various energy conversion and storage applications.

Organic high-entropy materials such as high-entropy polymers, meso-entropy 2D carbon and phosphorus materials are other potential materials to be explored for desired properties in different energy-related applications. Organic high-entropy materials such as high-entropy polymers, meso-entropy 2D carbon and phosphorus materials are other potential materials to be explored for desired properties in different energy-related applications.

Conflicts of interest

There are no conflicts to declare.

Acknowledgements

The authors acknowledge the financial support from the National Science Foundation (NSF) Award DMR-1809439.

References

1 B. Cantor, I. T. H. Chang, P. Knight and A. J. B. Vincent, Microstructural Development in Equiatomic Multicomponent Alloys, *Mater. Sci. Eng. A*, 2004, **375–377**(1–2 Spec. Iss.), 213–218, DOI: 10.1016/j.msea.2003.10.257.

2 J. W. Yeh, S. K. Chen, S. J. Lin, J. Y. Gan, T. S. Chin, T. T. Shun, C. H. Tsau and S. Y. Chang, Nanostructured High-Entropy Alloys with Multiple Principal Elements: Novel Alloy Design Concepts and Outcomes, *Adv. Eng. Mater.*, 2004, **6**(5), 299–303, DOI: 10.1002/adem.200300567, 274.

3 Y. Zhang, T. T. Zuo, Z. Tang, M. C. Gao, K. A. Dahmen, P. K. Liaw and Z. P. Lu, Microstructures and Properties of High-Entropy Alloys, *Prog. Mater. Sci.*, 2014, **61**(September 2013), 1–93, DOI: 10.1016/j.pmatsci.2013.10.001.

4 J. W. Yeh, Alloy Design Strategies and Future Trends in High-Entropy Alloys, *JOM*, 2013, **65**(12), 1759–1771, DOI: 10.1007/s11837-013-0761-6.

5 D. B. Miracle and O. N. Senkov, A Critical Review of High Entropy Alloys and Related Concepts, *Acta Mater.*, 2017, **122**, 448–511, DOI: 10.1016/j.actamat.2016.08.081.

6 J. W. Yeh, S. J. Chen, T. S. Chin, J. Y. Gan, S. K. Chen, T. T. Shun, C. H. Tsau and S. Y. Chou, Formation of Simple Crystal Structures in Cu–Co–Ni–Cr–Al–Fe–Ti–V Alloys with Multiprincipal Metallic Elements, *Metall. Mater. Trans. A*, 2004, **35**(8), 2533–2536.

7 B. S. Murty, J.-W. Yeh, S. Ranganathan and P. P. Bhattacharjee, *High-Entropy Alloys*, Google Books, https://books.google.com/books?hl=en&lr=&id=VU2NDwAAQBAJ&oi=fnd&pg=PP1&ots=_68YqvgEu9&sig=fZ2qQkGzzjU0CML6uDrU6WlFX3c#v=onepage&q&f=false, accessed Sep 11, 2020.

8 J.-W. Yeh, Recent Progress in High-Entropy Alloys, *Annales de Chimie Science des Matériaux*, 2006, **31**(6), 633–648, DOI: 10.3166/acsm.31.633-648.

9 C. M. Rost, E. Sachet, T. Borman, A. Moballegh, E. C. Dickey, D. Hou, J. L. Jones, S. Curtarolo and J. Maria, Entropy-Stabilized Oxides, *Nat. Commun.*, 2015, **6**, 1–8, DOI: 10.1038/ncomms9485.

10 R. Djenadic, A. Sarkar, O. Clemens, C. Loho, M. Botros, V. S. K. Chakravadhanula, C. Kübel, S. S. Bhattacharya, A. S. Gandhi and H. Hahn, Multicomponent Equiatomic Rare Earth Oxides, *Mater. Res. Lett.*, 2017, **5**(2), 102–109, DOI: 10.1080/21663831.2016.1220433.

11 J. Gild, M. Samiee, J. L. Braun, T. Harrington, H. Vega, P. E. Hopkins, K. Vecchio and J. Luo, High-Entropy Fluorite Oxides, *J. Eur. Ceram. Soc.*, 2018, **38**(10), 3578–3584, DOI: 10.1016/j.jeurceramsoc.2018.04.010.

12 K. Chen, X. Pei, L. Tang, H. Cheng, Z. Li, C. Li and X. Zhang, Short Communication: A Five-Component Entropy-Stabilized Fluorite Oxide, *J. Eur. Ceram. Soc.*, 2018, **38**(11), 4161–4164, DOI: 10.1016/j.jeurceramsoc.2018.04.063.

13 A. Sarkar, R. Djenadic, D. Wang, C. Hein, R. Kautenburger, O. Clemens and H. Hahn, Rare Earth and Transition Metal Based Entropy Stabilised Perovskite Type Oxides, *J. Eur. Ceram. Soc.*, 2018, **38**(5), 2318–2327, DOI: 10.1016/j.jeurceramsoc.2017.12.058.

14 S. Jiang, T. Hu, J. Gild, N. Zhou, J. Nie, M. Qin, T. Harrington, K. Vecchio and J. Luo, A New Class of High-Entropy Perovskite Oxides, *Scr. Mater.*, 2018, **142**, 116–120, DOI: 10.1016/j.scriptamat.2017.08.040.

15 J. Dąbrowa, M. Stygar, A. Mikuła, A. Knapik, K. Mroczka, W. Tejchman, M. Danielewski and M. Martin, Synthesis and Microstructure of the $(Co,Cr,Fe,Mn,Ni)_3O_4$ High Entropy Oxide Characterized by Spinel Structure, *Mater. Lett.*, 2018, **216**, 32–36, DOI: 10.1016/j.matlet.2017.12.148.

16 S. Wang, D. Wang, Z. Liu, S. Du, Y. Zhang, H. Li, R. Chen, Y. Wang, Y. Zou, Z. Xiao and W. Chen, Low-Temperature Synthesis of Small-Size High-Entropy Oxide for Water Oxidation, *J. Mater. Chem. A*, 2019, DOI: 10.1039/c9ta08740k.

17 J. Dusza, Š. Peter, V. Girman, R. Sedlák, E. G. Castle, T. Csanádi, A. Koval and M. J. Reece, Microstructure of (Hf–Ta–Zr–Nb)C High-Entropy Carbide at Micro and Nano/Atomic Level, *J. Eur. Ceram. Soc.*, 2018, **38**(May), 4303–4307, DOI: 10.1016/j.jeurceramsoc.2018.05.006.

18 J. Zhou, J. Zhang, F. Zhang, B. Niu, L. Lei and W. Wang, High-Entropy Carbide: A Novel Class of Multicomponent Ceramics, *Ceram. Int.*, 2018, **44**(17), 22014–22018, DOI: 10.1016/j.ceramint.2018.08.100.

19 L. Feng, W. G. Fahrenholtz, G. E. Hilmas and Y. Zhou, Synthesis of Single-Phase High-Entropy Carbide Powders, *Scr. Mater.*, 2019, **162**, 90–93, DOI: 10.1016/j.scriptamat.2018.10.049.

20 Y. Chu, First-Principles Study, Fabrication and Characterization of $(Zr_{0.25}Nb_{0.25}Ti_{0.25}V_{0.25})C$ high-entropy ceramics, *Acta Mater.*, 2019, **170**, 15–23, DOI: 10.1016/j.actamat.2019.03.021.

21 J. Gild, Y. Zhang, T. Harrington, S. Jiang, T. Hu, M. C. Quinn, W. M. Mellor, N. Zhou, K. Vecchio and J. Luo, High-entropy metal diborides: a new class of high-entropy materials and a new type of ultrahigh temperature ceramics, *Sci. Rep.*, 2016, **6**, 37946.

22 P. H. Mayrhofer, A. Kirnbauer, P. Ertelthaler and C. M. Koller, High-Entropy Ceramic Thin Films; A Case Study on Transition Metal Diborides, *Scr. Mater.*, 2018, **149**, 93–97, DOI: 10.1016/j.scriptamat.2018.02.008.

23 M. H. Hsieh, M. H. Tsai, W. J. Shen and J. W. Yeh, Structure and Properties of Two Al–Cr–Nb–Si–Ti High-Entropy Nitride Coatings, *Surf. Coat. Technol.*, 2013, **221**, 118–123, DOI: 10.1016/j.surfcoat.2013.01.036.

24 A. Mo, N. Ta, T. W. Si, J. Gild, J. Braun, K. Kaufmann, E. Marin, T. Harrington, P. Hopkins, K. Vecchio and J. Luo, A High-Entropy Silicide: $(Mo_{0.2}Nb_{0.2}Ta_{0.2}Ti_{0.2}W_{0.2})Si_2$, *J. Mater.*, 2019, DOI: 10.1016/j.jmat.2019.03.002.

25 R. Zhang, F. Gucci, H. Zhu, K. Chen and M. J. Reece, Data-Driven Design of Ecofriendly Thermoelectric High-Entropy Sulfides, *Inorg. Chem.*, 2018, **57**, 13027–13033, DOI: 10.1021/acs.inorgchem.8b02379.

26 X. Zhao, Z. Xue, W. Chen, Y. Wang and T. Mu, Eutectic Synthesis of High-Entropy Metal Phosphides for Electrocatalytic Water Splitting, *ChemSusChem*, 2020, 1–6, DOI: 10.1002/cssc.202000173.

27 T. Wang, H. Chen, Z. Yang, J. Liang and S. Dai, High-Entropy Perovskite Fluorides: A New Platform for Oxygen Evolution Catalysis, *J. Am. Chem. Soc.*, 2020, **142**(10), 4550–4554, DOI: 10.1021/jacs.9b12377.

28 W. Xu, H. Chen, K. Jie, Z. Yang, T. Li and S. Dai, Entropy-Driven Mechanochemical Synthesis of Polymetallic Zeolitic Imidazolate Frameworks for CO2 Fixation, *Angew. Chem.*, 2019, **131**(15), 5072–5076.

29 K. Huang, B. Zhang, J. Wu, T. Zhang, D. Peng, X. Cao, Z. Zhang, Z. Li and Y. Huang, Exploring the Impact of Atomic Lattice Deformation on Oxygen Evolution Reactions Based on a Sub-5 nm Pure Face-Centred Cubic High-Entropy Alloy Electrocatalyst, *J. Mater. Chem. A*, 2020, **8**(24), 11938–11947, DOI: 10.1039/d0ta02125c.

30 X. Zhao, Z. Xue, W. Chen, X. Bai, R. Shi and T. Mu, Ambient Fast, Large-Scale Synthesis of Entropy-Stabilized Metal–Organic Framework Nanosheets for Electrocatalytic Oxygen Evolution, *J. Mater. Chem. A*, 2019, 7(46), 26238–26242, DOI: 10.1039/c9ta09975a.

31 B. Feng and X. Zhuang, The Philosophy of Carbon: Meso-Entropy Materials, *Faraday Discuss.*, 2019, DOI: 10.1039/c9fd00115h.

32 C. F. Wu, D. E. S. Arifin, C. A. Wang and J. Ruan, Coalescence and Split of High-Entropy Polymer Lamellar Cocrystals, *Polymer*, 2018, **138**, 188–202, DOI: 10.1016/j.polymer.2018.01.064.

33 Y. F. Ye, Q. Wang, J. Lu, C. T. Liu and Y. Yang, High-Entropy Alloy: Challenges and Prospects, *Mater. Today*, 2016, **19**(6), 349–362, DOI: 10.1016/j.mattod.2015.11.026.

34 W. Zhang, P. K. Liaw and Y. Zhang, Science and technology in high-entropy alloys, *Sci. China Mater.*, 2018, **61**(1), 2–22.

35 J. W. Yeh and S. J. Lin, Breakthrough applications of high-entropy materials, *J. Mater. Res.*, 2018, **33**(19), 3129–3137.

36 E. P. George, D. Raabe and R. O. Ritchie, High-Entropy Alloys, *Nat. Rev. Mater.*, 2019, **4**(8), 515–534, DOI: 10.1038/s41578-019-0121-4.

37 W. Steurer, Single-Phase High-Entropy Alloys – A Critical Update, *Mater. Charact.*, 2020, **162**(February), 110179, DOI: 10.1016/j.matchar.2020.110179.

38 Y. Zhang, C. Wen, C. Wang, S. Antonov, D. Xue, Y. Bai and Y. Su, Phase Prediction in High Entropy Alloys with a Rational Selection of Materials Descriptors and Machine Learning Models, *Acta Mater.*, 2020, **185**, 528–539, DOI: 10.1016/j.actamat.2019.11.067.

39 M. C. Gao, Design of high-entropy alloys, In *High-Entropy Alloys*, 2016, Springer, Cham, pp. 369–398.

40 A. Sarkar, Q. Wang, A. Schiele, M. R. Chellali, S. S. Bhattacharya, D. Wang, T. Brezesinski, H. Hahn, L. Velasco and B. Breitung, High-entropy oxides: fundamental aspects and electrochemical properties, *Adv. Mater.*, 2019, **31**(26), 1806236.

41 Y. Zhang, Y. J. Zhou, J. P. Lin, G. L. Chen and P. K. Liaw, Solid-solution phase formation rules for multi-component alloys, *Adv. Eng. Mater.*, 2008, **10**(6), 534–538.

42 S. Guo and C. T. Liu, Phase Stability in High Entropy Alloys: Formation of Solid-Solution Phase or Amorphous Phase, *Prog. Nat. Sci. Mater. Int.*, 2011, **21**(6), 433–446, DOI: 10.1016/S1002-0071(12)60080-X.

43 X. Yang and Y. Zhang, Prediction of High-Entropy Stabilized Solid-Solution in Multi-Component Alloys, *Mater. Chem. Phys.*, 2012, **132**(2–3), 233–238, DOI: 10.1016/j.matchemphys.2011.11.021.

44 M. C. Troparevsky, J. R. Morris, P. R. Kent, A. R. Lupini and G. M. Stocks, Criteria for predicting the formation of single-phase high-entropy alloys, *Phys. Rev. X*, 2015, **5**(1), 011041.

45 A. K. Singh, N. Kumar, A. Dwivedi and A. Subramaniam, A Geometrical Parameter for the Formation of Disordered Solid Solutions in Multi-Component Alloys, *Intermetallics*, 2014, **53**, 112–119, DOI: 10.1016/j.intermet.2014.04.019.

46 S. Guo, C. Ng, J. Lu and C. T. Liu, Effect of valence electron concentration on stability of fcc or bcc phase in high entropy alloys, *J. Appl. Phys.*, 2011, **109**(10), 103505.

47 Y. F. Ye, Q. Wang, J. Lu, C. T. Liu and Y. Yang, Design of High Entropy Alloys: A Single-Parameter Thermodynamic Rule, *Scr. Mater.*, 2015, **104**, 53–55, DOI: 10.1016/j.scriptamat.2015.03.023.

48 Y. F. Ye, Q. Wang, J. Lu, C. T. Liu and Y. Yang, The Generalized Thermodynamic Rule for Phase Selection in Multicomponent Alloys, *Intermetallics*, 2015, **59**, 75–80, DOI: 10.1016/j.intermet.2014.12.011.

49 M. G. Poletti and L. Battezzati, ScienceDirect Electronic and Thermodynamic Criteria for the Occurrence of High Entropy Alloys in Metallic Systems, *Acta Mater.*, 2014, **75**, 297–306, DOI: 10.1016/j.actamat.2014.04.033.

50 A. R. Miedema, P. F. de Châtel and F. R. de Boer, Cohesion in Alloys - Fundamentals of a Semi-Empirical Model, *Phys. B+C*, 1980, **100**(1), 1–28, DOI: 10.1016/0378-4363(80)90054-6.

51 K. Zhang and Z. Fu, Effects of Annealing Treatment on Phase Composition and Microstructure of $CoCrFeNiTiAl_x$ High-Entropy Alloys, *Intermetallics*, 2012, **22**, 24–32, DOI: 10.1016/j.intermet.2011.10.010.

52 J. B. Mann, T. L. Meek and L. C. Allen, Configuration energies of the main group elements, *J. Am. Chem. Soc.*, 2000, **122**(12), 2780–2783.

53 A. Takeuchi, K. Amiya, T. Wada, K. Yubuta and W. Zhang, High-Entropy Alloys with a Hexagonal Close-Packed Structure Designed by Equi-Atomic Alloy Strategy and Binary Phase Diagrams, *JOM*, 2014, **66**(10), 1984–1992, DOI: 10.1007/s11837-014-1085-x.

54 Y. J. Zhao, J. W. Qiao, S. G. Ma, M. C. Gao, H. J. Yang, M. W. Chen and Y. Zhang, A Hexagonal Close-Packed High-Entropy Alloy: The Effect of Entropy, *Mater. Des.*, 2016, **96**, 10–15, DOI: 10.1016/j.matdes.2016.01.149.

55 M. Feuerbacher, M. Heidelmann and C. Thomas, Hexagonal High-Entropy Alloys, *Mater. Res. Lett.*, 2014, **3**(1), 1–6, DOI: 10.1080/21663831.2014.951493.

56 S. Guo, C. Ng, J. Lu and C. T. Liu, Effect of valence electron concentration on stability of fcc or bcc phase in high entropy alloys, *J. Appl. Phys.*, 2011, **109**(10), 103505.

57 *Hume-Rothery Rules for Structurally Complex Alloy Phases*, 1st edn https://www.routledge.com/Hume-Rothery-Rules-for-Structurally-Complex-Alloy-Phases/Mizutani/p/book/9780367383374, accessed Nov 2, 2020.

58 F. Wang, Y. Zhang, G. Chen and H. A. Davies, Tensile and Compressive Mechanical Behavior of a $CoCrCuFeNiAl_{0.5}$ High Entropy Alloy, *Int. J. Mod. Phys. B*, 2009, **23**, 1254–1259, DOI: 10.1142/s0217979209060774.

59 O. N. Senkov, G. B. Wilks, D. B. Miracle, C. P. Chuang and P. K. Liaw, Refractory High-Entropy Alloys, *Intermetallics*, 2010, **18**(9), 1758–1765, DOI: 10.1016/j.intermet.2010.05.014.

60 G. A. Mansoori, N. F. Carnahan, K. E. Starling and T. W. Leland, Equilibrium Thermodynamic Properties of the Mixture of Hard Spheres, *J. Chem. Phys.*, 1971, **54**(4), 1523–1525, DOI: 10.1063/1.1675048.

61 Y. Yang, B. Song, X. Ke, F. Xu, K. N. Bozhilov, L. Hu, R. Shahbazian-Yassar and M. R. Zachariah, Aerosol synthesis of high entropy alloy nanoparticles, *Langmuir*, 2020, **36**(8), 1985–1992.

62 F. He, Z. Wang, Y. Li, Q. Wu, J. Li, J. Wang and C. T. Liu, Kinetic Ways of Tailoring Phases in High Entropy Alloys, *Sci. Rep.*, 2016, **6**(September), 1–9, DOI: 10.1038/srep34628.

63 H. W. Luan, Y. Shao, J. F. Li, W. L. Mao, Z. D. Han, C. Shao and K. F. Yao, Phase Stabilities of High Entropy Alloys, *Scr. Mater.*, 2020, **179**, 40–44, DOI: 10.1016/j.scriptamat.2019.12.041.

64 G. Anand, A. P. Wynn, C. M. Handley and C. L. Freeman, Phase Stability and Distortion in High-Entropy Oxides, *Acta Mater.*, 2018, **146**, 119–125, DOI: 10.1016/j.actamat.2017.12.037.

65 Q. Wu, Z. Wang, F. He, L. Wang, J. Luo, J. Li and J. Wang, High Entropy Alloys: From Bulk Metallic Materials to Nanoparticles, *Metall. Mater. Trans. A*, 2018, **49**(10), 4986–4990, DOI: 10.1007/s11661-018-4802-1.

66 Y. Zhang, Y. J. Zhou, J. P. Lin, G. L. Chen and P. K. Liaw, Solid-Solution Phase Formation Rules for Multi-Component Alloys, *Adv. Eng. Mater.*, 2008, **10**(6), 534–538, DOI: 10.1002/adem.200700240.

67 J. W. Yeh, S. K. Chen, S. J. Lin, J. Y. Gan, T. S. Chin, T. T. Shun, C. H. Tsau and S. Y. Chang, Nanostructured High-Entropy Alloys with Multiple Principal Elements: Novel Alloy Design Concepts and Outcomes, *Adv. Eng. Mater.*, 2004, **6**(5), 299–303, DOI: 10.1002/adem.200300567.

68 X. Chen, C. Si, Y. Gao, J. Frenzel, J. Sun, G. Eggeler and Z. Zhang, Multi-Component Nanoporous Platinum–Ruthenium–Copper–Osmium–Iridium Alloy with Enhanced Electrocatalytic Activity Towards Methanol Oxidation and Oxygen Reduction, *J. Power Sources*, 2015, **273**, 324–332, DOI: 10.1016/j.jpowsour.2014.09.076.

69 M. Y. Rekha, N. Mallik and C. Srivastava, First Report on High Entropy Alloy Nanoparticle Decorated Graphene, *Sci. Rep.*, 2018, **8**(1), 8737, DOI: 10.1038/s41598-018-27096-8.

70 H.-J. Qiu, G. Fang, J. Gao, Y. Wen, J. Lv, H. Li, G. Xie, X. Liu and S. Sun, Noble Metal-Free Nanoporous High-Entropy Alloys as Highly Efficient Electrocatalysts for Oxygen Evolution Reaction, *ACS Mater. Lett.*, 2019, **1**(5), 526–533, DOI: 10.1021/acsmaterialslett.9b00414.

71 S. Li, X. Tang, H. Jia, H. Li, G. Xie, X. Liu, X. Lin and H. J. Qiu, Nanoporous High-Entropy Alloys with Low Pt Loadings for High-Performance Electrochemical Oxygen Reduction, *J. Catal.*, 2020, **383**, 164–171, DOI: 10.1016/j.jcat.2020.01.024.

72 H. J. Qiu, G. Fang, Y. Wen, P. Liu, G. Xie, X. Liu and S. Sun, Nanoporous High-Entropy Alloys for Highly Stable and Efficient Catalysts, *J. Mater. Chem. A*, 2019, **7**(11), 6499–6506, DOI: 10.1039/c9ta00505f.

73 M. Bondesgaard, N. L. N. Broge, A. Mamakhel, M. Bremholm and B. B. Iversen, General Solvothermal Synthesis Method for Complete Solubility Range Bimetallic and High-Entropy Alloy Nanocatalysts, *Adv. Funct. Mater.*, 2019, **29**(50), 1905933, DOI: 10.1002/adfm.201905933.

74 M. Liu, Z. Zhang, F. Okejiri, S. Yang, S. Zhou and S. Dai, Entropy-Maximized Synthesis of Multimetallic Nanoparticle Catalysts via a Ultrasonication-Assisted Wet Chemistry Method under Ambient Conditions, *Adv. Mater. Interfaces*, 2019, **6**(7), 1900015, DOI: 10.1002/admi.201900015.

75 B. Niu, F. Zhang, H. Ping, N. Li, J. Zhou, L. Lei, J. Xie, J. Zhang, W. Wang and Z. Fu, Sol–Gel Autocombustion Synthesis of Nanocrystalline High-Entropy Alloys, *Sci. Rep.*, 2017, **7**(1), 1–7, DOI: 10.1038/s41598-017-03644-6.

76 P. Xie, Y. Yao, Z. Huang, Z. Liu, J. Zhang, T. Li, G. Wang, R. Shahbazian-Yassar, L. Hu and C. Wang, Highly Efficient Decomposition of Ammonia Using High-Entropy Alloy Catalysts, *Nat. Commun.*, 2019, **10**(1), 1–12, DOI: 10.1038/s41467-019-11848-9.

77 Y. Yao, Z. Huang, P. Xie, S. D. Lacey, R. J. Jacob, H. Xie, F. Chen, A. Nie, T. Pu, M. Rehwoldt, D. Yu, M. R. Zachariah, C. Wang, R. Shahbazian-Yassar, J. Li and L. Hu, Carbothermal Shock Synthesis of High-Entropy-Alloy Nanoparticles, *Science*, 2018, **359**(6383), 1489–1494, DOI: 10.1126/science.aan5412.

78 X. Xu, Y. Du, C. Wang, Y. Guo, J. Zou, K. Zhou, Z. Zeng, Y. Liu and L. Li, High-entropy alloy nanoparticles on aligned electronspun carbon nanofibers for supercapacitors, *J. Alloys Compd.*, 2020, **822**, 153642.

79 S. Gao, S. Hao, Z. Huang, Y. Yuan, S. Han, L. Lei, X. Zhang, R. Shahbazian-Yassar and J. Lu, Synthesis of High-Entropy Alloy Nanoparticles on Supports by the Fast Moving Bed Pyrolysis, *Nat. Commun.*, 2020, **11**(1), DOI: 10.1038/s41467-020-15934-1.

80 T. Löffler, H. Meyer, A. Savan, P. Wilde, A. Garzón Manjón, Y.-T. Chen, E. Ventosa, C. Scheu, A. Ludwig and W. Schuhmann, Discovery of a Multinary Noble Metal-

Free Oxygen Reduction Catalyst, *Adv. Energy Mater.*, 2018, **8**(34), 1802269, DOI: 10.1002/aenm.201802269.

81 C. F. Tsai, P. W. Wu, P. Lin, C. G. Chao and K. Y. Yeh, Sputter Deposition of Multi-Element Nanoparticles as Eleetrocatalysts for Methanol Oxidation, *Jpn. J. Appl. Phys.*, 2008, **47**(7 Part 1), 5755–5761, DOI: 10.1143/JJAP.47.5755.

82 G. M. Tomboc, T. Kwon, J. Joo and K. Lee, High Entropy Alloy Electrocatalysts: A Critical Assessment of Fabrication and Performance, *J. Mater. Chem. A*, 2020, **8**(30), 14844–14862, DOI: 10.1039/d0ta05176d.

83 Y. Xin, S. Li, Y. Qian, W. Zhu, H. Yuan, P. Jiang, R. Guo and L. Wang, High-Entropy Alloys as a Platform for Catalysis: Progress, Challenges, and Opportunities, *ACS Catal.*, 2020, 11280–11306, DOI: 10.1021/acscatal.0c03617.

84 A. Ostovari Moghaddam and E. A. Trofimov, Toward Expanding the Realm of High Entropy Materials to Platinum Group Metals: A Review, *J. Alloys Compd.*, 2021, 851, DOI: 10.1016/j.jallcom.2020.156838.

85 I. U. M. R. Cnrs, U. Paris-sud, U. Paris-saclay, D. Bérardan, S. Franger, D. Dragoe, A. K. Meena and N. Dragoe, Colossal Dielectric Constant in High Entropy Oxides, *Phys. Status Solidi*, 2016, **333**(4), 328–333, DOI: 10.1002/pssr.201600043.

86 A. Sarkar, R. Djenadic, N. J. Usharani, K. P. Sanghvi, V. S. K. Chakravadhanula, A. S. Gandhi, H. Hahn and S. S. Bhattacharya, Nanocrystalline Multicomponent Entropy Stabilised Transition Metal Oxides, *J. Eur. Ceram. Soc.*, 2017, **37**(2), 747–754, DOI: 10.1016/j.jeurceramsoc.2016.09.018.

87 M. Biesuz, L. Spiridigliozzi, G. Dell'Agli, M. Bortolotti and V. M. Sglavo, Synthesis and Sintering of (Mg,Co,Ni,Cu,Zn) O Entropy-Stabilized Oxides Obtained by Wet Chemical Methods, *J. Mater. Sci.*, 2018, **53**(11), 8074–8085, DOI: 10.1007/s10853-018-2168-9.

88 D. Wang, Z. Liu, S. Du, Y. Zhang, H. Li, Z. Xiao, W. Chen, R. Chen, Y. Wang, Y. Zou and S. Wang, Low-Temperature Synthesis of Small-Sized High-Entropy Oxides for Water Oxidation, *J. Mater. Chem. A*, 2019, **7**(42), 24211–24216, DOI: 10.1039/c9ta08740k.

89 R. Djenadic, A. Sarkar, O. Clemens, C. Loho, M. Botros, V. S. K. Chakravadhanula, C. Kübel, S. S. Bhattacharya, A. S. Gandhi and H. Hahn, Multicomponent Equiatomic Rare Earth Oxides, *Mater. Res. Lett.*, 2017, **5**(2), 102–109, DOI: 10.1080/21663831.2016.1220433.

90 A. Sarkar, R. Djenadic, D. Wang, C. Hein, R. Kautenburger, O. Clemens and H. Hahn, Rare Earth and Transition Metal Based Entropy Stabilised Perovskite Type Oxides, *J. Eur. Ceram. Soc.*, 2018, **38**(5), 2318–2327, DOI: 10.1016/j.jeurceramsoc.2017.12.058.

91 H. Chen, W. Lin, Z. Zhang, K. Jie, D. R. Mullins, X. Sang, S. Z. Yang, C. J. Jafta, C. A. Bridges, X. Hu, R. R. Unocic, J. Fu, P. Zhang and S. Dai, Mechanochemical Synthesis of High Entropy Oxide Materials under Ambient Conditions: Dispersion of Catalysts via Entropy Maximization, *ACS Mater. Lett.*, 2019, **1**(1), 83–88, DOI: 10.1021/acsmaterialslett.9b00064.

92 M. Balcerzak, K. Kawamura, R. Bobrowski, P. Rutkowski and T. Brylewski, Mechanochemical Synthesis of (Co,Cu,Mg,Ni,Zn)O High-Entropy Oxide and Its Physicochemical Properties, *J. Electron. Mater.*, 2019, **48**(11), 7105–7113, DOI: 10.1007/s11664-019-07512-z.

93 F. Okejiri, Z. Zhang, J. Liu, M. Liu, S. Yang and S. Dai, Room-Temperature Synthesis of High-Entropy Perovskite Oxide Nanoparticle Catalysts through Ultrasonication-Based Method, *ChemSusChem*, 2020, **13**(1), 111–115, DOI: 10.1002/cssc.201902705.

94 A. Mao, H. Z. Xiang, Z. G. Zhang, K. Kuramoto, H. Yu and S. Ran, Solution Combustion Synthesis and Magnetic Property of Rock-Salt $(Co_{0.2}Cu_{0.2}Mg_{0.2}Ni_{0.2}Zn_{0.2})O$ High-Entropy Oxide Nanocrystalline Powder, *J. Magn. Magn. Mater.*, 2019, **484**, 245–252, DOI: 10.1016/j.jmmm.2019.04.023.

95 A. Sarkar, B. Breitung and H. Hahn, High Entropy Oxides: The Role of Entropy, Enthalpy and Synergy, *Scr. Mater.*, 2020, **187**, 43–48, DOI: 10.1016/j.scriptamat.2020.05.019.

96 Y. Xin, S. Li, Y. Qian, W. Zhu, H. Yuan, P. Jiang, R. Guo and L. Wang, High-Entropy Alloys as a Platform for Catalysis: Progress, Challenges, and Opportunities, *ACS Catal.*, 2020, 11280–11306, DOI: 10.1021/acscatal.0c03617.

97 D. Titus, E. James Jebaseelan Samuel and S. M. Roopan, Nanoparticle Characterization Techniques, in *Green Synthesis, Characterization and Applications of Nanoparticles*, Elsevier, 2019, pp. 303–319, DOI: 10.1016/b978-0-08-102579-6.00012-5.

98 S. Mourdikoudis, R. M. Pallares and N. T. K. Thanh, Characterization Techniques for Nanoparticles: Comparison and Complementarity upon Studying Nanoparticle Properties, *Nanoscale*, 2018, 12871–12934, DOI: 10.1039/c8nr02278j.

99 H. J. Qiu, G. Fang, Y. Wen, P. Liu, G. Xie, X. Liu and S. Sun, Nanoporous High-Entropy Alloys for Highly Stable and Efficient Catalysts, *J. Mater. Chem. A*, 2019, **7**(11), 6499–6506, DOI: 10.1039/c9ta00505f.

100 F. Waag, Y. Li, A. R. Ziefuß, E. Bertin, M. Kamp, V. Duppel, G. Marzun, L. Kienle, S. Barcikowski and B. Gökce, Kinetically-Controlled Laser-Synthesis of Colloidal High-Entropy Alloy Nanoparticles, *RSC Adv.*, 2019, **9**(32), 18547–18558, DOI: 10.1039/c9ra03254a.

101 Y. Yao, Z. Liu, P. Xie, Z. Huang, T. Li, D. Morris, Z. Finfrock, J. Zhou, M. Jiao, J. Gao, Y. Mao, J. Miao, P. Zhang, R. Shahbazian-Yassar, C. Wang, G. Wang and L. Hu, Computationally Aided, Entropy-Driven Synthesis of Highly Efficient and Durable Multi-Elemental Alloy Catalysts, *Sci. Adv.*, 2020, **6**(11), 510–523, DOI: 10.1126/sciadv.aaz0510.

102 K. M. McGrath, G. S. Prakash and G. A. Olah, Direct methanol fuel cells, *J. Ind. Eng. Chem.*, 2004, **10**(7), 1063–1080.

103 C. F. Tsai, P. W. Wu, P. Lin, C. G. Chao and K. Y. Yeh, Sputter deposition of multi-element nanoparticles as electrocatalysts for methanol oxidation, *Jpn. J. Appl. Phys.*, 2008, **47**(7R), 5755.

104 E. Reddington, A. Sapienza, B. Gurau, R. Viswanathan, S. Sarangapani, E. S. Smotkin and T. E. Mallouk, Combinatorial electrochemistry: a highly parallel, optical

screening method for discovery of better electrocatalysts, *Science*, 1998, **280**(5370), 1735–1737.

105 B. Gurau, R. Viswanathan, R. Liu, T. J. Lafrenz, K. L. Ley, E. S. Smotkin, E. Reddington, A. Sapienza, B. C. Chan, T. E. Mallouk and S. Sarangapani, Structural and electrochemical characterization of binary, ternary, and quaternary platinum alloy catalysts for methanol electrooxidation, *J. Phys. Chem. B*, 1998, **102**(49), 9997–10003.

106 H. Igarashi, T. Fujino, Y. Zhu, H. Uchida and M. Watanabe, CO tolerance of Pt alloy electrocatalysts for polymer electrolyte fuel cells and the detoxification mechanism, *Phys. Chem. Chem. Phys.*, 2001, **3**(3), 306–314.

107 H. Uchida, H. Ozuka and M. Watanabe, Electrochemical quartz crystal microbalance analysis of CO-tolerance at Pt Fe alloy electrodes, *Electrochim. Acta*, 2002, **47**(22–23), 3629–3636.

108 J. W. Guo, T. S. Zhao, J. Prabhuram, R. Chen and C. W. Wong, Preparation and characterization of a PtRu/C nanocatalyst for direct methanol fuel cells, *Electrochim. Acta*, 2005, **51**(4), 754–763.

109 T. Yajima, H. Uchida and M. Watanabe, In Situ ATR-FTIR Spectroscopic Study of Electro-Oxidation of Methanol and Adsorbed CO at Pt–Ru Alloy, *J. Phys. Chem. B*, 2004, **108**(8), 2654–2659, DOI: 10.1021/jp037215q.

110 L. Zou, J. Guo, J. Liu, Z. Zou, D. L. Akins and H. Yang, Highly Alloyed PtRu Black Electrocatalysts for Methanol Oxidation Prepared Using Magnesia Nanoparticles as Sacrificial Templates, *J. Power Sources*, 2014, **248**, 356–362, DOI: 10.1016/j.jpowsour.2013.09.086.

111 P. Strasser, Q. Fan, M. Devenney, W. H. Weinberg, P. Liu and J. K. Nørskov, High throughput experimental and theoretical predictive screening of materials—a comparative study of search strategies for new fuel cell anode catalysts, *J. Phys. Chem. B*, 2003, **107**(40), 11013–11021.

112 K. W. Park, J. H. Choi, S. A. Lee, C. Pak, H. Chang and Y. E. Sung, PtRuRhNi nanoparticle electrocatalyst for methanol electrooxidation in direct methanol fuel cell, *J. Catal.*, 2004, **224**(2), 236–242.

113 J. F. Whitacre, T. Valdez and S. R. Narayanan, Investigation of direct methanol fuel cell electrocatalysts using a robust combinatorial technique, *J. Electrochem. Soc.*, 2005, **152**(9), A1780.

114 W. Dai, T. Lu and Y. Pan, Novel and Promising Electrocatalyst for Oxygen Evolution Reaction Based on MnFeCoNi High Entropy Alloy, *J. Power Sources*, 2019, **430**(April), 104–111, DOI: 10.1016/j.jpowsour.2019.05.030.

115 C. F. Tsai, K. Y. Yeh, P. W. Wu, Y. F. Hsieh and P. Lin, Effect of platinum present in multi-element nanoparticles on methanol oxidation, *J. Alloys Compd.*, 2009, **478**(1–2), 868–871.

116 X. Chen, C. Si, Y. Gao, J. Frenzel, J. Sun, G. Eggeler and Z. Zhang, Multi-Component Nanoporous Platinum–Ruthenium–Copper–Osmium–Iridium Alloy with Enhanced Electrocatalytic Activity towards Methanol Oxidation and Oxygen Reduction, *J. Power Sources*, 2015, **273**, 324–332, DOI: 10.1016/j.jpowsour.2014.09.076.

117 Y. X. Chen, A. Lavacchi, S. P. Chen, F. Di Benedetto, M. Bevilacqua, C. Bianchini, P. Fornasiero, M. Innocenti, M. Marelli, W. Oberhauser, S. G. Sun and F. Vizza, Electrochemical Milling and Faceting: Size Reduction and Catalytic Activation of Palladium Nanoparticles, *Angew. Chem., Int. Ed.*, 2012, **51**(34), 8500–8504, DOI: 10.1002/anie.201203589.

118 N. Tian, Z. Y. Zhou and S. G. Sun, Electrochemical Preparation of Pd Nanorods with High-Index Facets, *Chem. Commun.*, 2009, (No. 12), 1502–1504, DOI: 10.1039/b819751b.

119 Y. Xing, Y. Cai, M. B. Vukmirovic, W. P. Zhou, H. Karan, J. X. Wang and R. R. Adzic, Enhancing Oxygen Reduction Reaction Activity via Pd–Au Alloy Sublayer Mediation of Pt Monolayer Electrocatalysts, *J. Phys. Chem. Lett.*, 2010, **1**(21), 3238–3242, DOI: 10.1021/jz101297r.

120 V. Mazumder, M. Chi, M. N. Mankin, Y. Liu, Ö. Metin, D. Sun, K. L. More and S. Sun, A Facile Synthesis of MPd (M = Co, Cu) Nanoparticles and Their Catalysis for Formic Acid Oxidation, *Nano Lett.*, 2012, **12**(2), 1102–1106, DOI: 10.1021/nl2045588.

121 W. Du, K. E. MacKenzie, D. F. Milano, N. A. Deskins, D. Su and X. Teng, Palladium–Tin Alloyed Catalysts for the Ethanol Oxidation Reaction in an Alkaline Medium, *ACS Catal.*, 2012, **2**(2), 287–297, DOI: 10.1021/cs2005955.

122 A. L. Wang, H. C. Wan, H. Xu, Y. X. Tong and G. R. Li, Quinary PdNiCoCuFe Alloy Nanotube Arrays as Efficient Electrocatalysts for Methanol Oxidation, *Electrochim. Acta*, 2014, **127**, 448–453, DOI: 10.1016/j.electacta.2014.02.076.

123 Y. Wang, S. Zou and W. B. Cai, Recent Advances on Electro-Oxidation of Ethanol on Pt-and Pd-Based Catalysts: From Reaction Mechanisms to Catalytic Materials, *Catalysts*, 2015, 1507–1534, http://mdpi.com.

124 X. Fang, L. Wang, P. K. Shen, G. Cui and C. Bianchini, An In Situ Fourier Transform Infrared Spectroelectrochemical Study on Ethanol Electrooxidation on Pd in Alkaline Solution, *J. Power Sources*, 2010, **195**(5), 1375–1378, DOI: 10.1016/j.jpowsour.2009.09.025.

125 S. C. S. Lai and M. T. M. Koper, The Influence of Surface Structure on Selectivity in the Ethanol Electro-Oxidation Reaction on Platinum, *J. Phys. Chem. Lett.*, 2010, **1**(7), 1122–1125, DOI: 10.1021/jz100272f.

126 W. J. Pech-Rodríguez, D. González-Quijano, G. Vargas-Gutiérrez, C. Morais, T. W. Napporn and F. J. Rodríguez-Varela, Electrochemical and In Situ FTIR Study of the Ethanol Oxidation Reaction on PtMo/C Nanomaterials in Alkaline Media, *Appl. Catal., B*, 2017, **203**, 654–662, DOI: 10.1016/j.apcatb.2016.10.058.

127 D. Wu, K. Kusada, T. Yamamoto, T. Toriyama, S. Matsumura, S. Kawaguchi, Y. Kubota and H. Kitagawa, Platinum-Group-Metal High-Entropy-Alloy Nanoparticles, *J. Am. Chem. Soc.*, 2020, **142**(32), 13833–13838, DOI: 10.1021/jacs.0c04807.

128 Z. Liang, L. Song, S. Deng, Y. Zhu, E. Stavitski, R. R. Adzic, J. Chen and J. X. Wang, Direct 12-Electron Oxidation of Ethanol on a Ternary Au(Core)–PtIr(Shell) Electrocatalyst,

J. Am. Chem. Soc., 2019, **141**(24), 9629–9636, DOI: 10.1021/jacs.9b03474.

129 M. D. Marcinkowski, J. Liu, C. J. Murphy, M. L. Liriano, N. A. Wasio, F. R. Lucci, M. Flytzani-Stephanopoulos and E. C. H. Sykes, Selective Formic Acid Dehydrogenation on Pt–Cu Single-Atom Alloys, *ACS Catal.*, 2017, **7**(1), 413–420, DOI: 10.1021/acscatal.6b02772.

130 J. Kim, C. W. Roh, S. K. Sahoo, S. Yang, J. Bae, J. W. Han and H. Lee, Highly Durable Platinum Single-Atom Alloy Catalyst for Electrochemical Reactions, *Adv. Energy Mater.*, 2018, **8**(1), 1–8, DOI: 10.1002/aenm.201701476.

131 A. X. Yin, X. Q. Min, Y. W. Zhang and C. H. Yan, Shape-Selective Synthesis and Facet-Dependent Enhanced Electrocatalytic Activity and Durability of Monodisperse Sub-10 nm Pt–Pd Tetrahedrons and Cubes, *J. Am. Chem. Soc.*, 2011, **133**(11), 3816–3819, DOI: 10.1021/ja200329p.

132 S. Zhang, Y. Shao, G. Yin and Y. Lin, Electrostatic Self-Assembly of a Pt-around-Au Nanocomposite with High Activity Towards Formic Acid Oxidation, *Angew. Chem., Int. Ed.*, 2010, **49**(12), 2211–2214, DOI: 10.1002/anie.200906987.

133 R. Iyyamperumal, L. Zhang, G. Henkelman and R. M. Crooks, Efficient Electrocatalytic Oxidation of Formic Acid Using Au@Pt Dendrimer-Encapsulated Nanoparticles, *J. Am. Chem. Soc.*, 2013, **135**(15), 5521–5524, DOI: 10.1021/ja4010305.

134 N. K. Katiyar, S. Nellaiappan, R. Kumar, K. D. Malviya, K. G. Pradeep, A. K. Singh, S. Sharma, C. S. Tiwary and K. Biswas, Formic Acid and Methanol Electro-Oxidation and Counter Hydrogen Production Using Nano High Entropy Catalyst, *Mater. Today Energy*, 2020, **16**, 100393, DOI: 10.1016/j.mtener.2020.100393.

135 J. Li, H. S. Stein, K. Sliozberg, J. Liu, Y. Liu, G. Sertic, E. Scanley, A. Ludwig, J. Schroers, W. Schuhmann and A. D. Taylor, Combinatorial screening of Pd-based quaternary electrocatalysts for oxygen reduction reaction in alkaline media, *J. Mater. Chem. A*, 2017, **5**(1), 67–72.

136 A. E. Chan, R. Hoffmann and W. Ho, Theoretical aspects of photoinitiated chemisorption, dissociation, and desorption of oxygen on platinum (111), *Langmuir*, 1992, **8**(4), 1111–1119.

137 M. Shao, Q. Chang, J. P. Dodelet and R. Chenitz, Recent advances in electrocatalysts for oxygen reduction reaction, *Chem. Rev.*, 2016, **116**(6), 3594–3657.

138 T. Löffler, H. Meyer, A. Savan, P. Wilde, A. Garzón Manjón, Y. T. Chen, E. Ventosa, C. Scheu, A. Ludwig and W. Schuhmann, Discovery of a Multinary Noble Metal-Free Oxygen Reduction Catalyst, *Adv. Energy Mater.*, 2018, **8**(34), 1–7, DOI: 10.1002/aenm.201802269.

139 H. J. Qiu, G. Fang, Y. Wen, P. Liu, G. Xie, X. Liu and S. Sun, Nanoporous High-Entropy Alloys for Highly Stable and Efficient Catalysts, *J. Mater. Chem. A*, 2019, **7**(11), 6499–6506, DOI: 10.1039/c9ta00505f.

140 Y. Yao, Z. Huang, T. Li, H. Wang, Y. Liu, H. S. Stein, Y. Mao, J. Gao, M. Jiao, Q. Dong, J. Dai, P. Xie, H. Xie, S. D. Lacey, I. Takeuchi, J. M. Gregoire, R. Jiang, C. Wang, A. D. Taylor, R. Shahbazian-Yassar and L. Hu, High-Throughput, Combinatorial Synthesis of Multimetallic Nanoclusters, *Proc. Natl. Acad. Sci. U. S. A.*, 2020, **117**(12), 6316–6322, DOI: 10.1073/pnas.1903721117.

141 T. A. A. Batchelor, J. K. Pedersen, S. H. Winther, I. E. Castelli, K. W. Jacobsen and J. Rossmeisl, High-Entropy Alloys as a Discovery Platform for Electrocatalysis, *Joule*, 2019, **3**(3), 834–845, DOI: 10.1016/j.joule.2018.12.015.

142 S. Chu and A. Majumdar, Opportunities and Challenges for a Sustainable Energy Future, *Nature*, 2012, **488**(7411), 294–303, DOI: 10.1038/nature11475.

143 R. Solmaz and G. Kardaş, Electrochemical Deposition and Characterization of NiFe Coatings as Electrocatalytic Materials for Alkaline Water Electrolysis, *Electrochim. Acta*, 2009, **54**(14), 3726–3734, DOI: 10.1016/j.electacta.2009.01.064.

144 Y. Li and J. Z. Zhang, Hydrogen Generation from Photoelectrochemical Water Splitting Based on Nanomaterials, *Laser Photonics Rev.*, 2010, **4**(4), 517–528, DOI: 10.1002/lpor.200910025.

145 A. R. Zeradjanin, J. P. Grote, G. Polymeros and K. J. J. Mayrhofer, A Critical Review on Hydrogen Evolution Electrocatalysis: Re-Exploring the Volcano-Relationship, *Electroanalysis*, 2016, **28**(10), 2256–2269, DOI: 10.1002/elan.201600270.

146 Y. Liang, Y. Li, H. Wang and H. Dai, Strongly Coupled Inorganic/Nanocarbon Hybrid Materials for Advanced Electrocatalysis, *J. Am. Chem. Soc.*, 2013, **135**(6), 2013–2036, DOI: 10.1021/ja3089923.

147 G. R. Xu, J. Bai, J. X. Jiang, J. M. Lee and Y. Chen, Polyethyleneimine Functionalized Platinum Superstructures: Enhancing Hydrogen Evolution Performance by Morphological and Interfacial Control, *Chem. Sci.*, 2017, **8**(12), 8411–8418, DOI: 10.1039/c7sc04109h.

148 Y. Lee, J. Suntivich, K. J. May, E. E. Perry and Y. Shao-Horn, Synthesis and Activities of Rutile IrO_2 and RuO_2 Nanoparticles for Oxygen Evolution in Acid and Alkaline Solutions, *J. Phys. Chem. Lett.*, 2012, **3**(3), 399–404, DOI: 10.1021/jz2016507.

149 M. M. Jaksic, Hypo–hyper-d-electronic interactive nature of interionic synergism in catalysis and electrocatalysis for hydrogen reactions, *Int. J. Hydrogen Energy*, 2001, **26**(6), 559–578.

150 J. R. McKone, B. F. Sadtler, C. A. Werlang, N. S. Lewis and H. B. Gray, Ni–Mo Nanopowders for Efficient Electrochemical Hydrogen Evolution, *ACS Catal.*, 2013, **3**(2), 166–169, DOI: 10.1021/cs300691m.

151 N. R. Elezović, V. D. Jović and N. V. Krstajić, Kinetics of the Hydrogen Evolution Reaction on Fe–Mo Film Deposited on Mild Steel Support in Alkaline Solution, *Electrochim. Acta*, 2005, **50**(28), 5594–5601, DOI: 10.1016/j.electacta.2005.03.037.

152 M. Schalenbach, F. D. Speck, M. Ledendecker, O. Kasian, D. Goehl, A. M. Mingers, B. Breitbach, H. Springer, S. Cherevko and K. J. J. Mayrhofer, Nickel–Molybdenum Alloy Catalysts for the Hydrogen Evolution Reaction:

Activity and Stability Revised, *Electrochim. Acta*, 2018, **259**, 1154–1161, DOI: 10.1016/j.electacta.2017.11.069.

153 I. A. Raj and K. I. Vasu, Transition Metal-Based Cathodes for Hydrogen Evolution in Alkaline Solution: Electrocatalysis on Nickel-Based Ternary Electrolytic Codeposits, *J. Appl. Electrochem.*, 1992, **22**(5), 471–477, DOI: 10.1007/BF01077551.

154 S. Cherevko, S. Geiger, O. Kasian, N. Kulyk, J. P. Grote, A. Savan, B. R. Shrestha, S. Merzlikin, B. Breitbach, A. Ludwig and K. J. J. Mayrhofer, Oxygen and Hydrogen Evolution Reactions on Ru, RuO_2, Ir, and IrO_2 Thin Film Electrodes in Acidic and Alkaline Electrolytes: A Comparative Study on Activity and Stability, *Catal. Today*, 2016, **262**, 170–180, DOI: 10.1016/j.cattod.2015.08.014.

155 C. Canales, A. F. Olea, L. Gidi, R. Arce and G. Ramírez, Enhanced Light-Induced Hydrogen Evolution Reaction by Supramolecular Systems of Cobalt(II) and Copper(II) Octaethylporphyrins on Glassy Carbon Electrodes, *Electrochim. Acta*, 2017, **258**, 850–857, DOI: 10.1016/j.electacta.2017.11.135.

156 G. Zhang, K. Ming, J. Kang, Q. Huang, Z. Zhang, X. Zheng and X. Bi, High Entropy Alloy as a Highly Active and Stable Electrocatalyst for Hydrogen Evolution Reaction, *Electrochim. Acta*, 2018, **279**, 19–23, DOI: 10.1016/j.electacta.2018.05.035.

157 M. Liu, Z. Zhang, F. Okejiri, S. Yang, S. Zhou and S. Dai, Entropy-Maximized Synthesis of Multimetallic Nanoparticle Catalysts via a Ultrasonication-Assisted Wet Chemistry Method under Ambient Conditions, *Adv. Mater. Interfaces*, 2019, **6**(7), 1900015.

158 S. Gao, S. Hao, Z. Huang, Y. Yuan, S. Han, L. Lei, X. Zhang, R. Shahbazian-Yassar and J. Lu, Synthesis of High-Entropy Alloy Nanoparticles on Supports by the Fast Moving Bed Pyrolysis, *Nat. Commun.*, 2020, **11**(1), 1–12, DOI: 10.1038/s41467-020-15934-1.

159 D. Wu, K. Kusada, T. Yamamoto, T. Toriyama, S. Matsumura, I. Gueye, O. Seo, J. Kim, S. Hiroi, O. Sakata, S. Kawaguchi, Y. Kubota and H. Kitagawa, On the Electronic Structure and Hydrogen Evolution Reaction Activity of Platinum Group Metal-Based High-Entropy-Alloy Nanoparticles, *Chem. Sci.*, 2020, DOI: 10.1039/d0sc02351e.

160 H.-J. Qiu, G. Fang, J. Gao, Y. Wen, J. Lv, H. Li, G. Xie, X. Liu and S. Sun, Noble Metal-Free Nanoporous High-Entropy Alloys as Highly Efficient Electrocatalysts for Oxygen Evolution Reaction, *ACS Mater. Lett.*, 2019, **1**, 526–533, DOI: 10.1021/acsmaterialslett.9b00414.

161 D. Yang and B. C. Gates, Catalysis by Metal–Organic Frameworks: Perspective and Suggestions for Future Research, *ACS Catal.*, 2019, **9**(3), 1779–1798, DOI: 10.1021/acscatal.8b04515.

162 Q. Shi, S. Fu, C. Zhu, J. Song, D. Du and Y. Lin, Metal–Organic Frameworks-Based Catalysts for Electrochemical Oxygen Evolution, *Mater. Horizons*, 2019, **6**(4), 684–702, DOI: 10.1039/c8mh01397g.

163 S. Royer and D. Duprez, Catalytic Oxidation of Carbon Monoxide over Transition Metal Oxides, *ChemCatChem*, 2011, **3**(1), 24–65, DOI: 10.1002/cctc.201000378.

164 Y. F. Y. Yao, The Oxidation of CO and Hydrocarbons over Noble Metal Catalysts, *Journal of Catalysis*, 1984, **87**(1), 152–162, DOI: 10.1016/0021-9517(84)90178-7.

165 J. Barbier and D. Duprez, Reactivity of Steam in Exhaust Gas Catalysis I. Steam and Oxygen/Steam Conversions of Carbon Monoxide and of Propane over PtRh Catalysts, *Appl. Catal., B*, 1993, **3**(1), 61–83, DOI: 10.1016/0926-3373(93)80069-P.

166 S. L. Swartz, Catalysis by Ceria and Related Materials Edited by Alessandro Trovarelli (Università Di Udine, Italy). Catalytic Science Series. Volume 2. Series Edited by Graham J. Hutchings. Imperial College Press: London. 2002. Vviii + 508 Pp. $78.00. ISBN: 1-86094299-7-, *J. Am. Chem. Soc.*, 2002, **124**(43), 12923–12924, DOI: 10.1021/ja025256e.

167 J. Jones, H. Xiong, A. T. DeLaRiva, E. J. Peterson, H. Pham, S. R. Challa, G. Qi, S. Oh, M. H. Wiebenga, X. I. P. Hernández and Y. Wang, Thermally stable single-atom platinum-on-ceria catalysts via atom trapping, *Science*, 2016, **353**(6295), 150–154.

168 A. T. Bell, The impact of nanoscience on heterogeneous catalysis, *Science*, 2003, **299**(5613), 1688–1691.

169 P. M. Arnal, M. Comotti and F. Schüth, High-temperature-stable catalysts by hollow sphere encapsulation, *Angew. Chem., Int. Ed.*, 2006, **45**(48), 8224–8227.

170 C. Chen, C. Nan, D. Wang, Q. Su, H. Duan, X. Liu, L. Zhang, D. Chu, W. Song, Q. Peng and Y. Li, Mesoporous Multicomponent Nanocomposite Colloidal Spheres: Ideal High-Temperature Stable Model Catalysts, *Angew. Chem.*, 2011, **123**(16), 3809–3813.

171 H. Yan, H. Cheng, H. Yi, Y. Lin, T. Yao, C. Wang, J. Li, S. Wei and J. Lu, Single-atom Pd1/graphene catalyst achieved by atomic layer deposition: remarkable performance in selective hydrogenation of 1, 3-butadiene, *J. Am. Chem. Soc.*, 2015, **137**(33), 10484–10487.

172 E. J. Peterson, A. T. Delariva, S. Lin, R. S. Johnson, H. Guo, J. T. Miller, J. H. Kwak, C. H. F. Peden, B. Kiefer, L. F. Allard, F. H. Ribeiro and A. K. Datye, Low-temperature carbon monoxide oxidation catalysed by regenerable atomically dispersed palladium on alumina, *Nat. Commun.*, 2014, **5**(1), 1–11, DOI: 10.1038/ncomms5885.

173 S. Farsi, W. Olbrich, P. Pfeifer and R. Dittmeyer, A Consecutive Methanation Scheme for Conversion of CO_2 – A Study on Ni_3Fe Catalyst in a Short-Contact Time Micro Packed Bed Reactor, *Chem. Eng. J.*, 2020, **388**(January), 124233, DOI: 10.1016/j.cej.2020.124233.

174 H. Chen, J. Fu, P. Zhang, H. Peng, C. W. Abney, K. Jie, X. Liu, M. Chi and S. Dai, Entropy-Stabilized Metal Oxide Solid Solutions as CO Oxidation Catalysts with High-Temperature Stability, *J. Mater. Chem. A*, 2018, **6**(24), 11129–11133, DOI: 10.1039/c8ta01772g.

175 H. Chen, W. Lin, Z. Zhang, K. Jie, D. R. Mullins, X. Sang, S.-Z. Yang, C. J. Jafta, C. A. Bridges, X. Hu, R. R. Unocic,

J. Fu, P. Zhang and S. Dai, Mechanochemical Synthesis of High Entropy Oxide Materials under Ambient Conditions: Dispersion of Catalysts via Entropy Maximization, *ACS Mater. Lett.*, 2019, **1**(1), 83–88, DOI: 10.1021/acsmaterialslett.9b00064.

176 F. Okejiri, Z. Zhang, J. Liu, M. Liu, S. Yang and S. Dai, Room-Temperature Synthesis of High-Entropy Perovskite Oxide Nanoparticle Catalysts through Ultrasonication-Based Method, *ChemSusChem*, 2020, **13**(1), 111–115, DOI: 10.1002/cssc.201902705.

177 H. Xu, Z. Zhang, J. Liu, C. L. Do-Thanh, H. Chen, S. Xu, Q. Lin, Y. Jiao, J. Wang, Y. Wang, Y. Chen and S. Dai, Entropy-Stabilized Single-Atom Pd Catalysts via High-Entropy Fluorite Oxide Supports, *Nat. Commun.*, 2020, **11**(1), 1–9, DOI: 10.1038/s41467-020-17738-9.

178 G. W. Brunson, Foil Based Heat Exchanger and Reactor Development, *EFC 2009 – Piero Lunghi Conf. Proc. 3rd Eur. Fuel Cell Technol. Appl. Conf.*, 2009, vol. 72(3), pp. 193–194.

179 F. Schüth, R. Palkovits, R. Schlögl and D. S. Su, Ammonia as a Possible Element in an Energy Infrastructure: Catalysts for Ammonia Decomposition, *Energy Environ. Sci.*, 2012, **5**(4), 6278–6289, DOI: 10.1039/c2ee02865d.

180 J. C. Ganley, F. S. Thomas, E. G. Seebauer and R. I. Masel, A Priori Catalytic Activity Correlations: The Difficult Case of Hydrogen Production from Ammonia, *Catal. Lett.*, 2004, **96**(3–4), 117–122, DOI: 10.1023/B:CATL.0000030108.50691.d4.

181 S. F. Yin, B. Q. Xu, X. P. Zhou and C. T. Au, A Mini-Review on Ammonia Decomposition Catalysts for On-Site Generation of Hydrogen for Fuel Cell Applications, *Appl. Catal., A*, 2004, **277**(1–2), 1–9, DOI: 10.1016/j.apcata.2004.09.020.

182 S. F. Yin, Q. H. Zhang, B. Q. Xu, W. X. Zhu, C. F. Ng and C. T. Au, Investigation on the Catalysis of CO_x-Free Hydrogen Generation from Ammonia, *J. Catal.*, 2004, **224**(2), 384–396, DOI: 10.1016/j.jcat.2004.03.008.

183 C. J. H. Jacobsen, Novel Class of Ammonia Synthesis Catalysts, *Chem. Commun.*, 2000, (No. 12), 1057–1058, DOI: 10.1039/b002930k.

184 C. J. H. Jacobsen, S. Dahl, B. G. S. Clausen, S. Bahn, A. Logadottir and J. K. Nørskov, Catalyst Design by Interpolation in the Periodic Table: Bimetallic Ammonia Synthesis Catalysts, *J. Am. Chem. Soc.*, 2001, **123**(34), 8404–8405, DOI: 10.1021/ja010963d.

185 X. Duan, J. Ji, X. Yan, G. Qian, D. Chen and X. Zhou, Understanding Co–Mo Catalyzed Ammonia Decomposition: Influence of Calcination Atmosphere and Identification of Active Phase, *ChemCatChem*, 2016, **8**(5), 938–945, DOI: 10.1002/cctc.201501275.

186 A. Boisen, S. Dahl and C. J. H. Jacobsen, Promotion of Binary Nitride Catalysts: Isothermal N_2 Adsorption, Microkinetic Model, and Catalytic Ammonia Synthesis Activity, *J. Catal.*, 2002, **208**(1), 180–186, DOI: 10.1006/jcat.2002.3571.

187 A. Boisen, S. Dahl, J. K. Nørskov and C. H. Christensen, Why the Optimal Ammonia Synthesis Catalyst Is Not the Optimal Ammonia Decomposition Catalyst, *J. Catal.*, 2005, **230**(2), 309–312, DOI: 10.1016/j.jcat.2004.12.013.

188 S. Podila, S. F. Zaman, H. Driss, Y. A. Alhamed, A. A. Al-Zahrani and L. A. Petrov, Hydrogen Production by Ammonia Decomposition Using High Surface Area Mo_2N and Co_3Mo_3N Catalysts, *Catal. Sci. Technol.*, 2016, **6**(5), 1496–1506, DOI: 10.1039/c5cy00871a.

189 J. K. Pedersen, T. A. A. Batchelor, A. Bagger and J. Rossmeisl, High-Entropy Alloys as Catalysts for the CO_2 and CO Reduction Reactions, *ACS Catal.*, 2020, **10**, 2169–2176, DOI: 10.1021/acscatal.9b04343.

190 W. Xu, H. Chen, K. Jie, Z. Yang, T. Li and S. Dai, Entropy-Driven Mechanochemical Synthesis of Polymetallic Zeolitic Imidazolate Frameworks for CO_2 Fixation, *Angew. Chem., Int. Ed.*, 2019, **58**(15), 5018–5022, DOI: 10.1002/anie.201900787.

191 S. Nellaiappan, N. K. Katiyar, R. Kumar, A. Parui, K. D. Malviya, K. G. Pradeep, A. K. Singh, S. Sharma, C. S. Tiwary and K. Biswas, High-Entropy Alloys as Catalysts for the CO_2 and CO Reduction Reactions: Experimental Realization, *ACS Catal.*, 2020, **10**(6), 3658–3663, DOI: 10.1021/acscatal.9b04302.

192 R. L. Singh, P. K. Singh and R. P. Singh, Enzymatic Decolorization and Degradation of Azo Dyes – A Review, *Int. Biodeterior. Biodegrad.*, 2015, **104**, 21–31, DOI: 10.1016/j.ibiod.2015.04.027.

193 K. Vinodgopal and P. V. Kamat, Enhanced Rates of Photocatalytic Degradation of an Azo Dye Using SnO_2/TiO_2 Coupled Semiconductor Thin Films, *Environ. Sci. Technol.*, 1995, **29**(3), 841–845, DOI: 10.1021/es00003a037.

194 J. A. Laszlo, Regeneration of Azo-Dye-Saturated Cellulosic Anion Exchange Resin by Burkholderia Cepacia Anaerobic Dye Reduction, *Environ. Sci. Technol.*, 2000, **34**(1), 167–172, DOI: 10.1021/es990918u.

195 S. D. Kalme, G. K. Parshetti, S. U. Jadhav and S. P. Govindwar, Biodegradation of Benzidine Based Dye Direct Blue-6 by Pseudomonas Desmolyticum NCIM 2112, *Bioresour. Technol.*, 2007, **98**(7), 1405–1410, DOI: 10.1016/j.biortech.2006.05.023.

196 I. K. Konstantinou and T. A. Albanis, TiO2-Assisted Photocatalytic Degradation of Azo Dyes in Aqueous Solution: Kinetic and Mechanistic Investigations: A Review, *Appl. Catal., B*, 2004, **49**(1), 1–14, DOI: 10.1016/j.apcatb.2003.11.010.

197 H. Lachheb, E. Puzenat, A. Houas, M. Ksibi, E. Elaloui, C. Guillard and J. M. Herrmann, Photocatalytic Degradation of Various Types of Dyes (Alizarin S, Crocein Orange G, Methyl Red, Congo Red, Methylene Blue) in Water by UV-Irradiated Titania, *Appl. Catal., B*, 2002, **39**(1), 75–90, DOI: 10.1016/S0926-3373(02)00078-4.

198 N. K. Amin, Removal of Direct Blue-106 Dye from Aqueous Solution Using New Activated Carbons Developed from Pomegranate Peel: Adsorption Equilibrium and Kinetics, *J. Hazard. Mater.*, 2009, **165**(1–3), 52–62, DOI: 10.1016/j.jhazmat.2008.09.067.

199 V. Meshko, L. Markovska, M. Mincheva and A. E. Rodrigues, Adsorption of Basic Dyes on Granular Acivated Carbon and Natural Zeolite, *Water Res.*, 2001, **35**(14), 3357–3366, DOI: 10.1016/S0043-1354(01)00056-2.

200 H. Y. Shu, M. C. Chang, H. H. Yu and W. H. Chen, Reduction of an Azo Dye Acid Black 24 Solution Using Synthesized Nanoscale Zerovalent Iron Particles, *J. Colloid Interface Sci.*, 2007, **314**(1), 89–97, DOI: 10.1016/j.jcis.2007.04.071.

201 J. Cao, L. Wei, Q. Huang, L. Wang and S. Han, Reducing Degradation of Azo Dye by Zero-Valent Iron in Aqueous Solution, *Chemosphere*, 1999, **38**(3), 565–571, DOI: 10.1016/S0045-6535(98)00201-X.

202 L. J. Matheson and P. G. Tratnyek, Reductive Dehalogenation of Chlorinated Methanes by Iron Metal, *Environ. Sci. Technol.*, 1994, **28**(12), 2045–2053, DOI: 10.1021/es00061a012.

203 A. Agrawal and P. G. Tratnyek, Reduction of Nitro Aromatic Compounds by Zero-Valent Iron Metal, *Environ. Sci. Technol.*, 1996, **30**(1), 153–160, DOI: 10.1021/es950211h.

204 J. Q. Wang, Y. H. Liu, M. W. Chen, G. Q. Xie, D. V. Louzguine-Luzgin, A. Inoue and J. H. Perepezko, Rapid Degradation of Azo Dye by Fe-Based Metallic Glass Powder, *Adv. Funct. Mater.*, 2012, **22**(12), 2567–2570, DOI: 10.1002/adfm.201103015.

205 Y. Tang, Y. Shao, N. Chen, X. Liu, S. Q. Chen and K. F. Yao, Insight into the High Reactivity of Commercial Fe–Si–B Amorphous Zero-Valent Iron in Degrading Azo Dye Solutions, *RSC Adv.*, 2015, **5**(43), 34032–34039, DOI: 10.1039/c5ra02870a.

206 Y. F. Zhao, J. J. Si, J. G. Song, Q. Yang and X. D. Hui, Synthesis of Mg–Zn–Ca Metallic Glasses by Gas-Atomization and Their Excellent Capability in Degrading Azo Dyes, *Mater. Sci. Eng., B*, 2014, **181**(1), 46–55, DOI: 10.1016/j.mseb.2013.11.019.

207 J. Q. Wang, Y. H. Liu, M. W. Chen, V. L. L. Dmitri, A. Inoue and J. H. Perepezko, Excellent Capability in Degrading Azo Dyes by MgZn-Based Metallic Glass Powders, *Sci. Rep.*, 2012, **2**, 1–6, DOI: 10.1038/srep00418.

208 Z. Y. Lv, X. J. Liu, B. Jia, H. Wang, Y. Wu and Z. P. Lu, Development of a Novel High-Entropy Alloy with Eminent Efficiency of Degrading Azo Dye Solutions, *Sci. Rep.*, 2016, **6**(November 2015), 1–11, DOI: 10.1038/srep34213.

209 S. Wu, Y. Pan, J. Lu, N. Wang, W. Dai and T. Lu, Effect of the Addition of Mg, Ti, Ni on the Decoloration Performance of AlCrFeMn High Entropy Alloy, *J. Mater. Sci. Technol.*, 2019, **35**(8), 1629–1635, DOI: 10.1016/j.jmst.2019.03.025.

210 M. S. Lal and R. Sundara, High Entropy Oxides—A Cost-Effective Catalyst for the Growth of High Yield Carbon Nanotubes and Their Energy Applications, *ACS Appl. Mater. Interfaces*, 2019, **11**(34), 30846–30857, DOI: 10.1021/acsami.9b08794.

211 N. Osenciat, D. Bérardan, D. Dragoe, B. Léridon, S. Holé, A. K. Meena, S. Franger and N. Dragoe, Charge compensation mechanisms in Li-substituted high-entropy oxides and influence on Li superionic conductivity, *J. Am. Chem. Soc.*, 2019, **102**(10), 6156–6162.

212 D. Bérardan, S. Franger, A. K. Meena and N. Dragoe, Room temperature lithium superionic conductivity in high entropy oxides, *J. Mater. Chem. A*, 2016, **4**(24), 9536–9541.

213 X. Li, J. Wei, Q. Li, S. Zheng, Y. Xu, P. Du, C. Chen, J. Zhao, H. Xue, Q. Xu and H. Pang, Nitrogen-Doped Cobalt Oxide Nanostructures Derived from Cobalt–Alanine Complexes for High-Performance Oxygen Evolution Reactions, *Adv. Funct. Mater.*, 2018, **28**(23), 1–7, DOI: 10.1002/adfm.201800886.

214 X. Guo, S. Zheng, G. Zhang, X. Xiao, X. Li, Y. Xu, H. Xue and H. Pang, Nanostructured Graphene-Based Materials for Flexible Energy Storage, *Energy Storage Mater.*, 2017, **9**(July), 150–169, DOI: 10.1016/j.ensm.2017.07.006.

215 S. Zheng, X. Li, B. Yan, Q. Hu, Y. Xu, X. Xiao, H. Xue and H. Pang, Transition-Metal (Fe, Co, Ni) Based Metal–Organic Frameworks for Electrochemical Energy Storage, *Adv. Energy Mater.*, 2017, **7**(18), 1–27, DOI: 10.1002/aenm.201602733.

216 Y. Lu, L. Yu, X. W. Lou and David), Nanostructured Conversion-Type Anode Materials for Advanced Lithium-Ion Batteries, *Chem*, 2018, **4**(5), 972–996, DOI: 10.1016/j.chempr.2018.01.003.

217 A. Sarkar, L. Velasco, D. Wang, Q. Wang, G. Talasila, L. D. Biasi, T. Brezesinski, S. S. Bhattacharya, H. Hahn and B. Breitung, High Entropy Oxides for Reversible Energy Storage, *Nat. Commun.*, 2018, **9**(1), 1–9, DOI: 10.1038/s41467-018-05774-5.

218 Q. Wang, A. Sarkar, Z. Li, Y. Lu and L. Velasco, Electrochemistry Communications High Entropy Oxides as Anode Material for Li-Ion Battery Applications: A Practical Approach, *Electrochem. Commun.*, 2019, **100**(February), 121–125, DOI: 10.1016/j.elecom.2019.02.001.

219 N. Qiu, H. Chen, Z. Yang, S. Sun, Y. Wang and Y. Cui, Lithium Storage Performance, *J. Alloys Compd.*, 2019, **777**, 767–774, DOI: 10.1016/j.jallcom.2018.11.049.

220 M. S. Balogun, W. Qiu, Y. Luo, H. Meng, W. Mai, A. Onasanya, T. K. Olaniyi and Y. Tong, A Review of the Development of Full Cell Lithium-Ion Batteries: The Impact of Nanostructured Anode Materials, *Nano Res.*, 2016, **9**(10), 2823–2851, DOI: 10.1007/s12274-016-1171-1.

221 H. Chen, N. Qiu, B. Wu, Z. Yang, S. Sun and Y. Wang, A new spinel high-entropy oxide $(Mg_{0.2}Ti_{0.2}Zn_{0.2}Cu_{0.2}Fe_{0.2})_3O_4$ with fast reaction kinetics and excellent stability as an anode material for lithium ion batteries, *RSC Advances*, 2020, **10**(16), 9736–9744, DOI: 10.1039/D0RA00255K.

222 J. Yan, D. Wang, X. Zhang, J. Li, Q. Du, X. Liu, J. Zhang and X. Qi, Materials A High-Entropy Perovskite Titanate Lithium-Ion Battery Anode, *J. Mater. Sci.*, 2020, **55**(16), 6942–6951, DOI: 10.1007/s10853-020-04482-0.

223 Q. Wang, A. Sarkar, D. Wang, L. Velasco, R. Azmi, S. S. Bhattacharya, T. Bergfeldt, A. Düvel, P. Heitjans, T. Brezesinski and H. Hahn, Multi-anionic and-cationic compounds: new high entropy materials for advanced Li-ion batteries, *Energy Environ. Sci.*, 2019, **12**(8), 2433–2442, DOI: 10.1039/c9ee00368a.

224 C. Zhao, F. Ding, Y. Lu, L. Chen and Y. S. Hu, High-Entropy Layered Oxide Cathodes for Sodium-Ion Batteries, *Angew. Chem., Int. Ed.*, 2020, **59**(1), 264–269, DOI: 10.1002/anie.201912171.

225 D. Zheng, G. Wang, D. Liu, J. Si, T. Ding, D. Qu, X. Yang and D. Qu, The Progress of Li–S Batteries—Understanding of the Sulfur Redox Mechanism: Dissolved Polysulfide Ions in the Electrolytes, *Adv. Mater. Technol.*, 2018, **3**(9), 1700233, DOI: 10.1002/admt.201700233.

226 J. Q. Huang, Q. Zhang and F. Wei, Multi-Functional Separator/Interlayer System for High-Stable Lithium-Sulfur Batteries: Progress and Prospects, *Energy Storage Mater.*, 2015, **1**, 127–145, DOI: 10.1016/j.ensm.2015.09.008.

227 W. Li, J. Hicks-Garner, J. Wang, J. Liu, A. F. Gross, E. Sherman, J. Graetz, J. J. Vajo and P. Liu, V_2O_5 Polysulfide Anion Barrier for Long-Lived Li–S Batteries, *Chem. Mater.*, 2014, **26**(11), 3404–3410, DOI: 10.1021/cm500575q.

228 L. Kong, X. Chen, B. Q. Li, H. J. Peng, J. Q. Huang, J. Xie and Q. Zhang, A Bifunctional Perovskite Promoter for Polysulfide Regulation toward Stable Lithium–Sulfur Batteries, *Adv. Mater.*, 2018, **30**(2), 1–7, DOI: 10.1002/adma.201705219.

229 Y. Tao, Y. Wei, Y. Liu, J. Wang, W. Qiao, L. Ling and D. Long, Kinetically-Enhanced Polysulfide Redox Reactions by Nb_2O_5 Nanocrystals for High-Rate Lithium-Sulfur Battery, *Energy Environ. Sci.*, 2016, **9**(10), 3230–3239, DOI: 10.1039/c6ee01662f.

230 Y. Zhang, Y. Zhao, A. Yermukhambetova, Z. Bakenov and P. Chen, Ternary Sulfur/Polyacrylonitrile/$Mg_{0.6}Ni_{0.4}O$ Composite Cathodes for High Performance Lithium/Sulfur Batteries, *J. Mater. Chem. A*, 2013, **1**(2), 295–301, DOI: 10.1039/c2ta00105e.

231 Y. Zheng, Y. Yi, M. Fan, H. Liu, X. Li, R. Zhang, M. Li and Z. A. Qiao, A High-Entropy Metal Oxide as Chemical Anchor of Polysul Fi de for Lithium-Sulfur Batteries, *Energy Storage Mater.*, 2019, **23**, 678–683, DOI: 10.1016/j.ensm.2019.02.030.

232 V. Augustyn, P. Simon and B. Dunn, Pseudocapacitive oxide materials for high-rate electrochemical energy storage, *Energy Environ. Sci.*, 2014, **7**(5), 1597–1614.

233 T. Jin, X. Sang, R. R. Unocic, R. T. Kinch, X. Liu, J. Hu, H. Liu and S. Dai, Mechanochemical-Assisted Synthesis of High-Entropy Metal Nitride via a Soft Urea Strategy, *Adv. Mater.*, 2018, **30**(23), 1–5, DOI: 10.1002/adma.201707512.

234 L. Zhang, C. M. B. Holt, E. J. Luber, B. C. Olsen, H. Wang, M. Danaie, X. Cui, X. Tan, V. W. Lui, W. P. Kalisvaart and D. Mitlin, High Rate Electrochemical Capacitors from Three-Dimensional Arrays of Vanadium Nitride Functionalized Carbon Nanotubes, *J. Phys. Chem. C*, 2011, **115**(49), 24381–24393, DOI: 10.1021/jp205052f.

235 X. Lu, T. Liu, T. Zhai, G. Wang, M. Yu, S. Xie, Y. Ling, C. Liang, Y. Tong and Y. Li, Improving the Cycling Stability of Metal-Nitride Supercapacitor Electrodes with a Thin Carbon Shell, *Adv. Energy Mater.*, 2014, **4**(4), 1–6, DOI: 10.1002/aenm.201300994.

236 K. Kong, J. Hyun, Y. Kim, W. Kim and D. Kim, Nanoporous Structure Synthesized by Selective Phase Dissolution of AlCoCrFeNi High Entropy Alloy and Its Electrochemical Properties as Supercapacitor Electrode, *J. Power Sources*, 2019, **437**(April), 226927, DOI: 10.1016/j.jpowsour.2019.226927.

237 X. Xu, Y. Du, C. Wang, Y. Guo, J. Zou, K. Zhou, Z. Zeng, Y. Liu and L. Li, High-Entropy Alloy Nanoparticles on Aligned Electronspun Carbon Nano Fibers for Supercapacitors, *J. Alloys Compd.*, 2020, **822**, 153642, DOI: 10.1016/j.jallcom.2020.153642.

238 A. Züttel, Materials for Hydrogen Storage & Separation, *Mater. Today*, 2003, (No. May), 24–33.

239 E. Akiba and H. Iba, Hydrogen Absorption by Laves Phase Related BCC Solid Solution, *Intermetallics*, 1998, **6**(6), 461–470, DOI: 10.1016/S0966-9795(97)00088-5.

240 M. Dornheim, Thermodynamics of metal hydrides: tailoring reaction enthalpies of hydrogen storage materials, *Thermodynamics-Interaction Studies-Solids, Liquids and Gases*, 2011, pp. 891–911.

241 B. K. Rao and P. Jena, Switendick criterion for stable hydrides, *Phys. Rev. B*, 1985, **31**(10), 6726.

242 C. A. Zeng, J. P. Hu and C. Y. Ouyang, Hydrogen Solution in Tetrahedral or Octahedral Interstitial Sites in Al, *J. Alloys Compd.*, 2011, **509**(37), 9214–9217, DOI: 10.1016/j.jallcom.2011.06.115.

243 C. Ouyang and Y. S. Lee, Hydrogen-Induced Interactions in Vanadium from First-Principles Calculations, *Phys. Rev. B: Condens. Matter Mater. Phys.*, 2011, **83**(4), 1–7, DOI: 10.1103/PhysRevB.83.045111.

244 K. J. Gross, A. Züttel and L. Schlapbach, On the Possibility of Metal Hydride Formation Part II: Geometric Considerations, *J. Alloys Compd.*, 1998, **274**(1–2), 239–247, DOI: 10.1016/S0925-8388(98)00503-9.

245 G. Sandrock, Panoramic Overview of Hydrogen Storage Alloys from a Gas Reaction Point of View, *J. Alloys Compd.*, 1999, **293**, 877–888, DOI: 10.1016/S0925-8388(99)00384-9.

246 M. Latroche, Structural and Thermodynamic Properties of Metallic Hydrides Used for Energy Storage, *J. Phys. Chem. Solids*, 2004, **65**(2–3), 517–522, DOI: 10.1016/j.jpcs.2003.08.037.

247 B. Sakintuna, F. Lamari-Darkrim and M. Hirscher, Metal Hydride Materials for Solid Hydrogen Storage: A Review, *Int. J. Hydrogen Energy*, 2007, **32**(9), 1121–1140, DOI: 10.1016/j.ijhydene.2006.11.022.

248 Y. Tominaga, S. Nishimura, T. Amemiya, T. Fuda, T. Tamura, T. Kuriiwa, A. Kamegawa and M. Okada, Protium absorption-desorption properties of Ti–V–Cr alloys with a BCC structure, *Materials Transactions, JIM*, 1999, **40**(9), 871–874.

249 H. Iba and E. Akiba, Hydrogen Absorption and Modulated Structure in Ti–V–Mn Alloys, *J. Alloys Compd.*, 1997, **253–254**, 21–24, DOI: 10.1016/S0925-8388(96)03072-1.

250 Y. Tominaga, K. Matsumoto, T. Fuda, T. Tamura, T. Kuriiwa, A. Kamegawa, H. Takamura and M. Okada, Protium absorption-desorption properties of Ti–V–Cr–(Mn, Ni) alloys, *Materials Transactions, JIM*, 2000, **41**(5), 617–620.

251 S. W. Cho, H. Enoki and E. Akiba, Effect of Fe Addition on Hydrogen Storage Characteristics of $Ti_{0.16}Zr_{0.05}Cr_{0.22}V_{0.57}$

Alloy, *J. Alloys Compd.*, 2000, **307**(1–2), 304–310, DOI: 10.1016/S0925-8388(00)00839-2.

252 T. Kohno, H. Yoshida, F. Kawashima, T. Inaba, I. Sakai, M. Yamamoto and M. Kanda, Hydrogen Storage Properties of New Ternary System Alloys: La_2MgNi_9, $La_5Mg_2Ni_{23}$, La_3MgNi_{14}, *J. Alloys Compd.*, 2000, **311**(2), 5–7, DOI: 10.1016/S0925-8388(00)01119-1.

253 K. hsiung Young and J. Nei, The Current Status of Hydrogen Storage Alloy Development for Electrochemical Applications, *Materials*, 2013, **6**(10), 4574–4608, DOI: 10.3390/ma6104574.

254 M. V. Lototskyy, V. A. Yartys, B. G. Pollet and R. C. Bowman, Metal Hydride Hydrogen Compressors: A Review, *Int. J. Hydrogen Energy*, 2014, **39**(11), 5818–5851, DOI: 10.1016/j.ijhydene.2014.01.158.

255 J. J. Reilly and R. H. Wiswall, The Higher Hydrides of Vanadium and Niobium, *Inorg. Chem.*, 1970, **9**(7), 1678–1682, DOI: 10.1021/ic50089a013.

256 M. Tsukahara, K. Takahashi, T. Mishima, A. Isomura and T. Sakai, Vanadium-Based Solid Solution Alloys with Three-Dimensional Network Structure for High Capacity Metal Hydride Electrodes, *J. Alloys Compd.*, 1997, **253–254**, 583–586, DOI: 10.1016/S0925-8388(96)02912-X.

257 T. Fuda, K. Matsumoto, Y. Tominaga, T. Tamura, T. Kuriiwa, A. Kamegawa and M. Okada, Effects of additions of BCC former elements on protium absorbing properties of Cr–Ti–V alloys, *Materials Transactions, JIM*, 2000, **41**(5), 577–580.

258 C. Y. Seo, J. H. Kim, P. S. Lee and J. Y. Lee, Hydrogen Storage Properties of Vanadium-Based b.c.c. Solid Solution Metal Hydrides, *J. Alloys Compd.*, 2003, **348**(1–2), 252–257, DOI: 10.1016/S0925-8388(02)00831-9.

259 S. W. Cho, C. S. Han, C. N. Park and E. Akiba, Hydrogen Storage Characteristics of Ti–Cr–V Alloys, *J. Alloys Compd.*, 1999, **288**(1–2), 294–298, DOI: 10.1016/S0925-8388(99)00096-1.

260 T. Kuriiwa, T. Tamura, T. Amemiya, T. Fuda, A. Kamegawa, H. Takamura and M. Okada, New V-Based Alloys with High Protium Absorption and Desorption Capacity, *J. Alloys Compd.*, 1999, **293**, 433–436, DOI: 10.1016/S0925-8388(99)00325-4.

261 K. Young, J. Nei, D. F. Wong and L. Wang, Structural, Hydrogen Storage, and Electrochemical Properties of Laves Phase-Related Body-Centered-Cubic Solid Solution Metal Hydride Alloys, *Int. J. Hydrogen Energy*, 2014, **39**(36), 21489–21499, DOI: 10.1016/j.ijhydene.2014.01.134.

262 Y. Kao, S. Chen, J. Sheu, J. Lin, W. Lin, J. Yeh, S. Lin, T. Liou and C. Wang, Hydrogen Storage Properties of Multi-Principal-Component $CoFeMnTi_xV_yZr_z$ Alloys, *Int. J. Hydrogen Energy*, 2010, **35**(17), 9046–9059, DOI: 10.1016/j.ijhydene.2010.06.012.

263 I. Kunce, M. Polanski and J. Bystrzycki, Microstructure and Hydrogen Storage Properties of a TiZrNbMoV High Entropy Alloy Synthesized Using Laser Engineered Net Shaping (LENS), *Int. J. Hydrogen Energy*, 2014, **39**(18), 9904–9910, DOI: 10.1016/j.ijhydene.2014.02.067.

264 I. Kunce, M. Polański and T. Czujko, Microstructures and hydrogen storage properties of LaNiFeVMn alloys, *Int. J. Hydrogen Energy*, 2017, **42**(44), 27154–27164.

265 I. Kunce, M. Polanski and J. Bystrzycki, Structure and Hydrogen Storage Properties of a High Entropy ZrTiVCrFeNi Alloy Synthesized Using Laser Engineered Net Shaping (LENS) Structure and Hydrogen Storage Properties of a High Entropy ZrTiVCrFeNi Alloy Synthesized Using Laser Engineered Net Shaping, *Int. J. Hydrogen Energy*, 2013, **38**(January), 12180–12189, DOI: 10.1016/j.ijhydene.2013.05.071.

266 S. K. Chen, P. H. Lee, H. Lee and H. T. Su, Hydrogen storage of C14-CruFevMnwTixVyZrz alloys, *Mater. Chem. Phys.*, 2018, **210**, 336–347.

267 M. Sahlberg, D. Karlsson, C. Zlotea and U. Jansson, Superior hydrogen storage in high entropy alloys, *Sci. Rep.*, 2016, **6**, 36770.

268 D. Karlsson, G. Ek, J. Cedervall, C. Zlotea, K. T. Møller, T. C. Hansen, J. Bednarčík, M. Paskevicius, M. H. Sørby, T. R. Jensen, U. Jansson and M. Sahlberg, Structure and Hydrogenation Properties of a HfNbTiVZr High-Entropy Alloy, *Inorg. Chem.*, 2018, **57**(4), 2103–2110, DOI: 10.1021/acs.inorgchem.7b03004.

269 C. Zlotea, M. A. Sow, G. Ek, J. P. Couzinié, L. Perrière, I. Guillot, J. Bourgon, K. T. Møller, T. R. Jensen, E. Akiba and M. Sahlberg, Hydrogen sorption in TiZrNbHfTa high entropy alloy, *J. Alloys Compd.*, 2019, **775**, 667–674.

270 M. M. Nygård, G. Ek, D. Karlsson, M. Sahlberg, M. H. Sørby and B. C. Hauback, Hydrogen storage in high-entropy alloys with varying degree of local lattice strain, *Int. J. Hydrogen Energy*, 2019, **44**(55), 29140–29149.

271 M. M. Nygård, G. Ek, D. Karlsson, M. H. Sørby, M. Sahlberg and B. C. Hauback, Counting Electrons – A New Approach to Tailor the Hydrogen Sorption Properties of High-Entropy Alloys, *Acta Materialia*, 2019, **175**, 121–129, DOI: 10.1016/j.actamat.2019.06.002.

272 H. Shen, J. Zhang, J. Hu, J. Zhang, Y. Mao, H. Xiao, X. Zhou and X. Zu, A novel TiZrHfMoNb high-entropy alloy for solar thermal energy storage, *Nanomaterials*, 2019, **9**(2), 248.

273 J. Hu, H. Shen, M. Jiang, H. Gong, H. Xiao, Z. Liu, G. Sun and X. Zu, A DFT study of hydrogen storage in high-entropy alloy TiZrHfScMo, *Nanomaterials*, 2019, **9**(3), 461.

274 G. Zepon, D. R. Leiva, R. B. Strozi, A. Bedoch, S. J. A. Figueroa, T. T. Ishikawa and W. J. Botta, Hydrogen-Induced Phase Transition of $MgZrTiFe_{0.5}Co_{0.5}Ni_{0.5}$ High Entropy Alloy, *Int. J. Hydrogen Energy*, 2018, **43**(3), 1702–1708, DOI: 10.1016/j.ijhydene.2017.11.106.

275 H. Luo, Z. Li and D. Raabe, Hydrogen Enhances Strength and Ductility of an Equiatomic High-Entropy Alloy, *Sci. Rep.*, 2017, **7**(1), 1–7, DOI: 10.1038/s41598-017-10774-4.

276 C. Oses, C. Toher and S. Curtarolo, High-Entropy Ceramics, *Nat. Rev. Mater.*, 2020, **5**(4), 295–309, DOI: 10.1038/s41578-019-0170-8.

277 S. D. Lacey, Q. Dong, Z. Huang, J. Luo, H. Xie, Z. Lin, D. J. Kirsch, V. Vattipalli, C. Povinelli, W. Fan, R. Shahbazian-Yassar, D. Wang and L. Hu, Stable

Multimetallic Nanoparticles for Oxygen Electrocatalysis, *Nano Lett.*, 2019, **19**(8), 5149–5158, DOI: 10.1021/acs.nanolett.9b01523.

278 J. Lau, R. H. DeBlock, D. M. Butts, D. S. Ashby, C. S. Choi and B. S. Dunn, Sulfide solid electrolytes for lithium battery applications, *Adv. Energy Mater.*, 2018, **8**(27), 1800933.

279 K. Murata, S. Izuchi and Y. Yoshihisa, Overview of the Research and Development of Solid Polymer Electrolyte Batteries, *Electrochim. Acta*, 2000, **45**(8), 1501–1508, DOI: 10.1016/S0013-4686(99)00365-5.

280 A. Manuel Stephan and K. S. Nahm, Review on Composite Polymer Electrolytes for Lithium Batteries, *Polymer*, 2006, 5952–5964, DOI: 10.1016/j.polymer.2006.05.069.

281 P. Yao, H. Yu, Z. Ding, Y. Liu, J. Lu, M. Lavorgna, J. Wu and X. Liu, Review on Polymer-Based Composite Electrolytes for Lithium Batteries, *Front. Chem.*, August 8, 2019, 522, DOI: 10.3389/fchem.2019.00522.

282 R. Rojaee, S. Cavallo, S. Mogurampelly, B. K. Wheatle, V. Yurkiv, R. Deivanayagam, T. Foroozan, M. G. Rasul, S. Sharifi-Asl, A. H. Phakatkar, M. Cheng, S. Son, Y. Pan, F. Mashayek, V. Ganesan and R. Shahbazian-Yassar, Highly-Cyclable Room-Temperature Phosphorene Polymer Electrolyte Composites for Li Metal Batteries, *Adv. Funct. Mater.*, 2020, **30**(32), 1910749, DOI: 10.1002/adfm.201910749.

283 M. Cheng, A. Ramasubramanian, M. G. Rasul, Y. Jiang, Y. Yuan, T. Foroozan, R. Deivanayagam, M. Tamadoni Saray, R. Rojaee, B. Song, V. R. Yurkiv, Y. Pan, F. Mashayek and R. Shahbazian-Yassar, Direct Ink Writing of Polymer Composite Electrolytes with Enhanced Thermal Conductivities, *Adv. Funct. Mater.*, 2020, 2006683, DOI: 10.1002/adfm.202006683.

284 R. Deivanayagam, M. Cheng, M. Wang, V. Vasudevan, T. Foroozan, N. V. Medhekar and R. Shahbazian-Yassar, Composite Polymer Electrolyte for Highly Cyclable Room-Temperature Solid-State Magnesium Batteries, *ACS Appl. Energy Mater.*, 2019, **2**(11), 7980–7990, DOI: 10.1021/acsaem.9b01455.

285 S. Pothukuchi, Y. Li and C. P. Wong, Development of a Novel Polymer-Metal Nanocomposite Obtained through the Route of In Situ Reduction for Integral Capacitor Application, *J. Appl. Polym. Sci.*, 2004, **93**(4), 1531–1538, DOI: 10.1002/app.20626.

286 Y. Zare and I. Shabani, Polymer/Metal Nanocomposites for Biomedical Applications, *Mater. Sci. Eng., C*, 2016, **60**(28), 195–203, DOI: 10.1016/j.msec.2015.11.023.

287 M. R. Cerón, L. S. Lai, A. Amiri, M. Monte, S. Katta, J. C. Kelly, M. A. Worsley, M. D. Merrill, S. Kim and P. G. Campbell, Surpassing the Conventional Limitations of CO_2 separation Membranes with Hydroxide/Ceramic Dual-Phase Membranes, *J. Memb. Sci.*, 2018, **567**, DOI: 10.1016/j.memsci.2018.09.028.

288 B. Duhoux, P. Mehrani, D. Y. Lu, R. T. Symonds, E. J. Anthony and A. Macchi, Combined calcium looping and chemical looping combustion for post-combustion carbon dioxide capture: process simulation and sensitivity analysis, *Energy Technol.*, 2016, **4**(10), 1158–1170.

289 J. Adánez, L. F. de Diego, F. García-Labiano, P. Gayán, A. Abad and J. M. Palacios, Selection of oxygen carriers for chemical-looping combustion, *Energy Fuels*, 2004, **18**(2), 371–377.

290 A. Amiri, MSc thesis, Extraction of Oxygen from CO2 in *Chemical Looping Using Doped Ceria*, Southern, Illinois University, 2017.

291 A. Amiri, A. Sims and K. Mondal CO_2 Driven Chemical Looping Gasification on Doubly Doped Ceria, in *2017 AIChE Annual Meeting*, Minneapolis MN, 2017, ISBN: 978-0-8169-1102-8.

292 S. Sun, M. Zhao, L. Cai, S. Zhang, D. Zeng and R. Xiao, Performance of CeO_2-Modified Iron-Based Oxygen Carrier in the Chemical Looping Hydrogen Generation Process, *Energy Fuels*, 2015, **29**(11), 7612–7621, DOI: 10.1021/acs.energyfuels.5b01444.

293 F. He, Y. Wei, H. Li and H. Wang, Synthesis Gas Generation by Chemical-Looping Reforming Using Ce-Based Oxygen Carriers Modified with Fe, Cu, and Mn Oxides, *Energy Fuels*, 2009, **23**(4), 2095–2102, DOI: 10.1021/ef800922m.